

QUANTIFYING WIND RESOURCE ASSESSMENT AND
GRID INTEGRATION CHALLENGES FOR
DELAWARE OFFSHORE WIND POWER UTILIZING
MESOSCALE MODELING TECHNIQUES

by

Joseph F. Brodie

A dissertation submitted to the Faculty of the University of Delaware in partial fulfillment of the requirements for the degree of Doctor of Philosophy in Marine Studies

Summer 2016

© 2016 Joseph F. Brodie
All Rights Reserved

ProQuest Number: 10192307

All rights reserved

INFORMATION TO ALL USERS

The quality of this reproduction is dependent upon the quality of the copy submitted.

In the unlikely event that the author did not send a complete manuscript and there are missing pages, these will be noted. Also, if material had to be removed, a note will indicate the deletion.



ProQuest 10192307

Published by ProQuest LLC (2016). Copyright of the Dissertation is held by the Author.

All rights reserved.

This work is protected against unauthorized copying under Title 17, United States Code
Microform Edition © ProQuest LLC.

ProQuest LLC.
789 East Eisenhower Parkway
P.O. Box 1346
Ann Arbor, MI 48106 - 1346

QUANTIFYING WIND RESOURCE ASSESSMENT AND
GRID INTEGRATION CHALLENGES FOR
DELAWARE OFFSHORE WIND POWER UTILIZING
MESOSCALE MODELING TECHNIQUES

by

Joseph F. Brodie

Approved: _____

Mark A. Moline, Ph.D.

Director of the School of Marine Science and Policy

Approved: _____

Mohsen Badiy, Ph.D.

Interim Dean of the College of Earth, Ocean, and Environment

Approved: _____

Ann L. Ardis, Ph.D.

Senior Vice Provost for Graduate and Professional Education

I certify that I have read this dissertation and that in my opinion it meets the academic and professional standard required by the University as a dissertation for the degree of Doctor of Philosophy.

Signed: _____

Dana E. Veron, Ph.D.
Professor in charge of dissertation

I certify that I have read this dissertation and that in my opinion it meets the academic and professional standard required by the University as a dissertation for the degree of Doctor of Philosophy.

Signed: _____

Cristina L. Archer, Ph.D.
Member of dissertation committee

I certify that I have read this dissertation and that in my opinion it meets the academic and professional standard required by the University as a dissertation for the degree of Doctor of Philosophy.

Signed: _____

Julie K. Lundquist, Ph.D.
Member of dissertation committee

I certify that I have read this dissertation and that in my opinion it meets the academic and professional standard required by the University as a dissertation for the degree of Doctor of Philosophy.

Signed: _____

Fabrice Veron, Ph.D.
Member of dissertation committee

ACKNOWLEDGEMENTS

I would like to thank the coauthors on the papers developed out of the dissertation work described and other projects throughout graduate school, including Justin Gilchrist, Yosef Shirazi, Lance Noel, Cory Budischak, and Willett Kempton;

Brian Vanderwende for his script used in generating WRF's vertical levels;

Sara Rauscher for granting access to her computing resources on the `farber` cluster;

Mary Martin for her encouragement and advocacy throughout my service to UD;

My family for all of their support over the years, and always encouraging my passion for science and mathematics; most especially my grandfather, Frank Ratcliffe, whose passion for gardening and weather drove my early childhood interest in meteorology and the environment;

My partner, Yiben Wang, for always encouraging me to write and push me to work harder throughout the dissertation process, even (and especially) when I was resistant;

My committee members, Cristina Archer, Julie Lundquist, and Fabrice Veron, for their ongoing flexibility and willingness to sit down and discuss my work whenever I needed to;

My advisor, Dana Veron, for her guidance and friendship over the past 12+ years, serving as an ideal mentor for an aspiring young scientist, despite the detours and difficulties along the way.

This research was supported in part through the use of computational and staff resources provided by Information Technologies at the University of Delaware.

TABLE OF CONTENTS

LIST OF TABLES	viii
LIST OF FIGURES	x
ABSTRACT	xiii
 Chapter	
1 INTRODUCTION	1
2 BACKGROUND AND MOTIVATION	4
2.1 Boundary Layer Meteorology	4
2.2 Offshore Wind in the Northeast United States	10
2.2.1 Resource Assessments	10
2.3 Synoptic Typing	12
2.4 Ramp Events	15
2.5 Wind Farms	17
2.5.1 Wake Modeling	17
2.5.2 Interfacing with the Grid	21
2.5.3 Wind Turbine Designs	24
2.6 WRF Model Description	26
2.7 Meteorological Data Descriptions	29
2.7.1 Observational Data	29
2.7.2 Modeling and Reanalysis Data	31
3 IDEALIZED MODELING USING CLIMATOLOGY	33
3.1 Model Setup	33

3.2	Basic Wind Farm Shape Analysis	34
3.2.1	Wind Farm Design	35
3.2.2	Idealized Model Results	37
3.3	Wind Rose Analysis	42
3.3.1	Basic Geometric Arrays	43
3.3.2	Customized Array	44
3.4	Summary and Conclusions	50
4	EVALUATING MODEL PERFORMANCE FOR RAMP EVENTS	51
4.1	Wind Ramp Identification using Observational Data	51
4.1.1	Selection of Case Studies	54
4.2	Modeling Ramp Events with WRF Forecasts	56
4.3	Meteorological Evaluation of Model Performance	59
4.3.1	Forecasting Error Metrics	62
4.3.2	Grid Impacts and Assessing Forecast Probabilities	69
4.4	Summary and Conclusions	73
5	REGIONAL MODELING OF A DELAWARE OFFSHORE WIND FARM	74
5.1	Case Study Selection	74
5.2	Model Setup	79
5.2.1	The Wind Farms and Model Domain	80
5.2.2	Forcing Data and Model Physics	84
5.3	Model Results	89
5.3.1	Wind Energy Production of the Primary Farms	89
5.3.2	Wind Energy Production of the Supplemental Farms	96
5.3.3	Meteorological Factors	99
5.3.4	Front Row Equivalent Turbine Count	103

5.3.5	Annual Results	108
5.4	Summary and Conclusions	113
6	DISCUSSION AND CONCLUSIONS	116
6.1	Resource Assessment Improvements	116
6.2	Forecasting Improvements	118
6.3	Future Work	119
6.4	Final Remarks	120
	REFERENCES	121
 Appendix		
A	WIND TURBINE LOCATION FILES	130
A.1	Rectangle (RECT)	130
A.2	Custom Shape (CUST)	132
A.2.1	Filled Custom Shape (FILL)	134
A.3	Rotated (ROTD)	135
A.4	Rotated - Adjusted (RADJ)	137
A.5	Staggered - North/South Winds (STNS)	139
A.6	Staggered - West/East Winds (STWE)	141

LIST OF TABLES

2.1	Table showing a selection of approximate surface roughness lengths for various terrain types.	6
3.1	Calculations of power output from the 5 simulated wind farms, using WRF predicted winds at 100 m hub height.	40
3.2	Calculations of power output produced by two Bluewater Wind-type wind farms at the three predominant wind directions.	48
3.3	Total power produced in the model runs for a Bluewater Wind-type wind farm under the climatological wind conditions at Buoy 44009.	49
4.1	Case study dates of ramps selected for modeling along with their synoptic type.	55
4.2	Parameterizations selected for the model runs conducted using WRF for the ramp prediction study.	61
5.1	Frequency of winter synoptic types, both from the entire period that Siegert et al. (2016) used to develop the synoptic types, and for the selected period for this research, 2005–2011.	76
5.2	Frequency of summer synoptic types, both from the entire period that Siegert et al. (2016) used to develop the synoptic types, and for the selected period for this research, 2005–2011.	76
5.3	Number of case studies selected by synoptic type.	77
5.4	Selected case study dates for modeling of the Delaware Wind Energy Area.	78
5.5	Alternate case study dates for the regional modeling of the Delaware Wind Energy Area.	79
5.6	The vertical structure of the WRF domains.	87

5.7	Parameterizations selected for the model runs conducted using WRF for the regional study.	90
5.8	Comparison of different custom-shaped farms.	100
5.9	Performance of the modeled farms for the 2007-08-25 case study. . .	101
5.10	Performance of the modeled farms for the 2008-02-14 case study. . .	103
5.11	Summary of the calculated energy production for the entire winter season based on the synoptic type distribution.	111
5.12	Summary of the calculated energy production for the entire summer season based on the synoptic type distribution.	112

LIST OF FIGURES

2.1	Wind speed profiles calculated using 3 different values for surface roughness length.	7
2.2	Histogram of capacity factor (CF) for all 11 wind farms combined in the Kempton et al. (2010) study.	11
2.3	Map depicting the Delaware Wind Energy Area as specified in Bluewater Wind Delaware’s lease from the Bureau of Ocean Energy Management.	12
2.4	Figure depicting power losses experienced along rows of wind turbines within the Nysted and Horns Rev wind farms in Denmark.	18
2.5	Map depicting the geographical area operated under PJM Interconnection and the various utility companies that constitute the PJM region.	23
2.6	Illustration of the electricity demand (load) in PJM Interconnection from 2005-2011.	25
3.1	The five example wind farm layouts used in the idealized WRF simulations.	36
3.2	WRF model output for the 5 example farms, depicting wind speed at 100 m height after 90 minutes of model integration.	38
3.3	WRF model output for the 5 sample farms, depicting wind speed along a vertical slice through the center of each wind farm in the along-wind direction after 90 minutes of model integration.	39
3.4	The published power curve for the REpower 5M wind turbine.	40
3.5	Normalized power output for a single row of the long rectangular array.	41

3.6	Wind rose for Buoy 44009, a NOAA buoy located off of the coast of Delaware.	43
3.7	WRF model output of EQT with wind from 6 wind directions. . . .	45
3.8	WRF model output of two possible Bluewater Wind-type projects.	46
3.9	Histograms depicting the number of wind turbines producing a given amount of power for each of the two Bluewater Wind-type farms. . .	47
4.1	The published power curve for the Vestas V164 wind turbine. . . .	53
4.2	Distributions of the 357 ramp-up events detected by the ramp algorithm.	53
4.3	Monthly mean and standard deviation of ramps that occurred in January from 2006-2011.	55
4.4	Synoptic type by number from Siegert et al. (2016) for 2005-2011. .	57
4.5	WRF model domains for the ramp case studies.	60
4.6	WRF modeled wind speeds using all three forcing datasets at Buoy 44009 extrapolated to 120 m hub height, compared to observations for the analog cases.	63
4.7	WRF modeled wind speeds using all three forcing datasets at Buoy 44009 extrapolated to 120 m hub height, compared to observations for the extreme cases.	65
4.8	Two of the selected case studies showing the ramps as observed and modeled by WRF.	67
4.9	Illustration of the electricity demand (load) in PJM Interconnection from 2005-2011.	71
5.1	The layouts of the 6 modeled wind farms.	82
5.2	Map showing the area of the five modeled wind farms in this study, superposed on the Delaware Wind Energy Area lease area.	83
5.3	The WRF modeling domains for the regional modeling study. . . .	85

5.4	The vertical structure of the WRF model for all domains.	86
5.5	The daily capacity factor predicted by WRF for all case studies, for RECT and CUST farm layout.	93
5.6	Probability distribution of capacity factors for each individual turbine at all model timesteps for all of the case studies.	94
5.7	Comparison between total farm capacity factor for RECT and CUST at every time interval for all case studies run.	95
5.8	Comparison between total farm capacity factor for RECT, CUST, and the 3 supplemental farm shapes at every time step for the selected cased studies explored using all of the supplemental shapes.	97
5.9	Comparison between total farm capacity factor for CUST and FILL-NC at every time step for the selected cased studies explored using all of the supplemental shapes.	98
5.10	Winds as modeled in the innermost domain for the 2007-08-25 case study date at 18Z.	102
5.11	Winds as modeled in the innermost domain for the 2008-02-14 case study date at 18Z.	104
5.12	The wind turbine productivity for several of the farms at 1800Z on 2008-02-14.	105
5.13	The wind farm productivity for the primary farms at 1800Z on 2007-08-25.	107
5.14	Wind farm productivity for the supplemental farms at 1800Z on 2007-08-25.	109
5.15	Probability distribution of capacity factors for each individual turbine at all model timesteps for all of the case studies modeled.	113
5.16	Comparison between total farm capacity factor for RECT and CUST at every time interval for all case studies run.	114

ABSTRACT

Offshore wind in the United States continues to be a focused area of research as our society grapples with the Earth's changing climate and our ongoing and increasing demand for electricity. While the first offshore wind project in the U.S. is expected to be operational soon, much still remains to be done to help improve viability of offshore wind in additional locations. This dissertation discusses three studies conducted to improve the understanding of and expectations from developing wind energy in the Delaware Wind Energy Area off the Delaware coast. The first study examines the capabilities of the Weather Research and Forecasting (WRF) model to account for variations in wind farm array geometries in an idealized set-up of the model, and determines features of those array geometries that can positively influence the energy production of an offshore farm. The second study investigates the impacts that the misprediction of wind ramp events would have on the interaction of an offshore wind farm with the electricity grid, quantifying some of these impacts and discussing factors which contribute to grid instability. The third study combines the knowledge gained in the first two studies to evaluate potential wind farm array geometries in a regional study of the Delaware Wind Energy Area using WRF along with a selection of case study dates selected to examine the impacts of the synoptic variability of the region throughout the year.

These studies demonstrate that careful consideration of the meteorology and climatology of a region when determining the layout of an offshore wind array can improve the power production of the farm, thereby improving wind farm viability. It is shown that using a mesoscale model that incorporates a wind farm parameterization can improve resource assessment by allowing the assessment to evaluate the wind farm's interactions with the weather and climate in the Delaware Wind Energy Area.

Furthermore, it is shown that while certain synoptic conditions can improve the power production of a wind facility, synoptic conditions can also lead to increased unpredictability of the wind which can result in grid stability concerns. Improvements in wind forecasting during the early morning and evening hours would help to reduce these concerns. It is only through the thorough understanding of the various scales of atmospheric dynamics at work that offshore wind farms can prove to be a successful solution for our future energy needs while reducing the impacts of climate change and our usage of fossil fuels.

Chapter 1

INTRODUCTION

Society continues to grapple with approaches to mitigating the anthropogenic forcing of climate change, without sacrificing modern conveniences and technological advancements. As the world continues to modernize, the need for energy will climb. At the same time, fossil fuel use cannot continue indefinitely, whether due to a finite supply, or ongoing concerns over the increasing level of greenhouse gas emissions. The result is that low or no emission, carbon-neutral forms of energy production will continue to expand and, hopefully, become the norm.

Meaningful progress in this energy production transition faces many challenges. Electricity usage remains high in a modern, technologically savvy society, while electricity use in developing nations is climbing rapidly. The [U.S. Energy Information Administration \(2016b\)](#) estimates that global energy use will increase from 2.16×10^{13} kWh in 2012 to 3.65×10^{13} kWh by 2040, an increase of 69% over 28 years. Reducing society's reliance on fossil fuels may also lead to an increase in electricity use: gasoline and diesel motor vehicles may transition to electric vehicles; high-speed electric trains could offset fossil fuel-burning aircraft; natural gas and fuel oil heating systems common in many colder climates can be replaced with more efficient electric heating ([Kempton et al., 2007](#); [Noel et al., 2016](#)). While energy conservation measures also continue to expand, the overall demand for electricity will continue to rise. Renewable energy sources can, and should, play a significant part in fulfilling this demand.

Wind energy is one promising source of renewable energy for society's expanding electricity needs. Land-based wind turbines have been used for decades, and over the years have become larger and more efficient. In many regions, they have proven to be a significant part of a reliable electricity system ([Madariaga et al., 2012](#); [Firestone et al.,](#)

2015). Offshore wind, in contrast, is still an energy source in its relative infancy in the United States. Wind farms have been constructed offshore in Europe for a number of years, and much has been learned in these early projects. Despite tremendous potential for offshore wind in the United States (i.e. [Kempton et al., 2007](#)), there is yet to be an operational offshore wind farm; the first one, the Block Island Wind Farm, is a 5 turbine installation off Rhode Island by Deepwater Wind, expected to be operational in late 2016 ([Deepwater Wind, 2016](#)). Through ongoing input from scientists, engineers, and policymakers, Deepwater Wind and other American developers stand to learn from any challenges and missteps from the earlier European projects ([Firestone et al., 2015](#)).

Developing offshore wind presents unique challenges, quite different from its land-based counterpart ([Manwell et al., 2007](#)). Offshore turbines are often considerably larger, and require expensive foundations below the waterline, or floating platforms (currently in development). Construction must make careful geological considerations, as the seabed is frequently not as easy to observe as the land. There are often public perception issues surrounding the development of offshore wind projects (i.e. [Firestone and Kempton, 2007](#)). The sea surface is dynamic, and the structure must be able to withstand ocean wave action, in addition to the air flow stresses. Expensive submarine cables must be deployed in order to deliver the electricity to land. Offshore wind farms are also subject to a unique atmosphere; the boundary layer dynamics over the ocean are significantly different from that seen on land, and in many ways, are not as well understood. Exacerbating this is the fact that atmospheric observations over the ocean are sparse compared to land, increasing the reliance on quality modeling in order to assess wind resource potential. As the use of wind energy continues to expand, both onshore and offshore, the electrical grid faces challenges in maintaining system reliability with a variable and less predictable power source ([Cochran et al., 2014](#)).

The unique questions raised by the need to better understand and predict the atmospheric dynamics in an offshore wind farm are the focus of this dissertation. Research questions include:

- How does the layout of an offshore wind farm influence the power produced by

that farm?

- What wind farm layout design considerations are most significant to improving the productivity of the farm?
- How can the knowledge gained about wind farm layout be used to improve resource assessments for offshore wind, improving the prospects for successful offshore projects?
- How do the highly variable wind conditions such as wind ramp events impact an operational wind farm's grid interactions?
- What meteorological and power demand conditions could lead to increased uncertainty in the wind power forecast?

These questions are the broad themes behind the three studies performed in this dissertation, with the ultimate goal of furthering the understanding of how a wind farm constructed off of Delaware might perform.

Chapter 2

BACKGROUND AND MOTIVATION

Ongoing advances in researching offshore wind allow for increased penetration of renewable energy that is necessary as society reduces its reliance on fossil fuels and attempts to mitigate impacts from global climate change. Specifically, [Archer et al. \(2014\)](#) addressed three primary areas of necessary research over the next 10 years for ongoing offshore wind development: improving resource assessments; reducing wind power forecasting uncertainty; and better understanding turbulent wake losses. This dissertation aims to explore all three of these areas in various ways.

This chapter describes relevant research for the following in-depth study of how wind farm layout and forecasting uncertainty could influence the productivity of offshore wind in the Delaware region. There is an overview of some important principles of boundary layer meteorology, methods for classifying meteorological conditions, and exploration of how variations in the wind can be problematic for wind energy operations. Following that is a review of salient research into offshore wind turbine development and, in particular, the research focused on modeling wind turbine wake effects. Finally, the Weather Research and Forecasting (WRF) model will be described in detail, along with a description of the types of data used throughout this study.

2.1 Boundary Layer Meteorology

Numerous observational and theoretical studies have shown that wind speed generally increases with height away from the surface, due to the reduced impact of friction as distance from the surface increases. In fluid dynamics, the portion of the atmosphere influenced by friction is known as the *boundary layer*. From a wind energy perspective, the vertical variations in wind speed characteristics in the atmospheric

boundary layer mean that there is a benefit to increasing the height of wind turbines above the surface: the higher up the nacelle, the faster the wind. The faster the wind, the more power which can be extracted. However, there comes an altitude above which there is relatively little increase in wind speed with height, known as the *free atmosphere*. The transition from boundary layer to free atmosphere happens anywhere between 100 m and 3000 m above the surface, with an overall average of around 1000 m. The wind aloft is known as the *geostrophic wind* and is essentially a balance between the pressure gradient force and the Coriolis force (Stull, 1988).

One of the most commonly used models for estimating wind speed changes with height within the boundary layer is the *log law relationship* (Manwell et al., 2010), shown below as Equation 2.1, where $U(z)$ is the estimated wind speed at height z , $U(z_r)$ is an observed wind speed at a reference height z_r , and z_0 is a parameter defined as the *roughness length*:

$$U(z) = U(z_r) \cdot \left[\ln \left(\frac{z}{z_0} \right) / \ln \left(\frac{z_r}{z_0} \right) \right] \quad (2.1)$$

The roughness length is a way to parameterize the overall impact of the surface friction on the boundary layer. A selection of sample roughness lengths is shown in Table 2.1. The roughness length can be calculated for a variety of scenarios using laboratory data or real-world observations of the vertical wind profile. As can be seen in the table, there is a very large difference between the surface roughness of an offshore region and any onshore region; the roughness lengths for rough seas are an order of magnitude less than those for basic short grass, and four orders of magnitude smaller than that seen in developed areas.

The boundary layer winds in the offshore environment are profoundly different from those found over land (Pryor and Barthelmie, 2002). The dramatic difference in roughness length offshore compared to over land is one of the primary reasons the marine boundary layer is vastly different from the terrestrial boundary layer. In order to better understand the variations in boundary layer winds with an offshore versus

Table 2.1: Table showing a selection of approximate surface roughness lengths for various terrain types. Adapted from [Manwell et al. \(2010\)](#).

Terrain description	z_0 (mm)
Calm open sea	0.20
Blown sea	0.50
Lawn grass	8.00
Rough pasture	10.00
Crops	50.00
Few trees	100.00
Many trees, hedges, few buildings	250.00
Forest and woodlands	500.00
Suburbs	1500.00
City centers	3000.00

onshore surface roughness, it is perhaps best to see a graphical wind profile (Figure 2.1a). These three profiles are generated using Equation 2.1, with an “observed” wind speed of 10 m s^{-1} at 90 m height (a typical offshore wind platform hub height). It is clear that the vertical wind speed profile for a roughness length of a rough sea (0.50 mm, blue line) has less variation with height than the land-based wind speed profiles. This indicates that the power produced by an offshore turbine is less dependent on height above the surface than onshore turbines, since the wind speed profile is more uniform at typical hub heights. The variation in the wind profiles is perhaps better seen in Figure 2.1b, where all of the profiles have been set to a wind speed of 15 m s^{-1} in the free atmosphere, which is set to a height of 500 m. It is clear that at higher roughness lengths, the wind speeds drops off much more rapidly near the land surface, while over open sea, the profile is much more uniform.

The log law relationship outlined above is a good overall approximation of the wind profile within the atmospheric boundary layer for neutrally buoyant atmospheres. In [van Wijk et al. \(1990\)](#), the authors refine the log law relationship to take overall atmospheric stability into effect. The corrected log law, which they describe as the

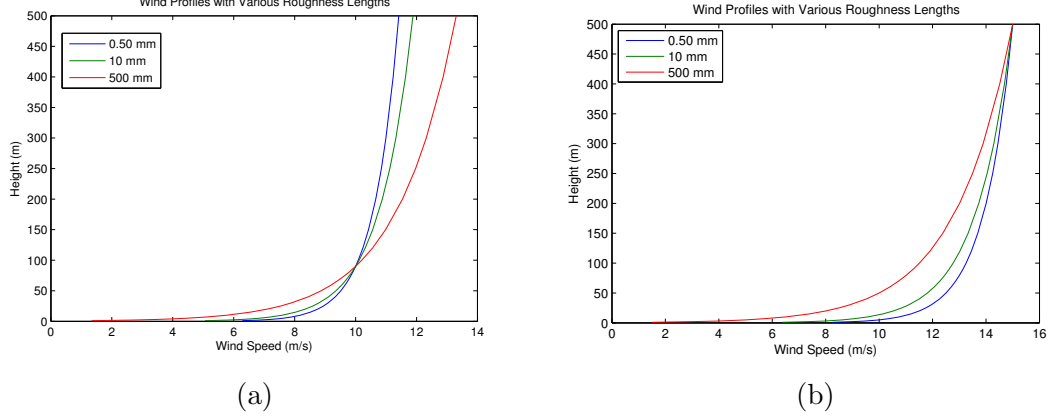


Figure 2.1: Wind speed profiles calculated using 3 different values for surface roughness length. (2.1a) shows all three profiles intersecting at a 10 m/s wind speed at 90 m height. (2.1b) shows all three profiles sharing the same wind speed in the free atmosphere at 500 m of 15 m/s.

adiabatic method, is described as:

$$U(z) = U(z_r) \cdot \left[\ln \left(\frac{z}{z_0} \right) - \Psi_m \left(\frac{z}{L} \right) \right] / \left[\ln \left(\frac{z_r}{z_0} \right) - \Psi_m \left(\frac{z_r}{L} \right) \right], \quad (2.2)$$

where L is the Monin-Obukhov length (described below in Equation 2.5), and Ψ_m is the integral of a gradient function for wind speed, $\phi_m = [1 - 16(z/L)]^{-1/4}$, which varies according to the stability of the atmosphere as determined by the sign of L :

$$\Psi_m = \begin{cases} 2 \ln \left(\frac{1+x}{2} \right) + \ln \left(\frac{1+x^2}{2} \right) - 2 \tan^{-1} x + \frac{\pi}{2} & \text{for } L < 0 \text{ (unstable)} \\ -5 \left(\frac{z}{L} \right) & \text{for } L > 0 \text{ (stable),} \end{cases} \quad (2.3)$$

where $x = [1 - 16(z/L)]^{1/4}$. They furthermore evaluate that for very stable conditions, where $z/L > 0.5$,

$$\Psi_m = -0.7 \left(\frac{z}{L} \right) - \left[0.75 \left(\frac{z}{L} \right) - 10.72 e^{-0.35(z/L)} \right] - 10.72 \quad (2.4)$$

is an even better approximation of this function.

The Monin-Obukhov length describes the effect of buoyancy on turbulent flows

in the atmospheric boundary layer. It is expressed by [van Wijk et al. \(1990\)](#) as:

$$L = \frac{u_*^2 T}{g\lambda\theta_*[1 + 0.00061 T(c_p/\lambda B)]}, \quad (2.5)$$

where $g = 9.81 \text{ m s}^{-2}$ is the acceleration due to gravity; T is the absolute air temperature (in K); c_p is the specific heat of water at constant pressure; λ is the latent heat of vaporization; u_* is the friction velocity; $\theta_* = H_0/(\rho c_p u_*)$ is known as the temperature scale with H_0 representing sensible heat flux and ρ the air density; and B is a quantity known as the Bowen ratio. The Bowen ratio is the ratio between sensible heat flux (H_0) and latent heat flux (λE), that is $B = H_0/\lambda E$. A small Bowen ratio ($B < 1$) indicates that more surface energy is passed to the atmosphere as latent heat; a large Bowen ratio ($B > 1$) indicates that the majority of the energy passed to the atmosphere is sensible heat.

The authors applied both the diabatic method and the standard log-law method to a variety of situations found in the North Sea, and found that there was little difference between the two methods in unstable and neutral atmospheric conditions. However, in very stable conditions, they found that the diabatic method performed considerably better relative to observations.

More recently, [Archer and Jacobson \(2003\)](#) strove to improve the use of both the log law relationship (Equation 2.1) and another extrapolation approach, commonly called the *power law*:

$$U(z) = U(z_r) \left(\frac{z}{z_r} \right)^\alpha, \quad (2.6)$$

where α is the power law exponent, commonly considered to be $\alpha = 1/7$. The authors point out that both of these techniques rely on seemingly arbitrary constants (z_0 and α), and propose a least-squares method to estimate these values using atmospheric sounding data. Essentially, the authors calculate the best-fitting values for z_0 and α using the 3 lowest observations in a sounding, and then use these parameters to extrapolate wind at hub height for nearby surface stations. This technique provided better results for wind at hub height than standard values of $z_0 = 0.01 \text{ m}$ and $\alpha = 1/7$

in 60% of the cases studied.

Furthermore, [Archer and Jacobson \(2003\)](#) evaluated two other meteorological situations in which these approaches fail: when the wind speed is actually decreasing with height, and when the wind speed at the observation height is zero but the wind is blowing at hub height. For the first case, they use a linear profile estimation:

$$U(z) = C + Dz, \quad (2.7)$$

with parameters C and D calculated using a least-squares technique on the sounding data, as above. For the second case, they have a modified log law that removes the dependence on $U(z_r) = 0$ which results in 0 wind at all heights when using the standard log law:

$$U(z) = A + B \ln(z), \quad (2.8)$$

with parameters A and B being calculated using their least-squares technique.

Further refinement of the theoretical representation of the wind speed profile was done in [Archer and Jacobson \(2005\)](#) by adding two more extrapolation techniques for two more unique situations. The first situation involves physically unrealistic cases where the wind speed calculated at hub height is greater than that observed in the sounding measurement taken above hub height (z_2), and involves calculating a modified friction coefficient based on forcing the power law curve through the observed sounding wind speed at z_2 :

$$\alpha = \ln \left[\frac{U(z_2)}{U(z_r)} \right] / \ln \left[\frac{z_2}{z_r} \right]. \quad (2.9)$$

The second situation involved cases where the sounding was almost constant above z_2 , but had a sharp increase in speed below z_2 . Previously, the log law relationship provided the best estimate of wind speed at hub height; [Archer and Jacobson \(2005\)](#) replace this with a linear relationship:

$$U(z) = U(z_r) + F(z - z_r), \quad (2.10)$$

where

$$F = \frac{U(z_2) - U(z_r)}{z_2 - z_r}. \quad (2.11)$$

Combined, the 6 techniques established by [Archer and Jacobson \(2003\)](#) and [Archer and Jacobson \(2005\)](#) provided excellent results in estimating the available wind resources within the United States, and worldwide. While these techniques were used for mostly onshore locations, the lessons learned here are highly applicable to the study of offshore boundary layer dynamics.

2.2 Offshore Wind in the Northeast United States

Offshore wind power is widely recognized as being one of the greatest potential sources of carbon-neutral energy available to those living in the heavily populated northeast United States. [Kempton et al. \(2007\)](#) found that along the Middle Atlantic Bight from Massachusetts to North Carolina, there is enough wind resource to produce an average 330 GW of electricity, greater than the combined electricity, light vehicle, and building fuel use at that time. This serves to highlight the importance of offshore wind power to future power production in the United States. In particular, it emphasizes the need to evaluate wind power production from a regional perspective.

2.2.1 Resource Assessments

A number of studies have evaluated and quantified the potential offshore wind resource for the Mid-Atlantic and Northeast states. The first serious study of the future of offshore wind in the United States was conducted by the National Renewable Energy Laboratory (NREL) starting in 2003 ([Musial and Butterfield, 2004](#)), and included a resource assessment of the New England states. Following that, the [Garvine and Kempton \(2008\)](#) study examined the wind resources available along the entire Middle Atlantic Bight, and concluded that the wind along the bight is both strong enough and constant enough to make it ideal for the development of offshore wind farms. The authors made special note of the fact that the more wind farms that are constructed, and the farther apart that they are, the more consistent the overall power production will

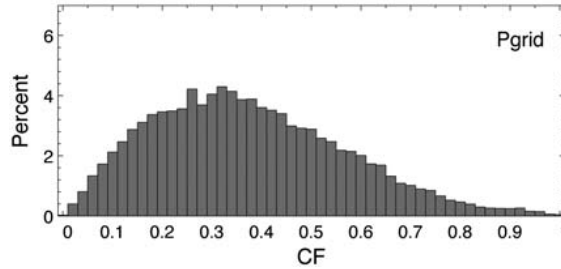


Figure 2.2: Histogram of capacity factor (CF) for all 11 wind farms combined in the [Kempton et al. \(2010\)](#) study. Figure reproduced from [Kempton et al. \(2010\)](#).

be. [Kempton et al. \(2010\)](#) examined this further with a situation where hypothetical wind farms were sited at 11 offshore locations along the United States' eastern coast, ranging from Maine to the Florida Keys, a distance of about 2500 km. By evaluating wind farm performance during a variety of synoptic-scale weather features over a 5-year time period, they found that the power output along the coast never dropped to zero; at least one of the farms was producing power at all times (see [Figure 2.2](#)).

NREL has continued to put together comprehensive reports on the available offshore wind resource in the United States since 2003 ([Schwartz et al., 2010](#); [Musial and Ram, 2010](#)). These assessments rely upon mesoscale modeling to evaluate the resource potential, which is validated with a limited number of available observations in the offshore region. The 200 m resolution of the model used in the NREL assessments allows for reasonable confidence in the results, despite the lack of 90 m hub height observations. [Musial and Ram \(2010\)](#) estimated that the total available wind resources directly off Delaware out to 50 nm was 14.7 GW, without excluding any area for other ocean uses such as shipping or environmental concerns. [Dhanju et al. \(2008\)](#) honed in on the Delaware offshore resource and considered exclusion zones and ocean depth, and found an available resource of 5200 MW annually, on average, which is more than 4 times the average state consumption. [Dvorak et al. \(2012\)](#) also conducted mesoscale modeling of the East Coast in order to evaluate the available offshore resource and included a full 5 years worth of model results, finding overall capacity factors between 40% and 50% from Virginia to Maine. It also examined the seasonality of the wind resource,

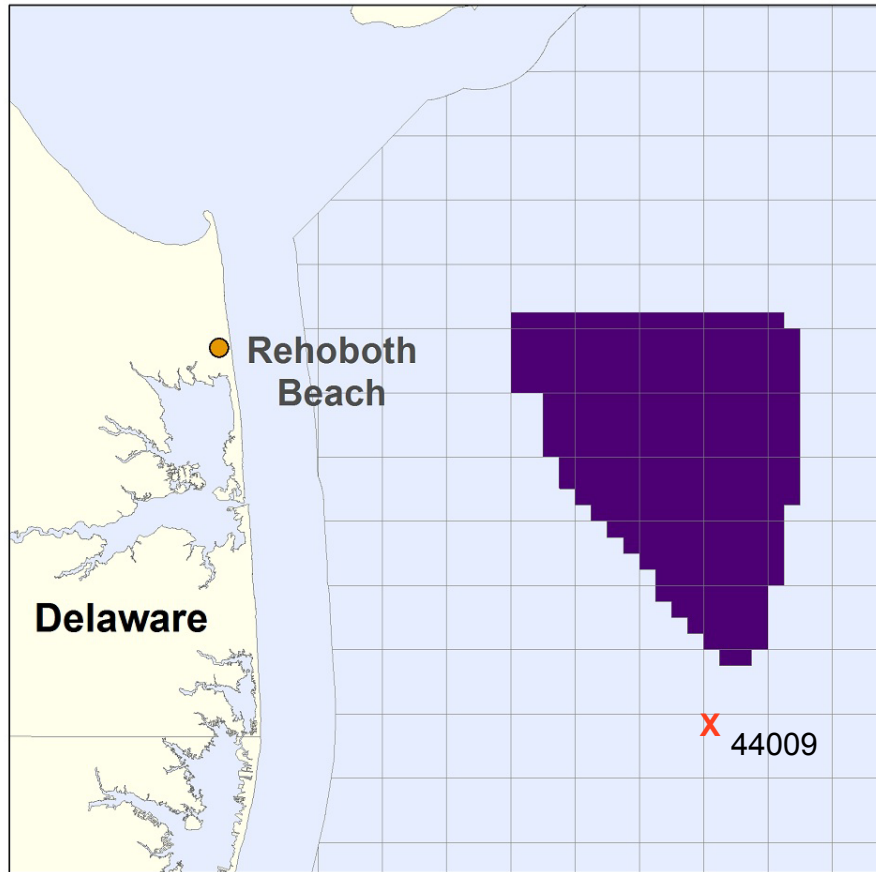


Figure 2.3: Map depicting the Delaware Wind Energy Area in purple, as specified in Bluewater Wind Delaware’s lease from the Bureau of Ocean Energy Management. The location of Buoy 44009 is shown by the red X. Figure adapted from [Bureau of Ocean Energy Management \(2015\)](#).

since wind conditions in the Delaware offshore region vary with season ([Hughes and Veron, 2015](#)). Ultimately, in 2012, the Bureau of Ocean Energy Management (BOEM) within the U.S. Department of the Interior, leased out a block of ocean that became the Delaware Wind Energy Area (WEA), seen in [Figure 2.3](#), to Bluewater Wind Delaware, LLC ([Bureau of Ocean Energy Management, 2015](#)).

2.3 Synoptic Typing

There are several different ways to identify large-scale meteorological conditions, including synoptic typing. With this method, meteorological conditions are quantified

using a wide assortment of variables to characterize the state of the atmosphere, including wind velocity, temperature, humidity, cloud cover, precipitation, and many others. Due to the tremendous spatial and temporal variability of these meteorological characteristics, it can be a challenge to quantify overall meteorological conditions in an area using a single metric. *Synoptic typing* accomplishes this through principle component analysis of a large number of meteorological variables, and can be traced back to both computer-aided statistical relationships of sea level pressure by [Lund \(1963\)](#) and manual visual classification of weather maps in the United Kingdom by [Lamb \(1972\)](#). Over the years, advances in technology and statistical techniques have allowed these basic analyses to be significantly developed and improved ([Siegert et al., 2016](#), and references cited).

[Siegert et al. \(2016\)](#) utilize an eigenvector-based approach described by [Kalkstein and Corrigan \(1986\)](#) and [Yarnal \(1993\)](#) in order to classify the synoptic conditions for the Delaware area. The authors used temperature, dewpoint temperature, u and v wind components, pressure, and cloud cover data obtained from Philadelphia International Airport, taken at 4 times daily (0900, 1500, 2100, and 0300 UTC). The events were grouped into the four meteorological seasons (DJF, MAM, JJA, SON) for separate principal component analysis. The statistical PC analysis performed on the Philadelphia data was combined with a visual qualitative analysis of composite synoptic maps consisting of sea level pressure, 500 hPa geopotential height, surface air temperature, and surface precipitation rate. Their analysis resulted in various numbers of synoptic types in each season: 12 in winter, 13 for spring, 9 in summer, and 11 in the autumn. While the study was specifically applied to the Delaware region, the findings have broad regional applicability, and is of potential use throughout the northeast United States and the coastal region of those states ([Dowtin, 2012](#); [Siegert et al., 2016](#)).

These seasonal variations are composed of a total of 22 unique synoptic scenarios, with several scenarios occurring in multiple seasons: 6 low pressure systems, 4 high pressure systems, 1 cold front regime, 3 north/northwest predominant flow regimes, 3

south/southwest flow regimes, and 5 weakly defined scenarios. These can be described as follows, with synoptic type numbers in parentheses ([Dowtin, 2012](#); [Siegert et al., 2016](#)):

- *Low Pressure Systems*

1. Strong coastal low off of New Jersey featuring northerly winds over Delaware, observed in DJF (1017) and MAM (2020).
2. Weak coastal low in coastal North Carolina featuring easterly winds over Delaware, observed in DJF (1011), MAM (2011), and SON (4031).
3. Eastern Great Lakes low located near Lake Ontario with westerly winds over Delaware, in all four seasons (1034, 2033, 3036, 4009).
4. Midwestern low, with the center over Michigan delivering southwesterly winds over Delaware, in DJF (1035), MAM (2018), and SON (4033).
5. Strong low over coastal Maine featuring northwest winds over Delaware, in MAM (2006) and SON (4019).
6. Southeast Canadian low centered over Newfoundland resulting in northerly winds over Delaware, only in JJA (3004).

- *High Pressure Systems*

1. Strong high centered over the region in DJF (1014), MAM (2009), and SON (4013).
2. Moderate high centered over the region during DJF (1003), JJA (3007), and SON (4032).
3. Weak high centered over the region in DJF (1013) and MAM (2004).
4. New England high centered over New England featuring easterly winds in Delaware during DJF (1010) and SON (4035).

- *Cold Front*

1. Cold front passage off the Atlantic coast during all four seasons, which included a surface low pressure system in eastern Canada and a western high pressure system and provided for northwesterly winds in Delaware (1005, 2034, 3033, 4034).

- *Flow Regimes*

1. Northerly flow due to an eastern low and western high, in MAM (2008).
2. Strong northwesterly flow due to strong pressure gradient, in DJF (1031).
3. Weak northwestern flow in DJF (1033), MAM (2032), and SON (4036).

4. Southwesterly flow during DJF (1032), MAM (2031), and SON (4037).
 5. Weak southwest flow in MAM (2005) and SON (4038).
 6. Southerly flow during JJA (3031, 3032).
- *Weakly Defined*
 1. Calm conditions during MAM (2010).
 2. Very weak southerly flow during MAM.
 3. Weak flow associated with upper level trough during JJA (3002).
 4. Weak flow associated with zonal flow aloft during JJA (3011).
 5. Weak flow associated with upper level southern trough during JJA (3035).

Combined, these 22 types are sufficient to describe the overlying meteorological conditions found in Delaware throughout the year, roughly 99% of the time. There were tropical systems moving through the region less than 1% of the time, as well (Siegert et al., 2016).

While the synoptic types established by Siegert et al. (2016) were used to study hydroclimatological impacts, the technique is useful for any study examining daily meteorological phenomena over broader, climatological timescales. Grouping daily records into synoptic types provides for an effective way to select case studies that captures the variety of weather conditions. Furthermore, separating case studies by synoptic type also allows for focus on a particular weather condition, without confining the study to a few known events.

2.4 Ramp Events

As seen in many of the studies of the wind resource, there is a lot of variability in the wind speed and direction both temporally and spatially. This variability creates electrical grid management challenges due to the need to provide reliable power to meet demand at all times, yet have the flexibility to handle variable renewable resources (Cochran et al., 2014). A *ramp event* is a meteorological phenomenon characterized by a rapid change in wind speed. Ramp events can be challenging to predict, occur under a variety of synoptic conditions, and can cause particular issues for wind farm operators

(Kamath, 2010; Sevlian and Rajagopal, 2013). They can have significant impacts on wind power generation and electrical grid operations due to the substantial and abrupt change in wind speed. This abrupt change in available power may be exacerbated by any error in the forecasting of a ramp event, as allocation of generation resources relies on wind speed forecasts.

Ramp events occur in two ways: ramp-up events, when wind speeds are originally slow and increase over a relatively short period of time to a high wind speed; and ramp-down events, when the wind speeds start high and then rapidly decline. Ramp-up events are typically associated with a variety of intensifying weather conditions, including low pressure systems, low level jets, and thunderstorms (Sevlian and Rajagopal, 2013). Ramp-downs are associated with the departure of these weather conditions, and a concurrent, significant decrease in wind speed. This dissertation will be focusing on ramp-up events, since during the investigated time period and location, ramp-down events were typically more gradual, and therefore would be easier for the grid to compensate.

There are a number of criteria that can be used to define a ramp event. Kamath (2010) suggests two possible methods. The first method defines a ramp event as having occurred during the interval from time t to $t + \Delta t$ if the magnitude of change in power output from the start to the end of that interval exceeds a predefined threshold P_T :

$$|P(t + \Delta t) - P(t)| > P_T, \quad (2.12)$$

where P is the power output of the turbine or farm under consideration. However this method only looks at the end points of the interval. The second approach looks at the maximum and minimum within a given interval:

$$\max(P[t, t + \Delta t]) - \min(P[t, t + \Delta t]) > P_T. \quad (2.13)$$

Common convention is that the time period for the ramp, Δt , is typically between 15

minutes and 1 hour (Kamath, 2010). The selection of P_T is more complicated, since it can be either an absolute amount of power (i.e. 450 MW), or a percentage of the farm’s nameplate capacity, which allows for wind farms that may expand or install new equipment. Additional details on the criteria used for this dissertation are found in Chapter 4.

2.5 Wind Farms

As discussed in Section 2.1, wind turbines offshore interact with a vastly different environment than when they are on land. This section will discuss some of the factors that go into large-scale development of offshore wind energy. The first issue is the ongoing research into wake effects, which result from wind turbines extracting energy from the flow, and introducing additional turbulence. These wakes propagate through a wind farm, and negatively impact the power production of wind turbines deep within the farm. Next, a discussion on how large-scale wind deployment interacts with the electrical grid. Finally, wind turbines and ongoing development on improving turbine technology is discussed, along with differences between onshore and offshore turbines.

2.5.1 Wake Modeling

In a recent study, Barthelmie et al. (2010) found that power losses within two wind farms located offshore of Denmark, Nysted and Horns Rev, can be as great as 40% between the leading and rearmost columns of turbines. This can be clearly seen from observations, as shown in Figure 2.4. As such, being able to understand and model these wake effects is paramount to improving turbine efficiencies. Some of the earliest wind turbine wake modeling was conducted by Katic et al. (1986), which examined wake interactions between 2 modeled wind turbines using an idealized theoretical model. This model sought to evaluate the overall performance of the two turbines, and not necessarily accurately represent the entire wake velocity profile. Nevertheless, the calculations made using this model showed good agreement between more complex modeling and the limited available wind tunnel observations.

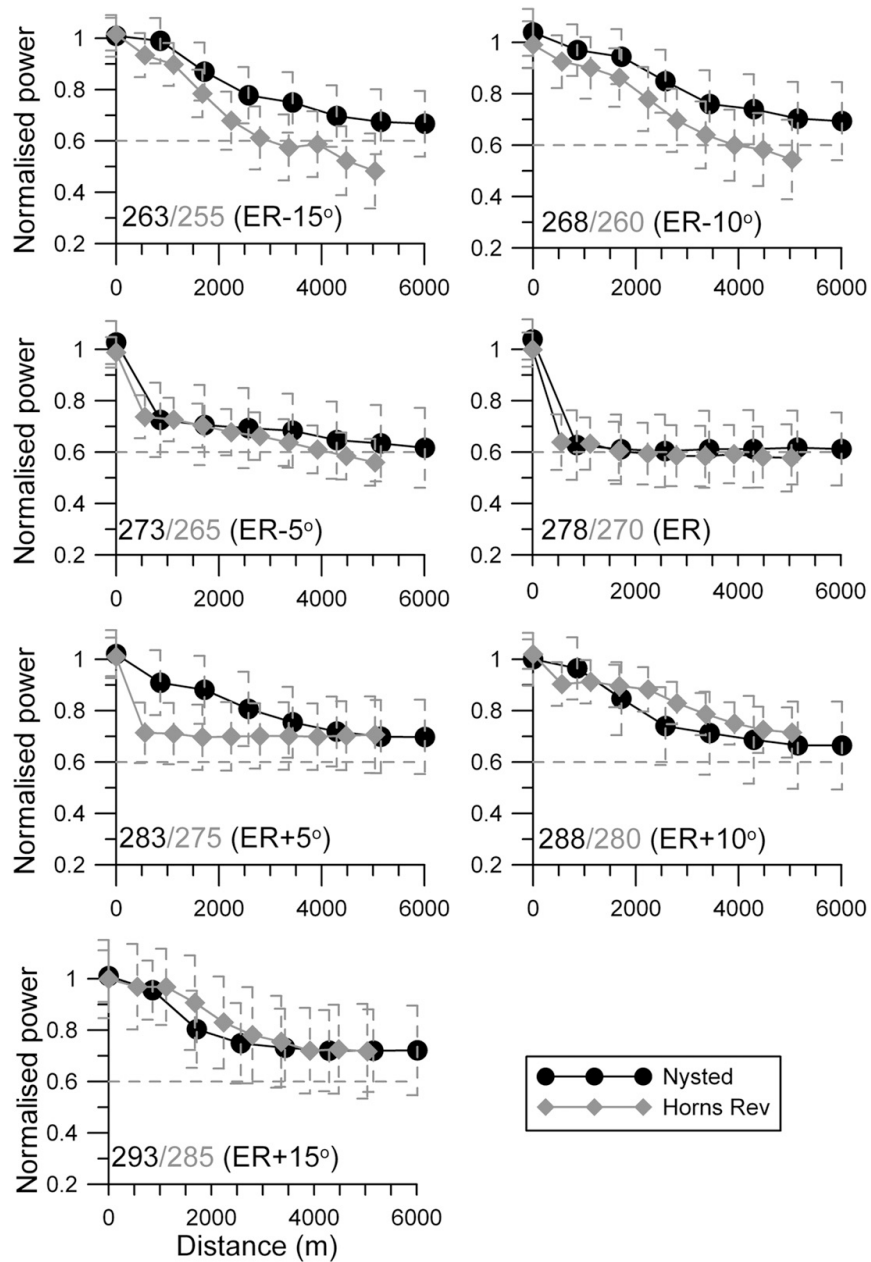


Figure 2.4: Figure depicting power losses experienced along rows of wind turbines within the Nysted and Horns Rev wind farms in Denmark. Note that the ER figure is for a row of wind turbines parallel to the wind direction; the other figures show losses experienced by rows at an angle to the wind direction. Figure from [Barthelmie et al. \(2010\)](#).

Ainslie (1988) examined wind turbine wakes and attempted to describe a numerical model for the wind field. He developed a relatively simple eddy viscosity turbulence model, which accounts for both the turbulent mixing caused by the turbines, and the ambient turbulence already in the atmosphere. There are several assumptions and simplifications made to allow for calculation using the relatively simple computers of the day: assume the wake is axisymmetric, fully turbulent, and with zero circumferential velocities. The flow field is assumed to be stationary with time, the pressure gradient within the fluid outside of the wake is assumed to be negligible, and beyond several rotor diameters downstream any mean quantity gradients will be much greater in the radial direction than the axial direction. This allows the inviscid Navier-Stokes equations to be simplified to a thin shear layer approximation:

$$U \frac{\partial U}{\partial x} + V \frac{\partial U}{\partial r} = -\frac{1}{r} \frac{\partial r \overline{uv}}{\partial r}, \quad (2.14)$$

where U and V are the axial and radial velocities, respectively, x and r are the axial and radial distance coordinates, respectively. The Reynolds stress cross-correlation is $\overline{uv} = -\epsilon \frac{\partial U}{\partial r}$, with ϵ being the eddy viscosity:

$$\epsilon = F[k_1 b(U_0 - U_C) + K_M], \quad (2.15)$$

where $k_1 = 0.015$ is a dimensionless constant calculated by Ainslie (1988) using wake decay observations from a wind tunnel. K_M is the eddy diffusivity of momentum, b is the width of the turbine wake, U_0 and U_C are the free stream wind speed and wake center line velocity, respectively, and F is defined based on the distance downstream from the turbine:

$$F = \begin{cases} 0.65 + \left(\frac{x - 4.5}{23.32}\right)^{1/3} & \text{for } x < 5.5 \text{ rotor diameters} \\ 1 & \text{for } x > 5.5 \text{ rotor diameters.} \end{cases} \quad (2.16)$$

Using this simple model, [Ainslie \(1988\)](#) found good agreement between his calculations and observations taken from a series of wind tunnel experiments. However, the shear stresses formed in the near wake were not yet well understood, and so were not well accounted for in his model. Additionally, this model was essentially a 2-dimensional model, and so ignoring any vertical variations in wind speed or turbulence. Finally, this model was sufficient for only a handful of turbines; modeling a large wind farm would not be accurate using this technique.

Wind farm modeling has come a long way since the 1980's. Two examples of models used in the wind industry include the Wind Atlas Analysis and Application Program (WAsP) ([Rathmann et al., 2006](#)) and WindFarmer ([Schlez and Neubert, 2009](#)). WAsP is a relatively simple linearized wind farm model, which allows for rapid wake calculations, while WindFarmer is a more state-of-the-art computational fluid dynamics (CFD) model, which explicitly models the flow at high resolution, but is more computationally expensive. Interestingly, WindFarmer uses an initial wake profile parameterization based on [Ainslie \(1988\)](#). A variety of studies have been performed evaluating the performance of these (and other) models ([Barthelmie et al., 2004, 2006, 2009](#)), using smaller wind farms or single turbine wakes for comparison. The general consensus of these studies was that wind farm-specific models tended to under-predict wake losses, while the more sophisticated CFD models tended to over-predict them.

Most recently, [Barthelmie et al. \(2010\)](#) performed a rigorous evaluation of four models, comparing their performance in wake modeling to observations taken from the two aforementioned large-scale wind farms in Denmark. The models the authors use include the two aforementioned models, plus two other CFD models: Wakefarm, which is another commercial wind farm model; and a Reynolds-averaged Navier-Stokes equation model from the National Technical University at Athens (NTUA), which is highly sophisticated, but not intended specifically for wind farm modeling. Overall, they found that the two industry-standard CFD models, WindFarmer and Wakefarm, showed very strong agreement with the observations; WAsP and the NTUA model performed reasonably, but some modifications could make them more accurate for

modeling the wake effects.

Large-eddy simulation (LES) of wind turbines and farms is also a common modeling technique to study both wake effects and power productivity. [Wu and Porté-Agel \(2011\)](#) used LES techniques to evaluate the modeling of wakes using both a rotating and a non-rotating actuator disk model of the wind turbine rotor in order to assess the impact of accounting for the rotation of the rotor when modeling the turbine wake. [Archer et al. \(2013\)](#) also used an LES model, combined with an actuator line model of the turbine rotors, to evaluate the impacts of staggering wind turbines in a wind farm layout. They found that staggering the turbine locations in the Lillgrund wind farm would have reduced array losses from 36% to 27%. While LES is a highly effective tool for studying wind turbine wakes, these models are computationally expensive, and are not suitable for a regional study. To this end, [Archer and Jacobson \(2013\)](#) assessed the need to better understand turbulent wake losses in offshore wind farms, and stressed the desire for efficient parameterizations of wind farms in larger-scale models than LES. They conclude that overly simplistic direct surface-based parameterizations extract momentum at the surface, rather than at hub height, which reduces their accuracy in understanding wake effects. Furthermore, [Fitch et al. \(2013a\)](#) concluded that these surface-based parameterizations such as those used in large-scale climate models are not sufficient for studying wind farm effects, since they often produce sensible heat fluxes of opposite sign from elevated momentum techniques implemented in mesoscale models. The elevated momentum techniques produce results similar to both observations and large-eddy simulations.

2.5.2 Interfacing with the Grid

Wind energy interacts with electrical grid operations in a somewhat different manner than more steady and predictable energy resources, such as nuclear, fossil fuel, or hydroelectric power plants. Wind is by nature more variable and less consistent than these more traditional energy sources. As such, large-scale development of wind power requires careful consideration as to how it will be included in grid operations.

The grid operator (regional transmission organization, RTO) that manages the electricity grid in the Delaware region is PJM Interconnection (PJM, 2016a). PJM manages and coordinates the transmission of electricity for a region spanning from New Jersey to northeastern North Carolina, and as far west as parts of Illinois and Indiana (see map in Figure 2.5). PJM serves as the wholesale electricity market between the power plants that produce the electricity, and the local utilities that deliver this electricity to the end user. They also ensure that supply meets demand at all times, thereby eliminating or minimizing blackouts or electricity surpluses.

In order to successfully meet load demand, PJM operates a “two-settlement” market structure whereby generating facilities and electricity purchasers (utilities) participate in both a day-ahead market, and a real-time market (PJM, 2016b). Under this system, initial bids for electricity generation that each power plant will be providing is due by 1200 local time the day prior to the day during which the electricity will be provided (the day-ahead market), and refined during a rebidding window from 1600–1800 local time. This day-ahead market allows PJM to balance the projected electricity demand with the least expensive generation sources in order to meet the anticipated load. On the operating day, the real-time market operates in 5-minute intervals throughout the day, refining and balancing the actual demand and supply, either reducing generation that is in excess of the anticipated load, or increasing generation using reserve generators which can quickly provide on-demand power if there is an unexpected increase in load demand (PJM, 2016c)¹. The day-ahead market can be challenging for wind operators, due to the much more variable nature of wind, as opposed to the more predictable conventional energy sources of nuclear, hydro, and fossil fuels.

Wind energy is a small, but growing, portion of the electricity generated in the PJM system. During 2015, installed wind capacity grew from 6601.7 MW on 31 December 2014 to 6781.7 MW on 31 December 2015, while overall PJM generation

¹ When the work of this dissertation was initially conducted, the timeframe for the day-ahead market in PJM functioned as indicated. However, as of the latest operating manual (PJM, 2016c, revision 80), the timeframe for the day-ahead market has shifted to require initial bids to be due at 1030 local, with the rebidding period from 1330–1415. This change took effect on 1 April 2016.

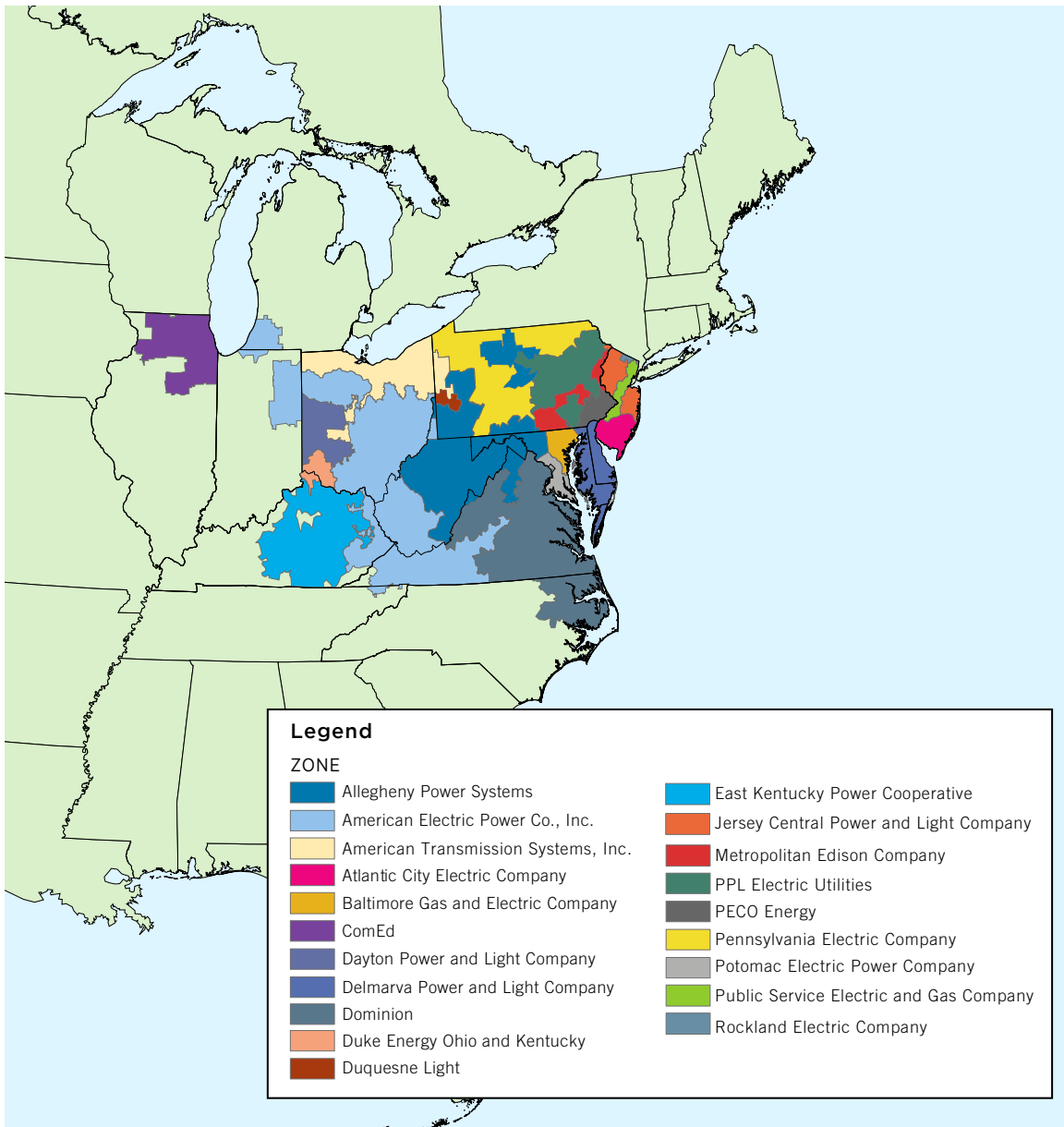


Figure 2.5: Map depicting the geographical area operated under PJM Interconnection and the various utility companies that constitute the PJM region, as of 9 May 2016. Reproduced from PJM (2016a).

capacity declined from 201.7 GW to 187.7 GW over the same time period, ultimately accounting for 3.6% of the installed generation capacity ([Monitoring Analytics, 2015, 2016](#)). In terms of future growth, as of 31 December 2015, there is 15 698.8 MW of wind capacity in the queue for construction by 2024, which is 18.4% of the 85 323.1 MW total generation capacity queued for construction by 2024. By 2020, PJM is projected to have 12 757.3 MW of installed wind generation capacity, amounting to 9% of their generation capacity ([Monitoring Analytics, 2016](#)). As usage of wind within PJM increases, greater attention will need to be paid to both the predictability of wind and possible market adjustments of the grid operations to handle more variable electricity generation. This is due to the fact that unanticipated supply changes, such as those caused by sudden and unpredicted changes in wind conditions, require grid operators to compensate for this through grid management techniques such as demand management, importing or exporting power from other transmission networks, or through the use of rapidly responding backup generators, frequently using natural gas ([Cochran et al., 2014](#)). The level and type of these responses will vary, since load is highly variable, peaking during the summer months, and reaching minima in the overnight hours ([Figure 2.6](#)). The necessary response must be dictated by the predictable load demand and the less predictable renewable generation, such that demand is always met without a surplus in supply.

2.5.3 Wind Turbine Designs

Wind turbines come in a range of sizes with a variety of technical specifications, with the intent of serving different meteorological conditions or local needs, as well as variations based on whether they are installed on land or in the water. Wind turbines come in a variety of designs ([Manwell et al., 2010](#)), among them the most common being:

- Small, sub-MW machines meant for small-scale or residential installations.
- Vertical axis (VAWT) machines, with a series of blades that rotate around a single, vertical axis.

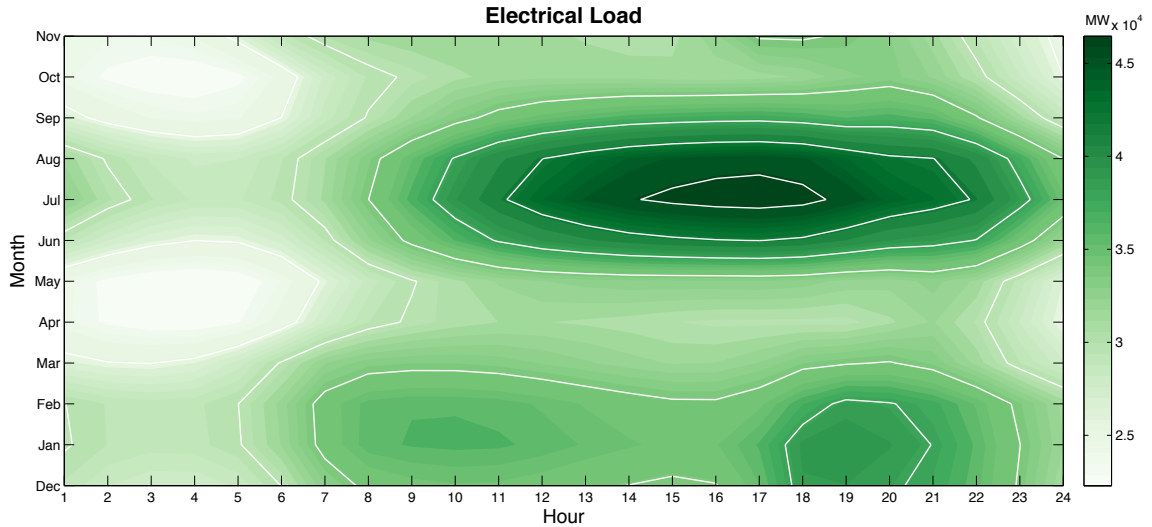


Figure 2.6: Illustration of the electricity demand (load) in PJM Interconnection from 2005-2011, shown as a function of hour of the day, plotted versus the month of the year. The darker colors indicate a greater electrical load.

- Large, MW-scale horizontal axis (HAWT) machines with large airfoil blades (often 3) that rotate around a single axis (hub) mounted atop of a tall structure.

For the intents of this research, the focus will be on conventional horizontal axis, single hub, large-scale wind turbines intended for offshore installation. Offshore turbines are often considerably larger than their onshore counterparts, which are limited in size due to practical reasons. When constructed offshore, the parts used to assemble the turbines on-site (tower sections, blades, etc.) are not constrained by what can be brought in via road by truck, as land-based turbines are. This allows for much greater capacity for each machine, presently up to 8 MW such as the Vestas V164 ([Vestas Wind Systems A/S, 2011](#)) used in Chapter 4, but even larger wind turbines are being considered ([Steel, 2015](#)).

Offshore wind technology has grown tremendously in recent years, employing a variety of different construction techniques and design considerations ([Breton and Moe, 2009](#)). The most common offshore wind turbine consists of a monopile construction, with a single tower driven into the undersea floor. Another common foundation structure is the jacket foundation, which includes several smaller piles driven into the

sea floor, supporting a steel substructure that often meets with the single tower of each turbine above the water’s surface. There are also other special foundation types, such as suction buckets which rest on the sea floor, anchored in place by the removal of water from within and under the bucket. Other recent developments include floating turbines, with no foundation other than cables that anchor the floating platform to the bottom. These floating structures are vital to the development of offshore wind in regions that do not benefit from a shallow continental shelf, such as the western coast of the United States.

For this dissertation, a number of wind turbines were considered for study, without taking the foundation type into account. Foundation considerations are largely a “below water” concern, requiring careful consideration of factors such as the local geology, and are therefore beyond the scope of this dissertation. As such, the determination of the appropriate wind turbines was made based on the availability of the necessary data on turbine performance (some of which is company proprietary information and is therefore difficult, if not impossible, to obtain), along with consideration of the wind climatology of the offshore Delaware region and how those turbines would perform given their power curve and the wind distribution.

2.6 WRF Model Description

The Advanced Research WRF (ARW) is a mesoscale research and numerical weather prediction model that is adaptable to study phenomena on scales ranging from sub-kilometer grids to global simulations (Skamarock et al., 2008). WRF is capable of being run effectively on both desktop computer configurations and multiple cores of massively parallel modern supercomputers. As such, it is an ideal system for use on the University of Delaware’s community cluster computing environment (mills and farber, University of Delaware, 2012). The ARW dynamical core consists of a suite of fully compressible non-hydrostatic equations, with a hydrostatic option, along with a wide array of physics options for various advection schemes, planetary boundary layer dynamics, radiative transfer, and cloud microphysics, to name a few. The model

can also handle several nested grids, with both one-way and two-way nesting options. It also includes the ability to ingest a variety of input data as initial and boundary conditions during model runs, including NCEP reanalysis data, GFS model output, and even independent data sources (NCAR, 2012). These model forcing data are processed for WRF use by using the WRF Preprocessing System (WPS), and includes programs which unpack and interpolate the data for WRF’s needs.

The ARW can be run in one of two states: either an *ideal* case evaluation, or in *real* mode, which is meant to use real-world atmospheric data to drive it. The model package as provided by NCAR includes a variety of idealized cases, which are meant to help evaluate the performance of WRF under specific conditions, before using the model for real-world scenarios. For this dissertation work, the idealized mode is used for the wind rose experiment described in Chapter 3, and the real mode is used for both the ramp study in Chapter 4 and the regional project in Chapter 5. Additional details on the specific model setup for each project are located in the respective chapter.

Version 3.3 of ARW was the first to include a detailed wind farm parameterization described by Fitch et al. (2012) and can be used in both the idealized and real versions of WRF. This parameterization functions by calculating the energy balance within the atmospheric boundary layer in and around a modeled wind farm. It first calculates the total kinetic energy available to the wind farm, and how much kinetic energy is lost due to the drag force from the wind turbine(s) within a given grid cell. The parameterization then uses published efficiency parameters of a given wind turbine (Fitch et al. (2012) uses the REpower Systems 5M wind turbine (REpower Systems AG, 2011)) to calculate the amount of this kinetic energy that the turbine converts into electrical energy. The total fraction of kinetic energy extracted from the atmosphere by the wind turbine is quantified by the thrust coefficient (C_T), while the fraction of this kinetic energy converted to electrical energy is quantified by the power coefficient (C_P), with $C_T > C_P$. The remaining energy loss after the electricity extraction is then converted into turbulent kinetic energy (TKE) and dissipated back into the boundary layer, that is $C_{TKE} = C_T - C_P$. To understand how the parameterization does this,

it is necessary to begin with an equation for the drag force induced on an individual turbine, using:

$$\mathbf{F}_{\text{drag}} = \frac{1}{2} \int_{A_R} C_T \rho |\mathbf{V}| \mathbf{V} \, dA, \quad (2.17)$$

where $\mathbf{V} = (u, v)$ is the horizontal velocity vector, ρ is the air density, and A is the cross-sectional rotor area. Keep in mind that the thrust coefficient is a function of the wind speed, that is $C_T = C_T(|\mathbf{V}|)$. Then, integrate over the area of the rotor (A_R) because the wind speed varies over the surface of the rotor. From this, the rate of change of kinetic energy (KE_{drag}) for each turbine can be calculated using:

$$\frac{\partial KE_{\text{drag}}}{\partial t} = -\frac{1}{2} \int_{A_R} C_T \rho |\mathbf{V}|^3 \, dA. \quad (2.18)$$

From this, the rate of loss of kinetic energy within one grid cell i, j and at model level k is calculated using:

$$\frac{\partial KE_{\text{drag}}^{ijk}}{\partial t} = -\frac{1}{2} N_t^{ij} \Delta x \Delta y C_T \rho_{ijk} |\mathbf{V}|_{ijk}^3 A_{ijk}, \quad (2.19)$$

where Δx is zonal grid size, Δy is meridional grid size, and N_t^{ij} is a horizontal density of wind turbines within that calculated grid cell. It is important to note that the model does not account for wake effects between multiple turbines within the same grid cell.

In order for this to have meaning, an equation for the total kinetic energy loss within a grid cell must be defined, which is:

$$\frac{\partial KE_{\text{cell}}^{ijk}}{\partial t} = \rho_{ijk} \Delta x \Delta y |\mathbf{V}|_{ijk} \frac{\partial |\mathbf{V}|_{ijk}}{\partial t} (z_{k+1} - z_k), \quad (2.20)$$

where z_k and z_{k+1} is the height of the bottom of model level k and the height of the top of this same level, respectively. To find momentum tendency, which is the quantity the model needs, it is assumed that the kinetic energy loss in a cell is caused entirely by the wind turbines, which allows the right hand side of equations 2.19 and 2.20 to

be set equal to one another, obtaining:

$$\frac{\partial |\mathbf{V}|_{ijk}}{\partial t} = -\frac{N_t^{ij} C_T |\mathbf{V}|_{ijk}^2 A_{ijk}}{2(z_{k+1} - z_k)}. \quad (2.21)$$

Finally, the power extracted by the turbines and converted into electrical energy can be calculated using the power coefficient C_P and the following (Fitch et al., 2013b):

$$P_{ijk} = \frac{N_t^{ij} C_P \rho_{ijk} |\mathbf{V}|_{ijk}^3 A_{ijk} \Delta x \Delta y}{2}. \quad (2.22)$$

Furthermore, the remaining power extracted by the turbine is converted into turbulent kinetic energy, calculated using $C_{TKE} = C_T - C_P$:

$$\frac{\partial TKE_{ijk}}{\partial t} = \frac{N_t^{ij} C_{TKE} \rho_{ijk} A_{ijk} \Delta x \Delta y}{2}. \quad (2.23)$$

As one final point, the wind farm parameters can be defined as either a simple wind farm defined by uniform characteristics, or with each turbine within the farm defined individually in a separate input file. Care must also be taken to use the best available turbine specifications with the model, typically directly from the turbine manufacturer (Fitch, 2015).

2.7 Meteorological Data Descriptions

For the work outlined within this dissertation, a variety of meteorological data sources were used for case study selection, model forcing, and model validation. These data include observational data and established model output or reanalysis data.

2.7.1 Observational Data

In the Delaware offshore region, there is sparse observational information with which to conduct a thorough resource assessment. One of the prime sources of information is the network of buoys operated by the National Data Buoy Center (NDBC) of the National Oceanic and Atmospheric Administration (NOAA) (National Oceanic and

[Atmospheric Administration, 2016](#)). These buoys gather a variety of oceanographic and meteorological data, which vary depending on the buoy. Some are strictly ocean buoys and gather ocean data, such as wave heights, periods, predominant wave directions, and other oceanic variables. Other buoys also contain meteorological observation stations to measure atmospheric variables, such as temperature, pressure, wind velocity, and others.

The region offshore of the Delaware coast is home to NOAA Buoy 44009, located at 38.461°N , 74.703°W , about 30 km east of Fenwick Island, DE, approximately due east of the Delaware/Maryland border (see Figure 2.3). Fortunately, it is a combined meteorological/oceanographic buoy, reporting most observations hourly, as ASOS does. It measures wave characteristics including the water temperature at 0.6 m below the waterline, significant wave height, wave period, wave direction, and characteristics of both the swell and wind driven waves, along with also providing spectral wave information. Above the waterline, it measures air pressure at sea level, temperature and dewpoint at 4 m, and winds at 5 m. The winds reported during the hourly observation report is an 8-minute average wind speed and direction during the last 8-minute interval, in addition to any gust information during that 8-minute interval. This hourly record is available online dating back to 1984.

In addition to these hourly observations, Buoy 44009 also records “continuous winds”. These observations are 10-minute wind averages, and are reported every 10 minutes, or 6 observations each hour. It also reports each hour’s gust data once at the end of the hour, along with the time of the gust; unlike the hourly observation, this gust could take place anytime during the hour. This data record is available dating back to 1999, with some gaps due to instrument failure or maintenance. Most of these gaps are small, on the order of a day or less. However, there are 6 time periods where the buoy was non-operational for several weeks or more. It is this continuous wind record that is used as the primary observational data source for this dissertation.

2.7.2 Modeling and Reanalysis Data

As discussed in Section 2.6, the WRF model is capable of ingesting a wide array of initialization data, which it uses as both initial and boundary conditions for the model run. For the work detailed herein, the versatility of WRF’s input conditions is employed, using different forcing datasets depending on the specific questions to be addressed by the study.

For the ramp prediction study detailed in Chapter 4, several different forms of large-scale modeling data from the National Centers for Environmental Prediction (NCEP) are used to force WRF. Specifically the Global Forecast System (GFS, [Kanamitsu, 1989](#); [Kanamitsu et al., 1991](#)) and the North American Mesoscale (NAM, [Black, 1994](#)) products are used for the WRF Preprocessing System to generate initial and boundary conditions. Both sets of model output are publicly available through NOAA’s National Operational Model Archive and Distribution System hosted by the National Centers for Environmental Information (NCEI, formerly the National Climatic Data Center, NCDC) (NOMADS, [Rutledge et al., 2006](#)). Both of these models are used by NOAA, and indeed beyond the United States, as model guidance for daily weather prediction. The GFS provides global coverage and is run by NCEP every 6 hours. It provides model output at 3 hour intervals, out to hour 192 (8 days) at 0.5° resolution, and to hour 240 (10 days) at 1.0° resolution. It also provides 12-hour interval output at 1.0° resolution for hours 252 through 384 (16 days) ([National Centers for Environmental Information, 2016a](#)). The NAM model is a regional model for the North American continent and surrounding regions. It is also run 4 times a day, and provides 3-hourly model guidance out to 84 hours at 12 km resolution, or 60 hours at coarser resolutions ([National Centers for Environmental Information, 2016b](#)). Further details on the justification for the use of these model forcing datasets is found in Section 4.2.

The regional study described in Chapter 5 uses a different set of forcing data, since it is a study with different needs, further discussed in Section 5.2.2. For this study, the North American Regional Reanalysis (NARR, [Mesinger et al., 2006](#)) was used. The NARR dataset combines a vast array of observational data with model

results, going back as far as 1979, and is easily accessible through NCEI's NOMADS data server ([Rutledge et al., 2006](#)). The data are available in 3 h intervals for the North American continent and surrounding oceanic areas, utilizing a 32 km grid over the same domain as the NAM model. The production of this reanalysis product starts with a “first guess”, which is then adjusted by the 3-dimensional assimilation of available observational data, resulting in an analysis at the given time. This analysis is then used for a 3 h model integration, the final result of which is used as the “first guess” for the next time period. The assimilated observational data includes both surface observations and atmospheric observations, and include variables such as temperature, wind, pressure, sea and lake ice extent, sea surface temperature, and precipitation. Sources of the observational data include surface observing stations and buoys, aircraft and ships, rawinsondes and dropsondes, and satellite data. NARR is frequently used as forcing data for WRF, as it combines both observations and model data to provide realistic conditions on a known grid.

Chapter 3

IDEALIZED MODELING USING CLIMATOLOGY

The advantages of using WRF for mesoscale wind energy research has been established in Section 2.6. The first study, outlined in this chapter, is a feasibility and sensitivity study to determine WRF’s ability to model intra-farm interactions sufficiently well to be of value to study potential power productivity. This will involve using an idealized WRF configuration to examine the performance of several different wind farm array configurations under controllable atmospheric conditions.

The initial set of runs described are a series of different geometric-shaped wind farm arrays inserted into a simple WRF domain and allowed to run with a constant wind speed. This will allow for an assessment of some of the variables that impact the performance of a wind farm array due to the variable wake losses. Following that, a series of model runs are conducted using these geometries using 324 different wind speed and direction combinations in order to assess performance under a variety of wind conditions. This provides guidance towards designing two different wind farm arrays that could be used in the Delaware Wind Energy Area, based on the wind climatology of the region. Finally, these two farms are also modeled using the idealized WRF setup, in order to answer how these shapes might perform in a climatologically normal year. Specifically, this study seeks to address the questions of how the farm layout impacts the overall power production and what factors in these layouts contribute to any improvements.

3.1 Model Setup

As discussed in Section 2.6, the WRF model is a highly configurable mesoscale modeling suite, capable of running in both an idealized configuration, where the user

has control over all of the forcing conditions, and a real-world configuration, using observations and larger-scale models to force WRF. For the purpose of this set of experiments, the `em_seabreeze` idealized case will initially be used to evaluate the wind farm parameterization. This case is designed to allow the user to simulate a simple sea/land breeze in two dimensions (x and z). By removing the land component from the model parameterization and extending the domain into three dimensions (x , y , and z), it is possible to create an idealized offshore environment within which to model a wind farm.

A uniform westerly wind profile was created for the initial model runs by establishing a wind with only a u component, and leaving the v component as 0. This can then be used by WRF to evaluate the wind field within and around the sample wind farms. Additional wind fields will be used for the wind rose experiments described in Section 3.3. The Mellor-Yamada-Nakanishi-Niino Level 2.5 (MYNN2, [Nakanishi and Niino, 2006](#)) planetary boundary layer scheme is selected to handle the boundary layer physics, as the [Fitch et al. \(2012\)](#) wind turbine parameterization only works when using the MYNN2 PBL scheme. Additionally, a stable atmosphere will be used, based on the standard McClatchey mid-latitude atmospheric profiles ([McClatchey et al., 1972](#)). The use of a stable atmosphere is one limitation of this set of experiments; however, since these idealized runs are intended to demonstrate both WRF’s abilities and limitations for wind farm modeling and examine essential differences resulting from wind farm layout decisions, the use of a standard atmosphere is sufficient. Additional stability concerns will be addressed in the regional, real-world WRF runs discussed in Chapter 5.

3.2 Basic Wind Farm Shape Analysis

The initial experiment is intended to demonstrate the suitability of WRF for evaluating wind farm performance with more rigor than a simple resource assessment conducted without taking the impacts of the wind turbines themselves into consideration. Furthermore, it will evaluate how different wind farm array geometries may

influence the overall performance of the farm, and discuss what design factors may be significant when laying out an offshore wind farm.

3.2.1 Wind Farm Design

In order to evaluate basic wind farm array geometries, 5 different model wind farms are developed, with each wind farm including 36 5 MW wind turbines at 100 m hub height and with a $D = 126$ m rotor diameter, spaced 1 km apart. The first wind farm is a 6×6 turbine square (SQR) array, the simplest layout. Next are two rectangular arrays, both 4×9 turbines: one is a “tall” array (TLR), where the widest part of the farm faces into the wind; and the other is a “long” array (LGR), with the narrow part of the farm facing into the wind. The fourth layout is an equilateral triangular array with 8 turbines per side, and with the point of the triangle facing into the wind (EQT). The final format is a 6×6 diamond-shaped array (DMD), again with the point of the diamond facing into the wind. These final two arrays allow subsequent rows within the farm to be “staggered,” such that each trailing row has its turbines spaced within the gaps of the preceding row. A schematic of these 5 simple geometric wind farm layouts is shown in Figure 3.1.

With the wind farm characteristics defined, it is necessary to establish the model domain for these idealized runs. A 36×36 model grid, with 0.5 km grid spacing, is used, which makes the total domain 18×18 km, with a 2 s time step integration. Then, the wind farm is positioned in the center of the domain, spacing the turbine rows and columns each 1 km apart (approximately $8D$), so there is one grid point between each turbine row and column in both the x and y directions (this can be seen in Figure 3.1). The surface is defined within the model as being an open water surface. Vertically, the model has 40 layers, up to 10 km. The layers are spaced such that there is a large number of layers in the region of interest (< 250 m), with the layers getting thicker higher into the atmosphere. Then WRF is initialized with a uniform, constant in time, 13 m/s wind velocity ($u = 13 \text{ m s}^{-1}$, $v = 0 \text{ m s}^{-1}$) at all heights throughout the domain, and integrates for at least 90 minutes. The model begins to show a wake pattern

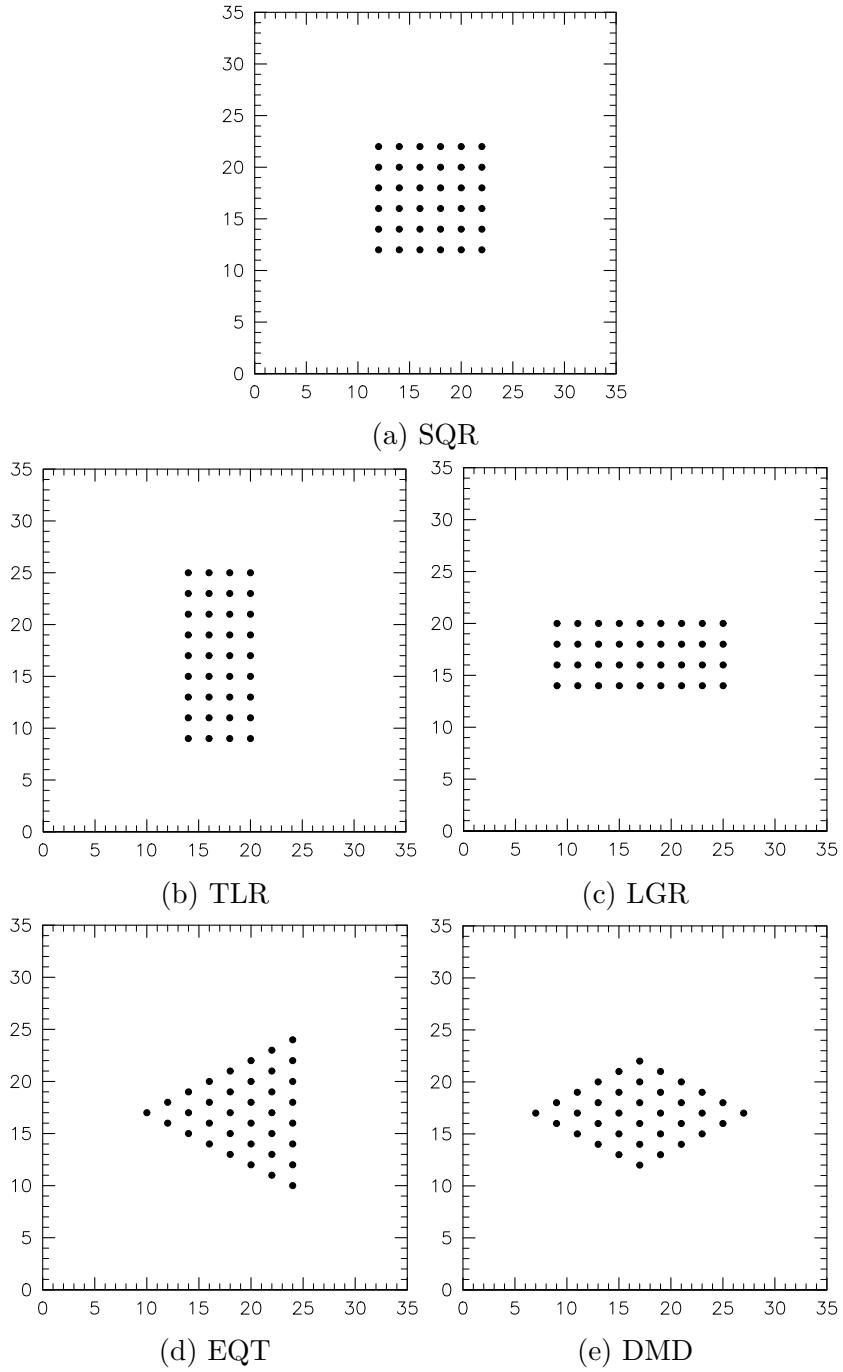


Figure 3.1: The five example wind farm layouts used in the idealized WRF simulations.

from the farms within the first 10 minutes of model integration, and as time continues, the wake pattern remains the same, although the overall wind speed within the entire domain slowly weakens. 90 minutes was selected as a representative time to illustrate the model’s performance since the wind speeds within the farm are high enough to be close to peak turbine performance, while not being so strong that all the turbines are producing maximum power even with the wake effects.

3.2.2 Idealized Model Results

In order to examine wind farm performance, the wind velocities at 100 m height is extracted from the model output, since this is a typical hub height of an offshore wind turbine. The resultant wind speeds within the model domain after 90 minutes of model integration is shown in Figures 3.2 and 3.3. At first glance, it can be seen that the diamond-shaped array (DMD, Figure 3.2e) experiences the most dramatic drop off in wind speed within the farm, and the tall rectangular array (TLR, Figure 3.2b) the least. However, it is necessary to perform a more rigorous analysis of these data to truly determine the wake impacts within the farm.

To do this, the wind speeds from the model are extracted at the location of each turbine, and compared to the power curve of the REpower 5M wind turbine (Figure 3.4, REpower Systems AG, 2011). This allows the calculation of the instantaneous power output of each wind turbine within the farm, and by summing them up, the total power production of each array configuration at this model time. A table summarizing these results is shown in Table 3.1.

As expected from the wind speeds, the tall rectangular array (TLR) experiences the least amount of power loss between the best-producing wind turbine and the worst, while the diamond shaped array (DMD) experiences the most dramatic loss of power. The tall rectangular array (TLR) also produces the most overall power, with the triangular array (EQT) performing second best. This is likely a direct result of the fact that there are more turbines on the leading edge of the triangular farm when compared to most of the other shapes, and only a couple turbines experience the lowest

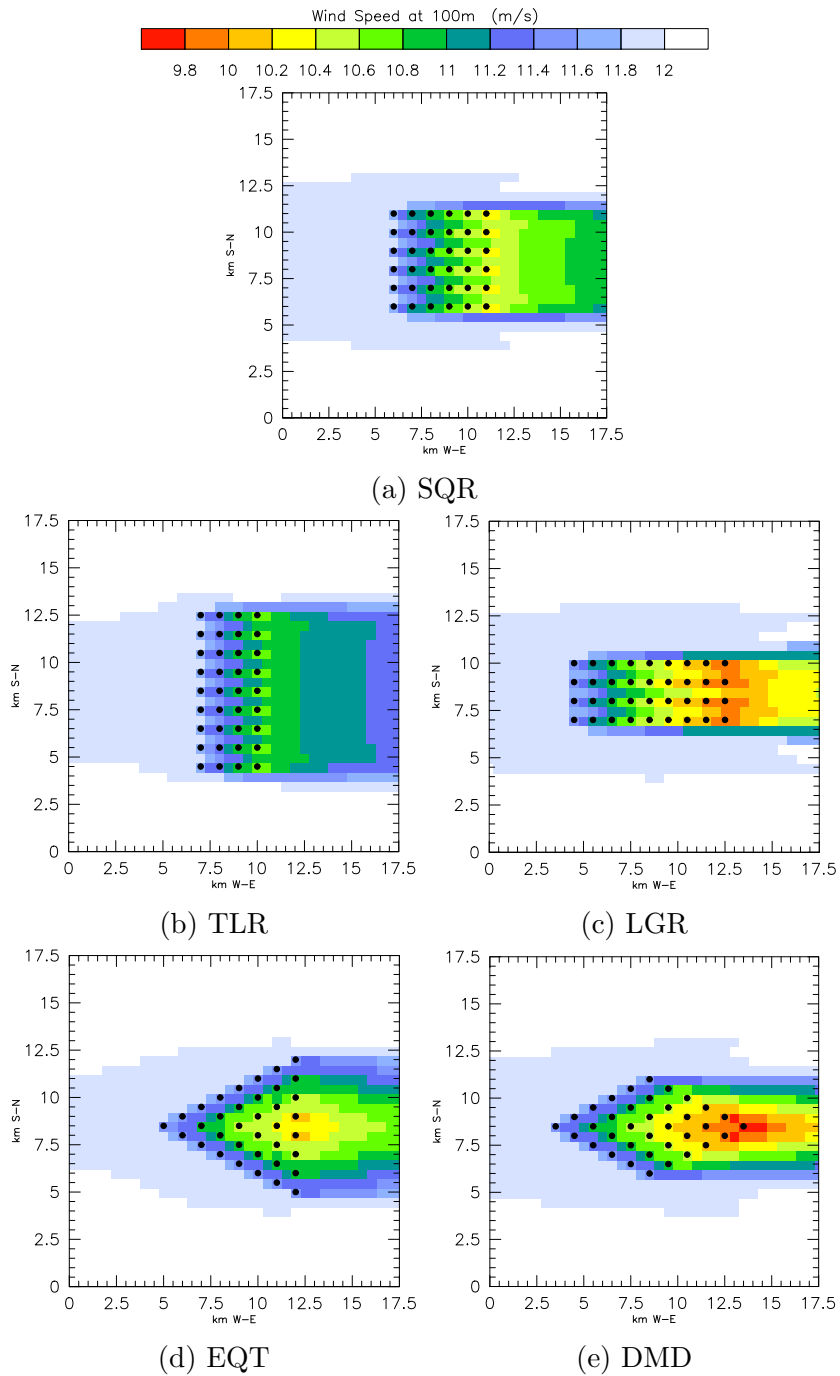
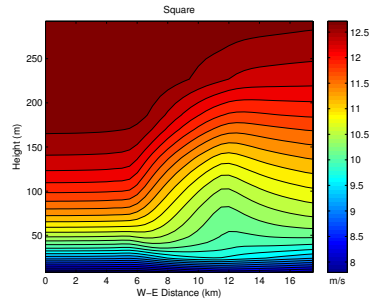
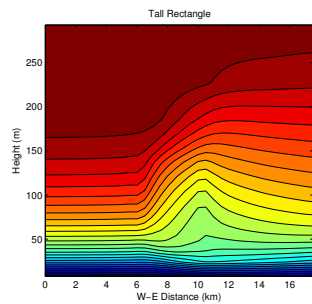


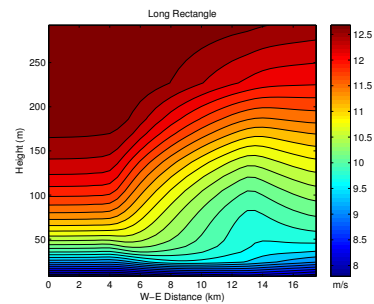
Figure 3.2: WRF model output for the 5 example farms, depicting wind speed at 100 m height after 90 minutes of model integration.



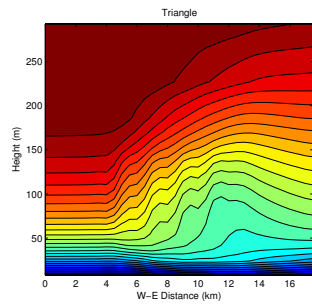
(a) SQR



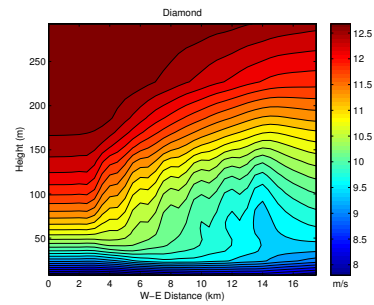
(b) TLR



(c) LGR



(d) EQT



(e) DMD

Figure 3.3: WRF model output for the 5 sample farms, depicting wind speed along a vertical slice through the center of each wind farm in the along-wind direction after 90 minutes of model integration.

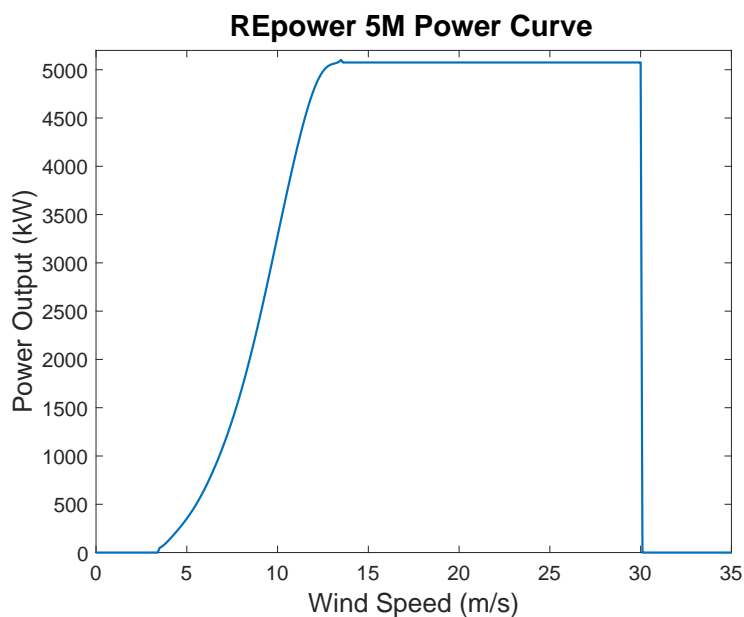


Figure 3.4: The published power curve for the REpower 5M wind turbine. It has a cut-in speed of 3.5 m s^{-1} , a rated speed of 13.5 m s^{-1} , and a cut-out speed of 30 m s^{-1} .

Table 3.1: Calculations of power output from the 5 simulated wind farms, using WRF predicted winds at 100 m hub height.

	SQR	TLR	LGR	EQT	DMD
Total Array Instantaneous Power Output (MW)	144.4	151.3	135.3	148.1	139.7
Array Daily Power Output (MWh)	3465	3632	3247	3555	3353
Best Turbine Instantaneous Power Output (kW)	4564	4564	4564	4564	4498
Worst Turbine Instantaneous Power Output (kW)	3541	3884	3102	3454	3014
Percent Loss from Best to Worst	22.42%	14.91%	32.04%	24.33%	32.99%

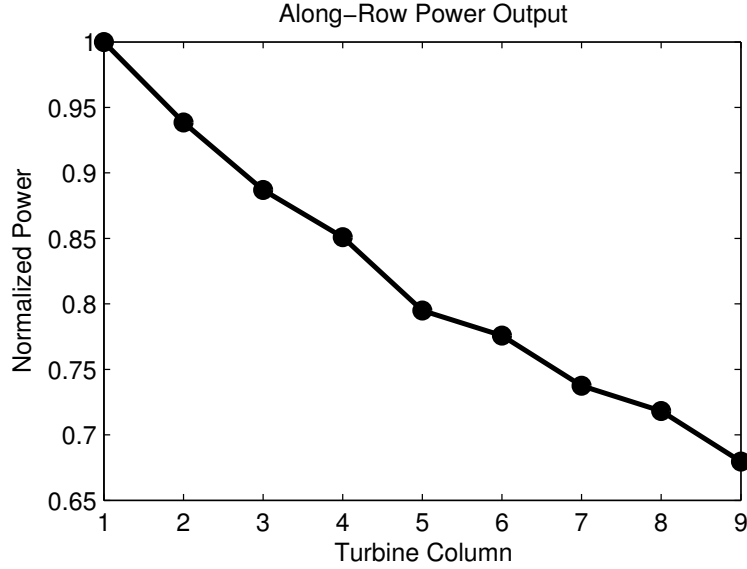


Figure 3.5: Normalized power output for a single row of the long rectangular array (LGR).

wind speeds; while the tall rectangle performs better, if a fifth column of turbines were added, the overall performance would likely suffer. These results appear realistic and similar to previous observations in existing wind farms (Barthelmie et al., 2010). In Figure 3.5, it can be seen how the normalized power output is reduced as the wakes propagate through the farm. However, these results show a more linear decline than that shown in Barthelmie et al. (2010), which shows a rapid decline from column 1 to 2, and slight declines approaching an asymptote around 0.6 (see Figure 2.4).

If a vertical profile of the wind speed in each of the farms is examined, as in Figure 3.3, it can be seen that as the wind propagates further into the farm, the wake effects expand vertically into the atmosphere, such that the higher wind speeds are found at higher altitudes than they were before. This suggests that it is worthwhile to pursue an investigation of how a change in vertical heights can improve the power output of the farm; it may be possible to “ride the wave” of higher wind speeds as it propagates upward. However, this may only be reasonable for the first couple of rows, before the change in height is too great to be practical for construction.

These results indicate that there is indeed benefit in changing the layout of

a wind farm in order to reduce wake effects and maximize power production. In particular the EQT array demonstrates that staggering of wind turbines with respect to the predominant wind direction, and having a triangular point in that wind direction to increase the number of leading edge turbines, improves the power production of the farm. However, this was only looking at one wind direction and speed; real world winds are highly variable. The next part of the study examines a more realistic distribution of winds.

3.3 Wind Rose Analysis

An initial assessment of the impact of these idealized farm layouts on the power production can be done using the climatological distribution of wind speed and directions from observations (e.g. the wind rose). A wind rose is a circular histogram, simplifying the visualization of the frequency distribution of winds based on both direction and speed. As a frequency distribution, it shows us what winds are predominant at a particular study site. Ultimately, this will allow for an evaluation of how a wind farm would perform in a particular location using wind observations from that location. The wind rose for Buoy 44009 shows the distribution of the wind speed in directions just offshore from the Delaware Bay from 1998-2012 (Figure 3.6). This wind rose sorts the wind data from the Buoy for a multiple year period into 10 degree directional bins, and shades it according to wind speed. The wind speed bins are selected to allow for analysis of wind farm production at all wind speeds in the power curve of the REpower 5M (Figure 3.4).

The wind speed bins shown in Figure 3.6 will be used to set the criteria for simulations of the power production of each layout using 2 m s^{-1} intervals along the spin-up portion of the power curve from cut-in speed of 3.5 m s^{-1} to the rated speed of 13.5 m s^{-1} . This 2 m s^{-1} resolution will be maintained up to 19.5 m s^{-1} , to capture the wind speed drop-off throughout the farm. Wind speeds above 19.5 m s^{-1} are grouped together in one bin, since at that speed, presumably the entire farm will be producing at full power until cut-out at 30 m s^{-1} . First the model is run with the wind velocities

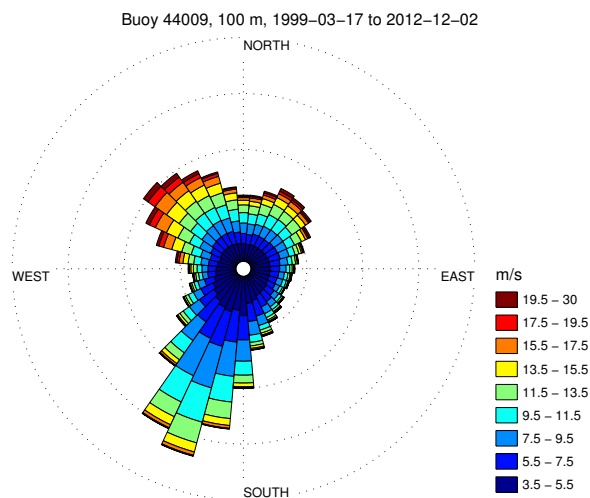


Figure 3.6: Wind rose for Buoy 44009, a NOAA buoy located off of the coast of Delaware. Note that the directional and speed bins correspond to intervals to be used in the WRF idealized windfarm modeling.

corresponding to the 36 directional bins, and power productivity is calculated based on a weighted sum of the wind distribution for the location.

3.3.1 Basic Geometric Arrays

This experiment design allows for preliminary analysis of the far field wake impacts at all wind speeds with a minimal amount of computing time. By doing this, it is possible to estimate the annual output for a hypothetical wind farm in this location using a variety of wind farm designs. Furthermore, seasonal variations can be assessed; for instance, while the winds are stronger in the winter months, it may be more desirable to have a wind farm layout which optimizes power output during the summer months, in order to correspond with the summer peak in power consumption. [Archer and Jacobson \(2013\)](#) describe that seasonal differences can be significant, particularly between the summer and winter months.

WRF is employed to simulate the same 5 wind farm layouts (SQR, TLR, LGR,

EQT, and DMD) used in the previous analysis, but with a larger domain to capture more of the downwind wake of the farms. Figure 3.7 shows some results from the triangular array (EQT) from 6 different wind directions. Since the triangle is an equilateral type, these 6 directions represent the entire compass rose. The model was run for all 36 10° wind direction bins, but due to the symmetry of the farms, these 6 directions are identical to the results in their corresponding bin elsewhere around the farm. The most important finding from these results is that the farm performs best when the point of the triangle is pointing directly into the wind direction, and the greatest wake effect is seen when blunt edge of the farm is facing the wind (compare Figure 3.7a and b).

3.3.2 Customized Array

Since the idealized farms were smaller than what is typical installed offshore, additional runs were performed using two different layouts for a wind farm with the specifics of the Bluewater Wind Delaware project (NRG Bluewater Wind, 2012): ninety 5 MW turbines for a total maximum output capacity of 450 MW. For these Bluewater Wind-type runs, a standard rectangular array (RECT) of 9×10 was used as a control; and a custom layout (CUST) was designed to capture more wind based on the dominant wind directions shown in the wind climatology at Buoy 44009 (Figure 3.6).

It can be seen that the impact of the CUST layout shares features with several of the idealized runs (see Figure 3.8). For example, the triangular pattern points facing into the peak wind directions of the wind rose: south-southwest, northeast, and northwest. In addition, this array layout emphasizes the south-southwest and northwest directions, since the majority of wind for this region comes predominantly from those directions. While there are strong winds out of the northeast on the wind rose, the frequency of these events is lower, and usually occur during winter storm events. Finally, the “courtyard” in the center allows minimization of the number of rows of turbines that are impacted by wakes occurring when the winds are from the predominant wind directions.

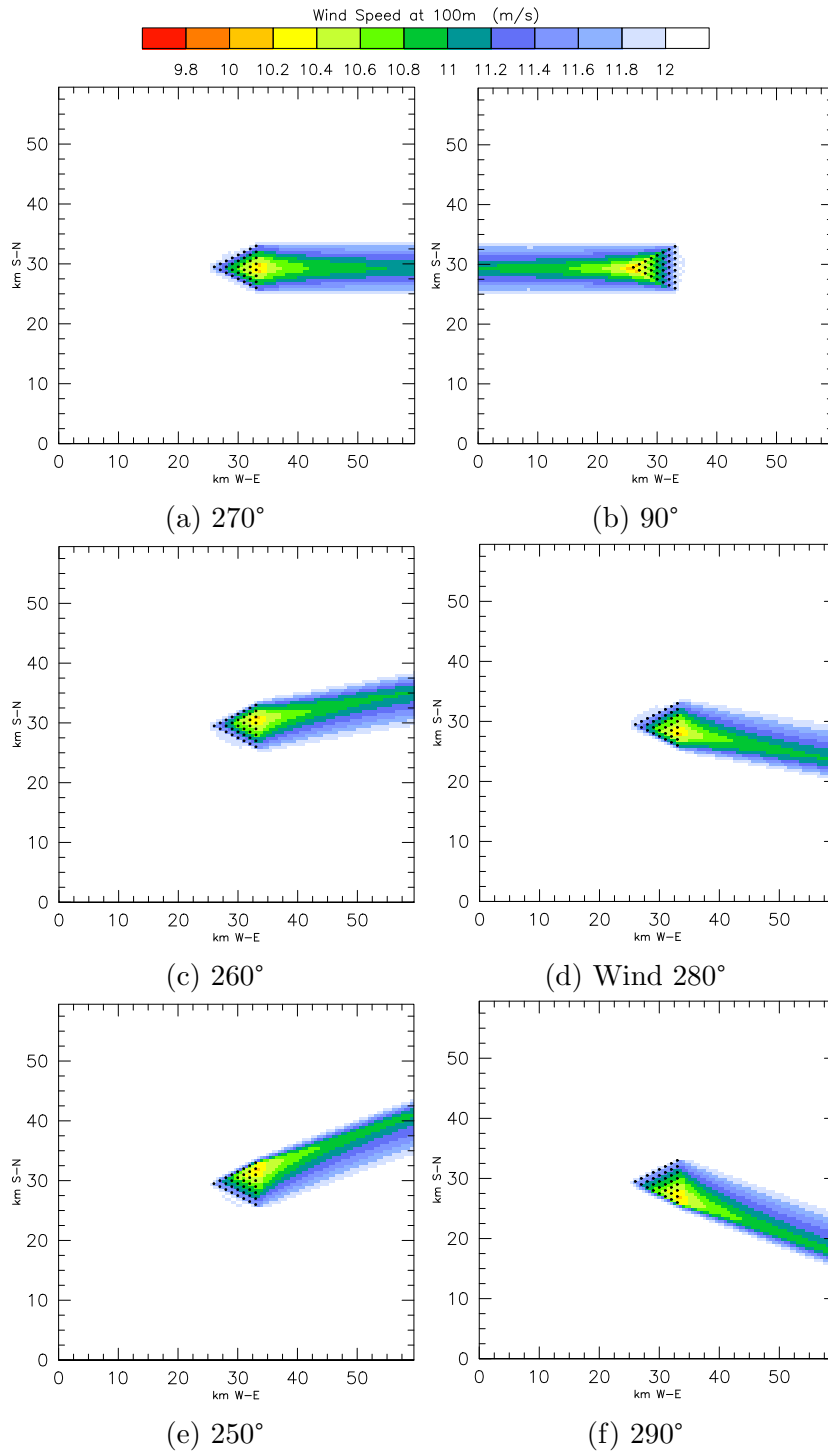


Figure 3.7: WRF model output of EQT with wind from 6 wind directions selected from the wind rose shown in Figure 3.6, depicting wind speed at 100 m height after 90 minutes of model integration.

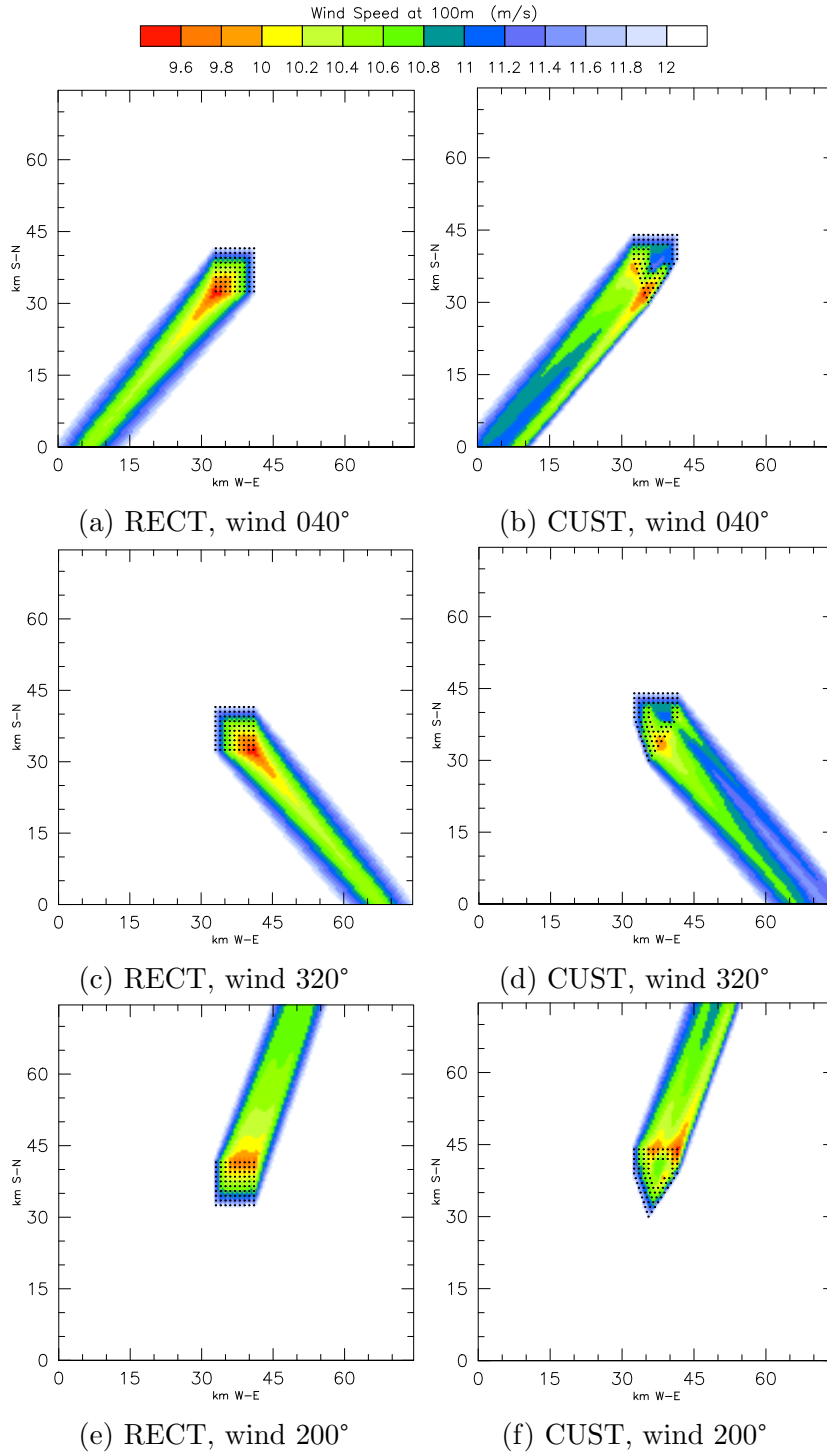


Figure 3.8: WRF model output of two possible Bluewater Wind-type projects, depicting wind speed at 100 m height after 90 minutes of model integration. The three wind directions shown were chosen to correspond to the peaks in the wind rose of Figure 3.6.

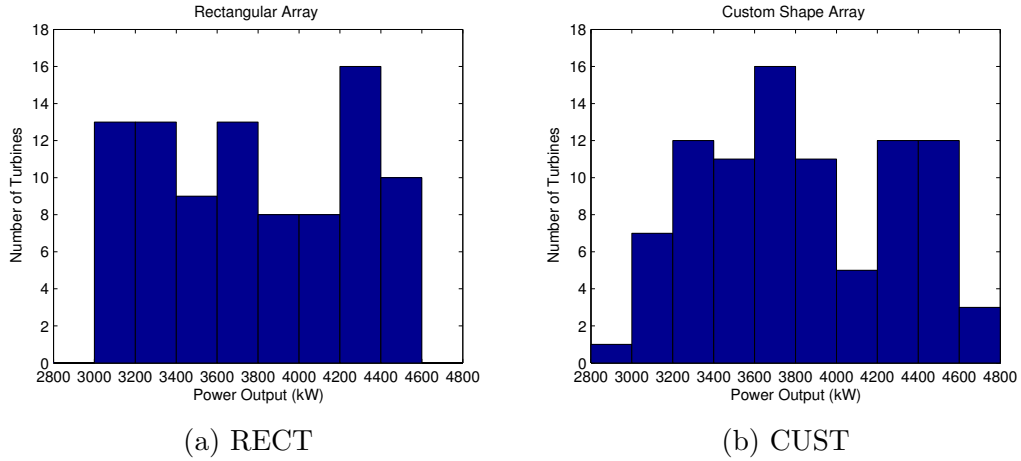


Figure 3.9: Histograms depicting the number of wind turbines producing a given amount of power for each of the two Bluewater Wind-type farms, with the wind blowing from 200°.

The same analysis on power output as used for the ideal layouts is then performed for the Bluewater Wind-style runs after 90 minutes of model integration with an initial wind speed of 13 m s^{-1} , calculating power output based on wind speeds at hub height. As can be seen in Table 3.2, the custom wind farm shape outperforms the standard rectangle in all three peak wind directions by between 1.2% and 4.0% in instantaneous power output. It’s important to note that while the custom shape actually has a larger percentage loss from best-to-worst in the south-southwest wind direction, it actually produces more overall power for this case. This larger percent loss is due to the fact that the best performing turbine is producing more power (4627 kW versus 4564 kW), and the worst producing turbine is producing less (2840 kW versus 3014 kW), and there are fewer turbines experiencing the most significant power loss. This is clearly seen in histograms (Figure 3.9) of the productivity of each individual wind turbine in the farm for southerly winds (200°). In fact, the custom shape array has 3 turbines producing more power than any of the turbines in the rectangular array. Furthermore, while the custom shaped array also has the worst producing turbine, it only has 7 turbines producing less than 3200 kW overall, while the rectangular array has 13 turbines producing at this level.

Table 3.2: Calculations of power output produced by two Bluewater Wind-type wind farms at the three predominant wind directions, using WRF predicted winds at 100 m hub height with initial wind speed of 13 m s^{-1} .

	Wind 40°		Wind 320°		Wind 200°	
	RECT	CUST	RECT	CUST	RECT	CUST
Total Array Instantaneous Power Output (MW)	344.5	352.7	344.5	358.4	340.6	344.8
Array Daily Power Output (MWh)	8268	8465	8268	8602	8176	8274
Best Turbine Instantaneous Power Output (kW)	4564	4627	4564	4564	4564	4627
Worst Turbine Instantaneous Power Output (kW)	2840	3102	2840	3102	3014	2840
Percent Loss from Best to Worst	37.77%	32.96%	37.77%	32.04%	33.96%	38.62%

Following this preliminary look at the comparison between the rectangular array and the custom array for Delaware’s offshore wind farm, a suite of model runs was performed to include every wind speed/directional bin from the wind climatology at Buoy 44009 (see the wind rose in Figure 3.6), amounting to 324 idealized runs per wind farm (36 directions and 9 wind speeds). The wind farm performance for each of these runs was calculated as before, and the annual contribution of wind power for that wind condition was calculated using:

$$P_{\text{bin}} = P_{\text{instant}} \cdot T \cdot p_{\text{wind}}, \quad (3.1)$$

where P_{bin} is the annual power contribution of this wind bin, in MWh; P_{instant} is the instantaneous power output of the farm under this wind bin’s wind conditions, in MW; T is 8760 h; and p_{wind} is the climatological probability of the wind conditions falling in to this bin. The total annual power production of the farm P_{annual} is then calculated

Table 3.3: Total power produced in the model runs for a Bluewater Wind-type wind farm under the climatological wind conditions at Buoy 44009. The control run contained no wind farm, so the power calculation is based on a wind farm where there were no array losses experienced whatsoever.

	RECT	CUST	CTRL
Annual Power (P_{annual} , MWh)	1 630 689	1 666 753	2 141 412
Difference from Rectangle (MWh)	–	36 064	–
Difference from Control (MWh)	510 723	474 659	–
Percent Loss due to Wakes	23.85%	22.17%	0%

by summing the power contribution of each of these wind bins:

$$P_{\text{annual}} = \sum P_{\text{bin}}. \quad (3.2)$$

In addition, a set of WRF control runs (CTRL) was also performed where the same domain and wind conditions were used with no wind farm located in the domain, in order to get a better idea of the impact of array losses. This allowed calculation of an idealized wind farm’s power production if it did not experience any array losses whatsoever.

Based on these sets of model runs and calculations, the custom shape CUST produced an additional 36 064 MWh over the rectangular array, an annual improvement of about 2.2%. A more complete set of calculations can be found in Table 3.3. If this were an actual wind farm under these conditions, the improved power production of the customized wind farm would have resulted in an additional \$3.8 million in annual revenue, based on the Bluewater Wind power purchasing agreement price of \$105.60/MWh (Firestone, 2008). Based on the U.S. Energy Information Administration’s 2014 average household electricity use of 10.9 MWh each year (U.S. Energy Information Administration, 2016a), this is enough electricity to power more than 3300 additional homes.

3.4 Summary and Conclusions

Studying wake effects with the goal of making wind farms more efficient is an important topic to make offshore wind more viable in the United States. The beginning of this chapter described an idealized WRF setup to evaluate the wake effects of 5 different wind farm array layouts of basic geometric shapes. This study found that WRF can replicate wake effects reasonably well, albeit not with the same level of detail seen in observations, or possible with higher resolution modeling, such as large-eddy simulations. Furthermore, it showed that both staggering of wind turbines from row to row, and having a triangular point of the array pointing into the predominant wind direction, can positively influence the power production of the wind farm. This answers two of the questions posed in Chapter 1: yes, the layout of a wind farm can influence power output, and factors such as staggering and increased front-row turbines from a triangular point in the predominant wind direction lead to improvements.

Using this knowledge, two different wind farm arrays were designed to evaluate their performance based on the climatology observed by Buoy 44009 near the Delaware Wind Energy Area. This part of the study found that the custom-designed shape outperformed a conventional rectangular array in all three of the predominant wind directions. If the results are weighted based on the probability distribution of the winds from the climatology, the custom shape would produce an additional 36 000 MWh of electricity in a climatologically normal year. The knowledge gained from this project leads into the remaining two studies of this dissertation: using WRF to study a specific meteorological phenomenon impacting the wind energy industry in Chapter 4; and the regional analysis of wind farm layouts in a set of real-world case study WRF model runs described in Chapter 5.

Chapter 4

EVALUATING MODEL PERFORMANCE FOR RAMP EVENTS

Wind ramp events, first discussed in Section 2.4, are a meteorological phenomenon where the wind speed increases or decreases at a location rapidly, which can have a significant impact on the operation of a wind farm (Marquis et al., 2011). While ramp events remain a highly relevant topic of ongoing research, the potential impact of ramp events on wind energy in Delaware has not been investigated. Driving research questions include: Under what meteorological conditions are ramps most likely to take place? How well is WRF able to predict these events? How might these ramp events influence the PJM grid operations discussed in Section 2.5.2?

This chapter will describe a modeling study of ramp events in the Delaware offshore region. First, a method of using observations to select suitable ramp case studies for modeling is described. WRF is then utilized to model the winds in the region during those case study ramp events in order to evaluate the forecasting performance under realistic operating conditions for a wind energy provider. Additionally, the “errors” in the forecasted wind relative to observations are applied to an analysis of the power demand to assess how these ramp events might interact with grid operations in PJM, along with a discussion on what factors are most likely to lead to a potentially unpredictable ramp event. Additional details on the impact of the model prediction error, calculated by Y. Shirazi, on the electrical grid are available in Veron et al. (2016).

4.1 Wind Ramp Identification using Observational Data

In order to evaluate model performance during ramp events, it is necessary to select suitable case study dates for which WRF can be run. Observations from NDBC buoy 44009 (see Section 2.2.1) during the period from March 2005 through December

2011 were examined for the occurrence of ramps. In order to estimate wind speeds and power production in a hypothetical wind farm from buoy observations made at 5 m, the log law (Equation 2.1) was used to estimate wind speeds at a hub height of 120 m, utilizing a roughness length of “blown sea” of 0.5 mm (Manwell et al., 2010). This 7-year period is relatively data-rich, but there are 13.6 months overall where the buoy was not operational. This period is also of interest due to high availability of forcing data from the National Centers for Environmental Prediction (NCEP), which will be discussed in Section 4.2.

For this project, a ramp time interval of $\Delta t \leq 1$ h was used, which captures all events detected using Equation 2.12 with $10 \text{ min} \leq \Delta t \leq 60 \text{ min}$. The lower threshold value is at the 10 min measurement frequency of the NOAA, which allows us to capture events that occur between measurements. P_T was selected to be 50% of the nameplate capacity of the wind turbine or farm examined, as used by Greaves et al. (2009). Since this work was conducted using the Vestas V164 8 MW wind turbine (Figure 4.1, Vestas Wind Systems A/S, 2011), this would be a 4 MW increase in power production in one hour or less. Applying these criteria to the 68.4 months of observations at buoy 44009 resulted in the identification of 357 ramp events, or 5.2 ramps per month on average.

Ramp events follow a seasonal cycle, as shown in Figure 4.2a. The most ramp events occur in April, due to the spring transition season, while the minimum takes place in August, corresponding to the low wind speeds in the summer months compared to an annual average (Hughes and Veron, 2015). Ramps are also highly time-dependent, shown in Figure 4.2b. Overall, ramps occur more frequently in both the evening and early morning. In terms of seasonal dependence, there is a summertime maximum in the early morning hours (05–09 GMT), while in winter the ramps occur more uniformly throughout the day. In spring, the maximum in ramp occurrence is in the early morning, accompanied by a similar peak in the evening, and in autumn, the ramps are more evenly distributed like in winter. Timing, both in terms of season and time of day, are of vital importance when evaluating electrical grid impacts.

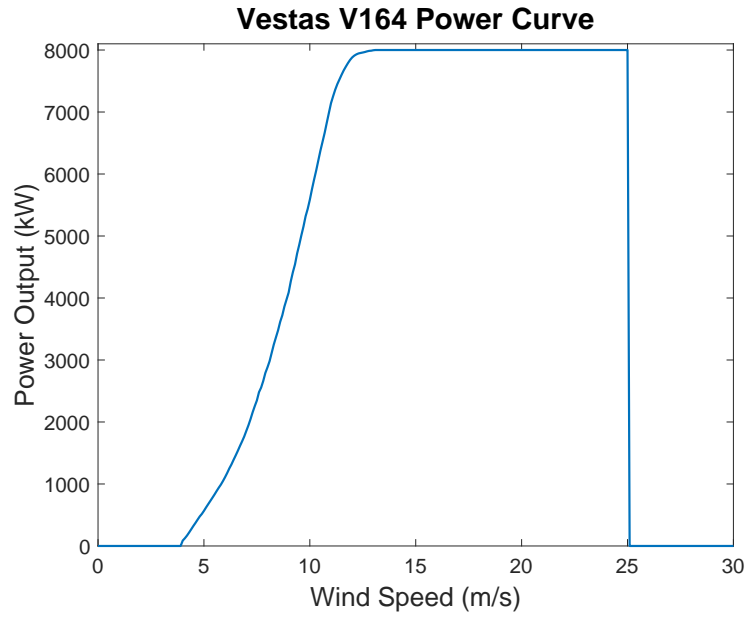


Figure 4.1: The published power curve for the Vestas V164 wind turbine.

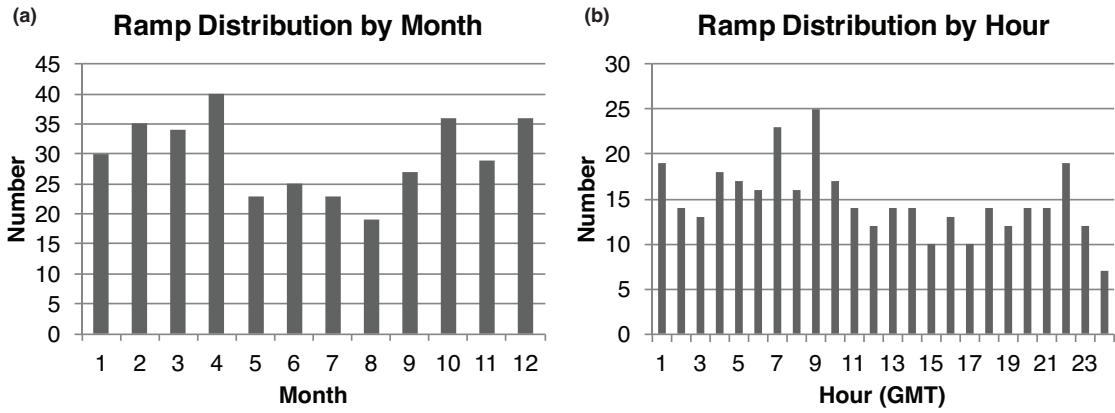


Figure 4.2: Distributions of the 357 ramp-up events detected by the ramp algorithm, shown (a) by month; and (b) by hour.

4.1.1 Selection of Case Studies

For this study, two different types of ramp events were considered when selecting suitable case studies for modeling: monthly average (analog) events; and extreme ramps which were noteworthy due to either their shape or magnitude. The selected dates are shown in Table 4.1. To find the analog events, all ramps identified in the observational analysis described above were grouped according to the calendar month. An algorithm was developed to time-shift the ramps so that they were aligned based on the mid-point of the ramp event. The ramps for each month were then averaged together to determine the intensity, duration, and shape of the monthly mean event. However, since this mean event is merely hypothetical, the algorithm used a least-squares fit to determine which of the ramp events making up that monthly mean most closely resembled the mean. The ramp with the best fit is selected as the analog for that month. Figure 4.3 shows the standard deviation of all the ramps in January, the numerical mean ramp and the selected historical analog for January.

In addition to the 12 historical analogs, 12 extreme ramp events were identified based on both the large ramp magnitude and potential for substantial grid impacts. The extreme ramps frequently included a rapid change from near calm winds to winds at or above the peak of the turbine power curve. In some instances, extreme ramps occurred in less than 30 minutes and the winds after the ramp were highly variable after the initial rapid increase.

In terms of goodness-of-fit, the selected historical analogs represent the monthly mean event fairly well. The average difference between the selected analogs and the means was 620 kW, with a maximum average difference of 1505 kW. The historical analog that least well matched to the mean occurs in October, with a maximum difference of 2469 kW between the mean ramp and the selected analog; however, the average difference between the analog and the mean for the entire October event was only 636 kW, which is comparable to the other months.

To further evaluate the effectiveness of these 12 historical analogs in representing a typical event, the synoptic types (Siegert et al., 2016) of each case study, and for all

Table 4.1: Case study dates of ramps selected for modeling along with their synoptic type. The analog cases are shown on the left side of the table, with the extreme cases on the right. Cases are shown in seasonal order from December through November.

Analog Cases		Extreme Cases	
Case Date	Synoptic Type	Case Date	Synoptic Type
30 December 2007	1013	7 December 2006	1034
12 January 2010	1013	13 December 2007	1011
2 February 2010	1013	19 December 2006	1033
27 March 2007	2010	29 December 2005	1035
18 April 2006	2034	17 January 2006	1035
10 May 2011	2010	19 January 2008	1013
13 June 2007	3035	2 February 2007	1035
7 July 2011	3031	23 February 2010	1014
14 August 2007	3031	4 March 2005	2032
30 September 2006	4032	17 June 2008	3036
19 October 2005	4038	29 June 2006	3032
3 November 2005	4032	10 August 2007	3002

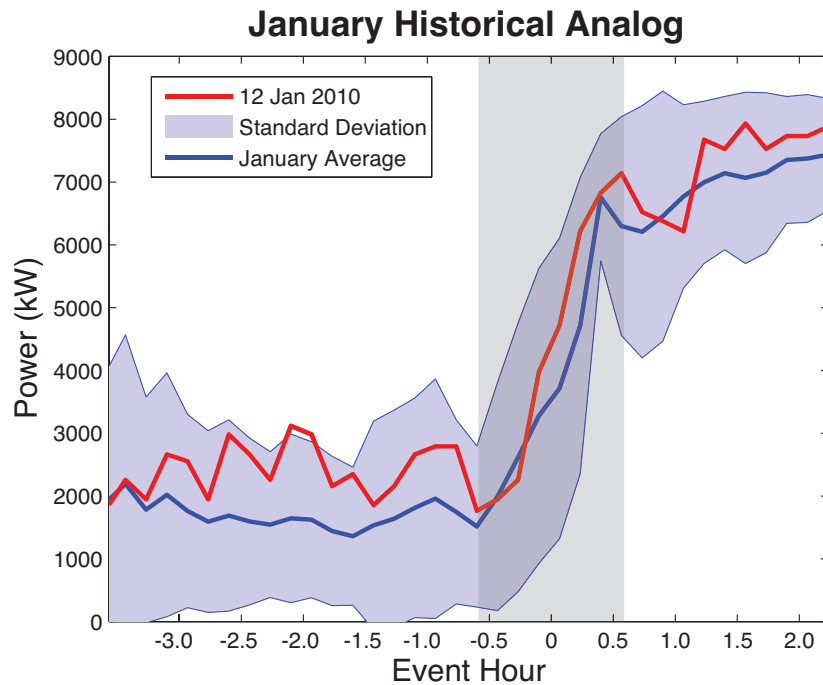


Figure 4.3: Monthly mean (blue line) and standard deviation (light blue shading) of ramps that occurred in January from 2006-2011. Selected historical analog shown in red. The ramp is highlighted by the gray box.

detected ramps, were evaluated. Figure 4.4 illustrates the frequency distribution by season for the 2005–2011 time period, both for all days and for days which feature a ramp. Not surprisingly, the distribution of synoptic types in which ramp events are found differ considerably from the overall synoptic type frequency distribution, since ramps are more likely to occur during certain meteorological conditions (Sevlian and Rajagopal, 2013). For offshore Delaware, ramps are more likely to occur in winter with a low pressure center located over the Midwest (type 1035) or Eastern Great Lakes (type 1034), while in summer they are common with a high pressure center in the Midwest (type 3034) or due to an approaching (type 3032) or passing (type 3033) frontal system. The transition seasons are a hybrid, with autumnal ramps being most prominent with a Mid-Atlantic high pressure center (type 4032) or a New England low pressure system (type 4009), and spring events occurring during an offshore cold front (type 2034) or weak zonal flow (type 2010).

As shown in Table 4.1, the selected historical analogs occur during synoptic types where ramps are more likely, further supporting their effectiveness as case studies and not outliers. Additionally, the 12 selected extreme events also occur during the synoptic conditions most favorable for ramps, illustrating that while they are classified as “extreme” events, they are by no means unlikely.

4.2 Modeling Ramp Events with WRF Forecasts

The WRF model simulated the 24 case studies and the output was used to assess the ability of the model to forecast ramp events. The modeling experiment was designed to simulate the type of modeling which may be done by a wind energy supplier operating a wind farm, which includes WRF being forced by datasets available to forecasting models and run on the timeframe which is set by both the release of the forcing data and the timing when wind farms operators are going to be bidding for energy. The model was forced with two different model forcing datasets distributed by the National Centers for Environmental Prediction (NCEP) at NOAA: the Global Forecast System (GFS, Kanamitsu, 1989; Kanamitsu et al., 1991) product, and the North American

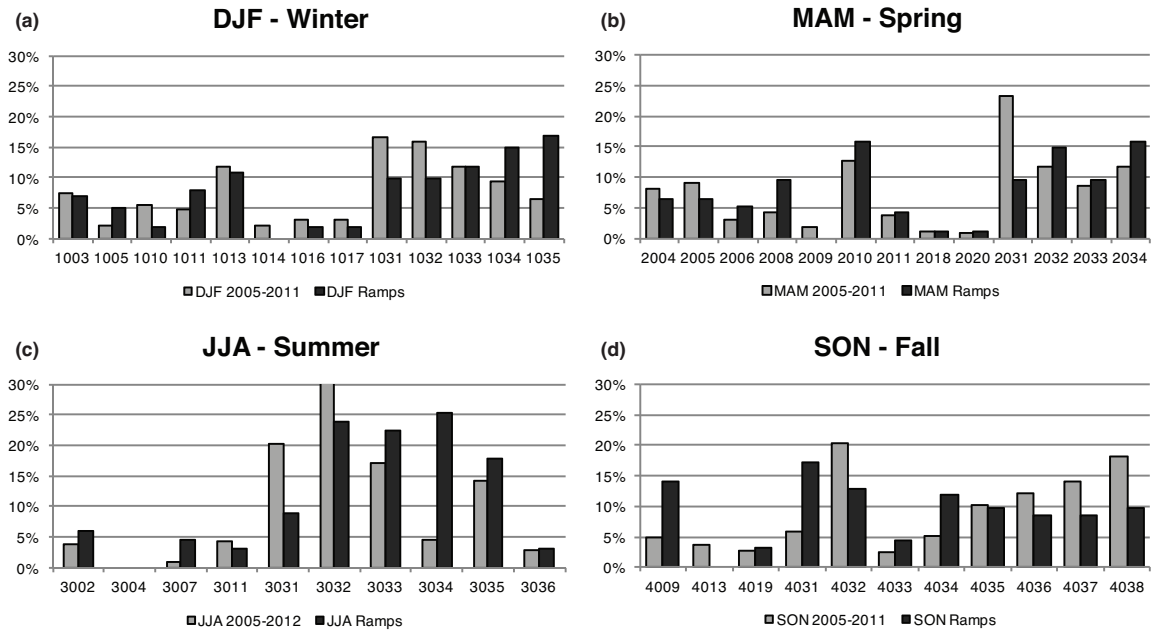


Figure 4.4: Synoptic type by number from [Siegert et al. \(2016\)](#) for (a) winter, (b) spring, (c) summer, and (d) fall for 2005-2011. The lighter bars depict the number of days per synoptic type for the entire study period, while the darker bars show the synoptic type for the days with ramps detected during the study period.

Mesoscale (NAM, [Black, 1994](#)) product. Both sets of model output are publicly available through NOAA’s National Operational Model Archive and Distribution System hosted by the National Centers for Environmental Information (NCEI, formerly the National Climatic Data Center, NCDC) (NOMADS, [Rutledge et al., 2006](#))¹, and are easily processed for WRF input by the WPS software.

The GFS model is a global model with output resolutions at both 1.0° and 0.5° resolutions, while the NAM only covers the North American continent and surrounding ocean areas at a 12 km resolution. Output for both models is available in 6-hour increments; the GFS 0.5° data are only available after July 2006. As such, each case study was modeled using both NAM and GFS 1.0° (hereafter GFS3) forcing data; cases which occur after July 2006 also include a third model run using GFS 0.5° (hereafter GFS4) forcing. All of the model runs were set up as 48 hour runs, including 12 hours of spin-up starting at 12Z the day before the case study date. The 12Z start time was selected due to power bidding requirements in the PJM region for “day-ahead” power supply bidding. GFS and NAM output is generally available in this region by mid-morning, allowing time for a WRF model forecast and analysis by an energy forecaster before power bids are due at 12 PM local to PJM for the following day.

The WRF model domain ([Figure 4.5](#)) was oriented to include a grid point at the location of buoy 44009, which allows for direct comparison between model results and observations without interpolation. Despite the fact that the Delaware WEA is located slightly north of the buoy, there are no *in situ* meteorological or oceanographic observations at the WEA. While wind in the WEA would likely vary somewhat from the winds observed and modeled at buoy 44009, we anticipate that model performance at the buoy and at the WEA will be similar. The domains for this model experiment consist of 3 nested grids at 36 km, 12 km and 4 km. Since the NAM model output is already provided at 12 km resolution, the outermost 36 km domain is omitted from the NAM-forced runs. The model is configured for two-way nesting, allowing the

¹ <http://nomads.ncdc.noaa.gov/data.php>

inner nests to feed information back into their parents. The physics parameterizations selected for these WRF runs are options that can be typically used for operational WRF runs (Table 4.2). The Mellor-Yamada-Janjić planetary boundary layer scheme, in association with the Eta similarity theory surface layer scheme, are selected to handle the boundary layer physics (Janjić, 1994). Cumulus convection was parameterized for the 36 and 12 km nests using the Betts-Miller-Janjić Eta operational scheme (Janjić, 1994), with the parameterization turned off for the 4 km nest, due to WRF’s ability to explicitly model convection at finer grid scales (Wang and Seaman, 1997; Gilliland and Rowe, 2007). Furthermore, Thompson microphysics (Thompson et al., 2008) scheme was used since recent research has indicated that the Thompson scheme performs well for forecasting in the wind energy industry (Davis et al., 2013), with some seasonal and regional dependencies (Cheng et al., 2013).

While WRF calculates wind at all 38 vertical levels throughout the run, analysis is conducted using the 10-m winds calculated by the model and extrapolated to hub height using the log law (Equation 2.1) to allow for similar treatment of modeled and observed winds. Observations at buoy 44009 are only available at 5 m; there are no tower observations in the offshore Delaware region. As such, extrapolated wind speeds at 120 m height in both observations and model output are used to calculate power using the turbine’s power curve. Generally, the 10-m modeled wind speeds that are extrapolated to hub height are about 1 m s^{-1} higher at 120 m than the wind speeds calculated at that height in the model; this bias is not consistent, and is often less during ramp events, occasionally becoming a negative bias. Model results forced with the GFS output generally show better agreement between extrapolated and explicitly modeled wind speeds at 120 m.

4.3 Meteorological Evaluation of Model Performance

The winds forecast by WRF for the ramp case studies are evaluated using the observations from Buoy 44009. The ramp timing and magnitude, along with wind speeds before and after the ramp, and the acceleration during the ramp are compared

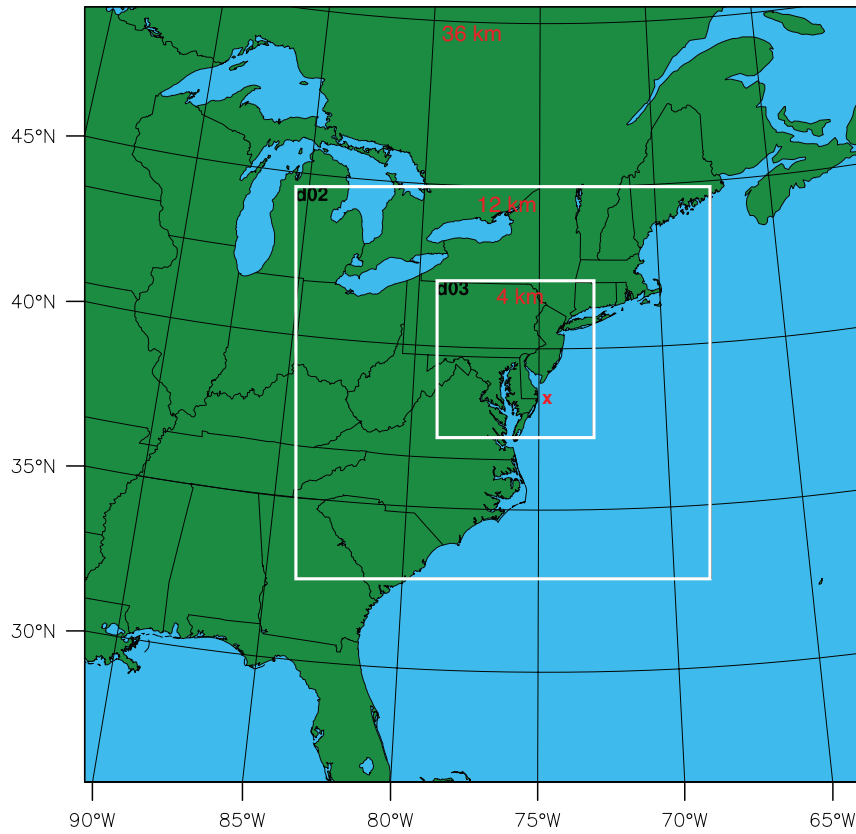


Figure 4.5: WRF model domains for the ramp case studies, with the location of buoy 44009 indicated by the red X, and the domain grid sizes as indicated in red. Note that the GFS3/GFS4 model runs include all three domains, while the NAM model runs only include the two inner domains (d02 and d03 on this figure).

Table 4.2: Parameterizations selected for the model runs conducted using WRF for the ramp prediction study.

Option	Setting	Reference
Planetary boundary layer (PBL) scheme	Mellor-Yamada-Janjić (MYJ)	Janjić (1994)
Surface layer scheme	Eta similarity theory	
Land surface scheme	Noah land surface model	Mlawer et al. (1997)
Microphysics scheme	Thompson double-moment 5-class graupel	Thompson et al. (2008)
Cumulus parameterization	Betts-Miller-Janjić Eta operational for 36 km and 12 km nests, none for 4 km nest	Janjić (1994)
Longwave radiation scheme	Rapid Radiative Transfer Model (RRTM)	Chen and Dudhia (2001)
Shortwave radiation scheme	Dudhia	Dudhia (1989)

among the simulations and with the observed winds. The performance of WRF varies widely depending on the synoptic weather conditions of each case, and the selection of forcing data, as shown in Figure 4.6 for the analog cases, and Figure 4.7 for the extreme cases.

In certain cases, such as 19 December 2006 (Figure 4.7c) or the GFS runs for 2 February 2007 (Figure 4.7g), WRF predicts the ramp timing and magnitude well, while in others, WRF simulates the ramp earlier or later than observed, like on 14 August 2007 (Figure 4.6i) or the GFS runs on 13 June 2007 (Figure 4.7g). In yet other cases, such as 23 February 2010 (Figure 4.7h) or the NAM-forced run for 13 June 2007 (Figure 4.7g), WRF does not produce a ramp in the wind speeds even though one was detected in the observations. Finally, the model may produce a ramp, but not of the correct shape. Ramp shape is the overall appearance (e.g. wind speed before and after) and slope of the ramp event on a time-series plot, and is typically categorized by a ramp that occurs more or less rapidly when modeled than it does in observations, such as 7 December 2006 in Figure 4.7a. Ramp misprediction can be defined by either an error in the timing of an event, or an error in the shape or magnitude of the event; or a combination of the two. This study works with two metrics to assess the error in the wind prediction, and then uses these to evaluate the impacts that misprediction may have on the grid.

4.3.1 Forecasting Error Metrics

The first metric developed in this study to evaluate the error in the forecast winds is a simple calculation of the difference between the model predicted power and the estimated power calculated using observed winds. For this work, the error is the predicted power subtracted from the power calculated using observations, which results in positive error when the winds are underpredicted, indicating a surplus of electricity produced from the wind that would need to be stored, dumped, or otherwise accounted for. Similarly, a negative error indicates an overprediction of wind, resulting in a production shortfall necessitating another source of electricity to make up for

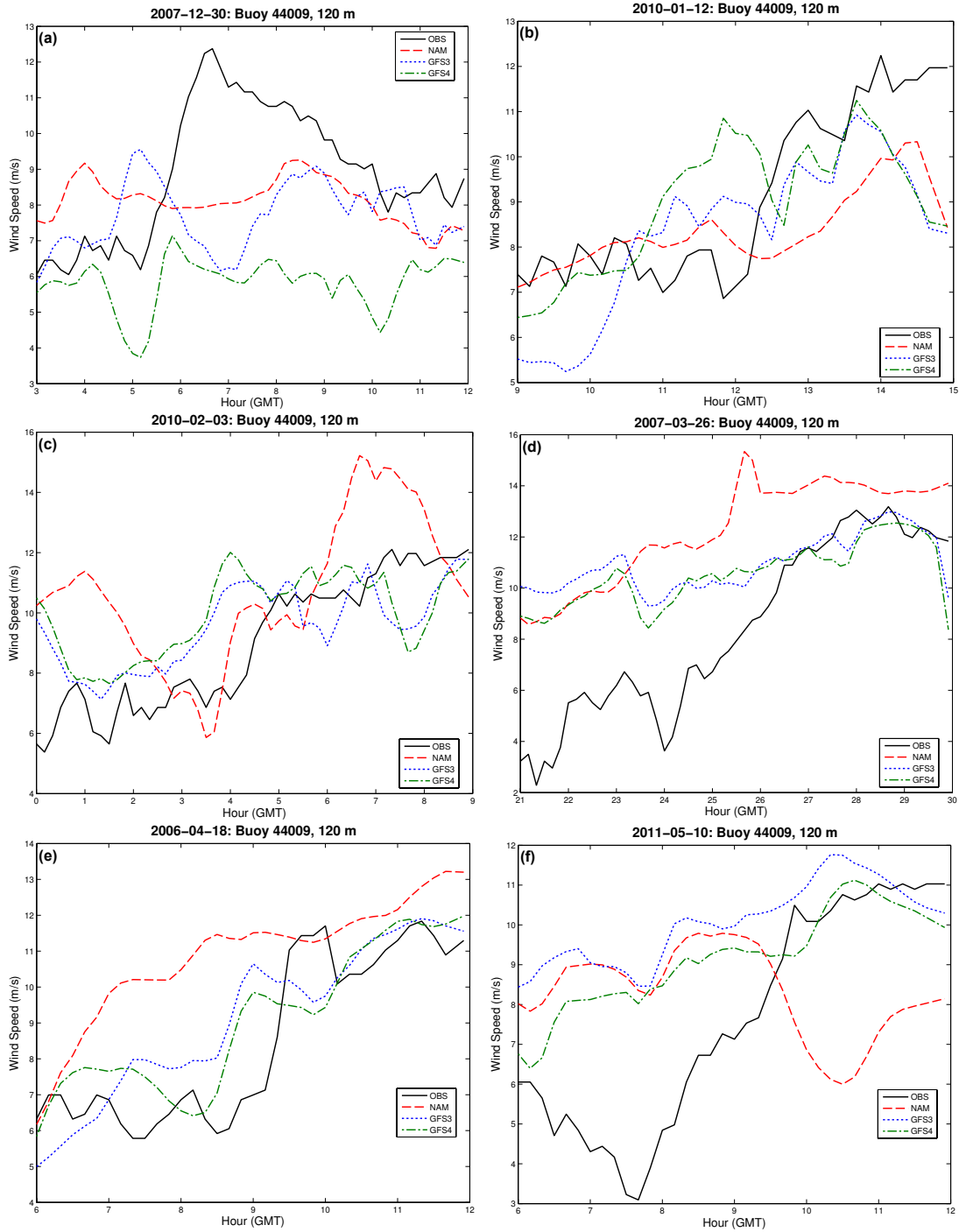


Figure 4.6: WRF modeled wind speeds using all three forcing datasets (red, blue, and green dashed lines) at Buoy 44009 extrapolated to 120 m hub height, compared to observations (black solid line) for the analog cases. (a) 30 December 2007; (b) 12 January 2010; (c) 2 February 2010; (d) 27 March 2007; (e) 18 April 2006; (f) 10 May 2011.

(continued on next page)

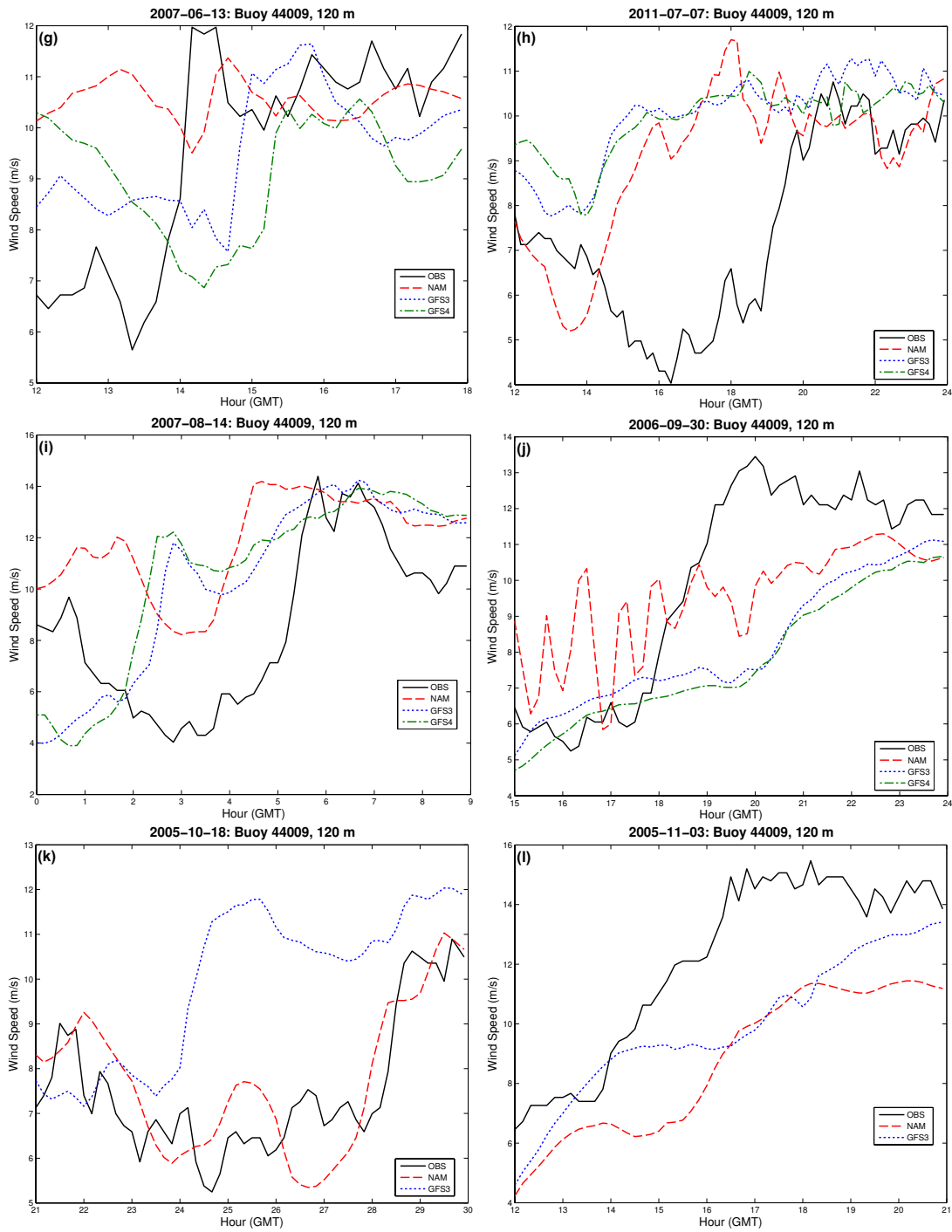


Figure 4.6: continued. (g) 13 June 2007; (h) 7 July 2011; (i) 14 August 2007; (j) 30 September 2006; (k) 19 October 2005; (l) 3 November 2005.

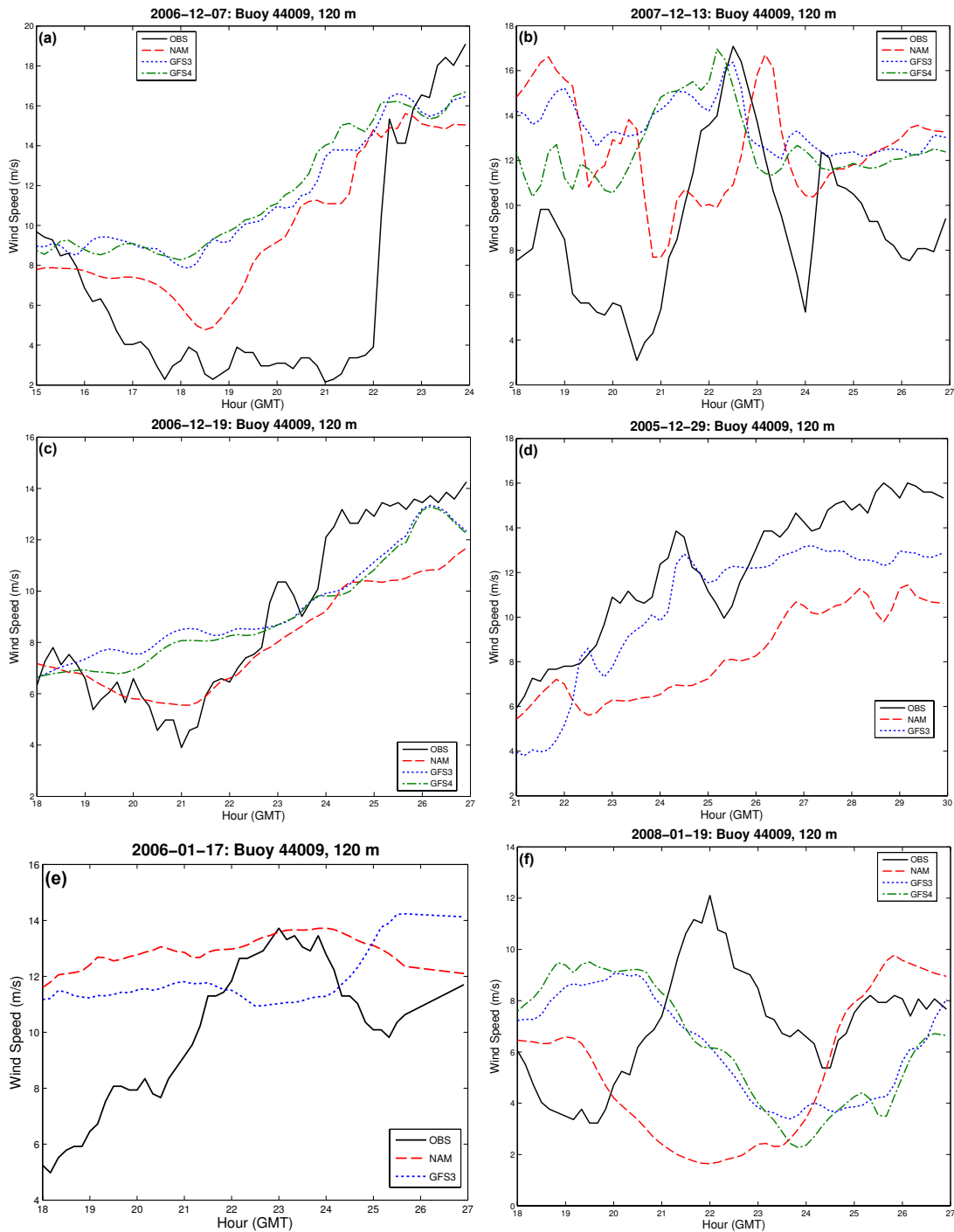


Figure 4.7: WRF modeled wind speeds using all three forcing datasets (red, blue, and green dashed lines) at Buoy 44009 extrapolated to 120 m hub height, compared to observations (black solid line) for the extreme cases. (a) 7 December 2006; (b) 13 December 2007; (c) 19 December 2006; (d) 29 December 2005; (e) 17 January 2006; (f) 19 January 2008.

(continued on next page)

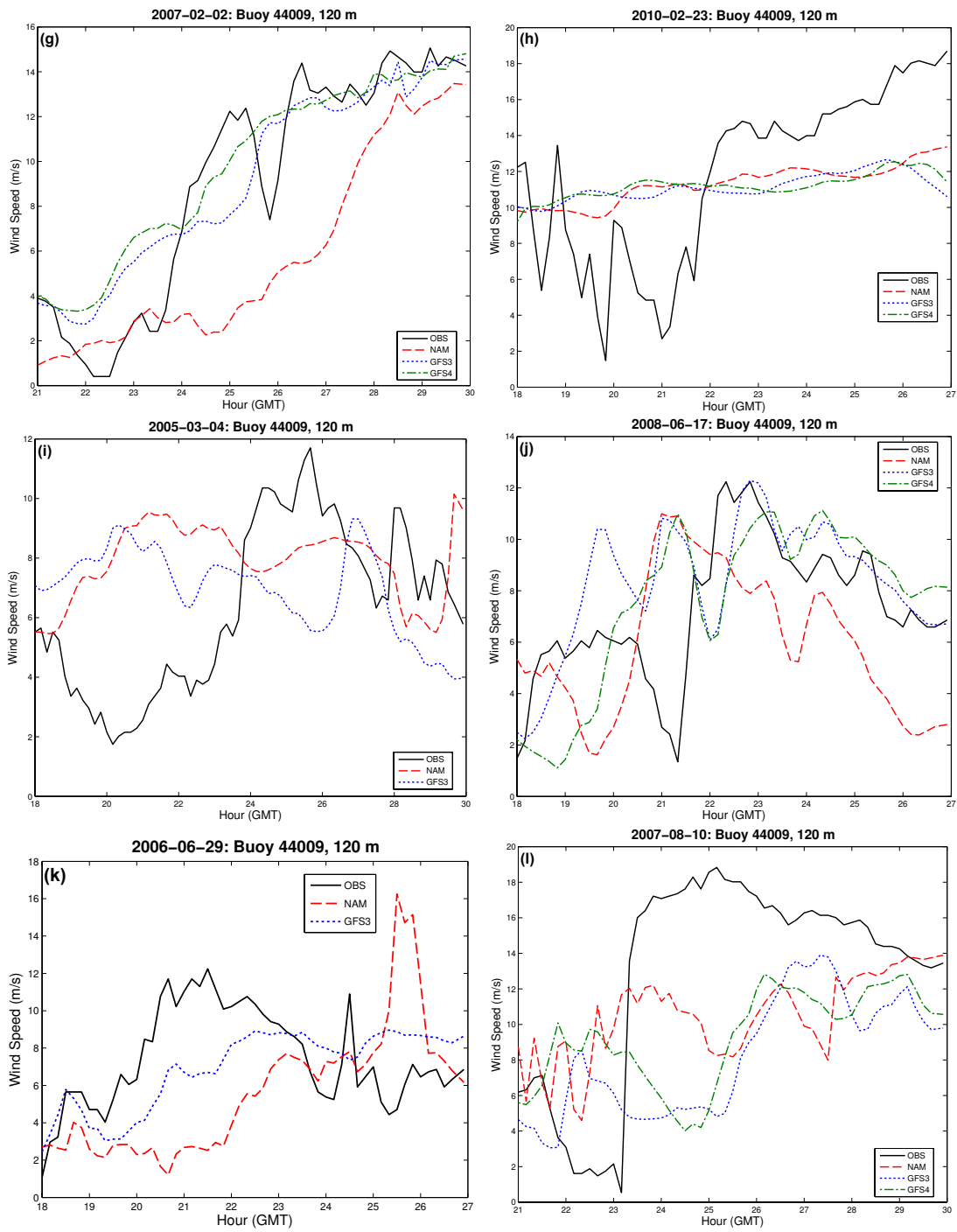


Figure 4.7: continued. (g) 2 February 2007; (h) 23 February 2010; (i) 4 March 2005; (j) 17 June 2008; (k) 29 June 2006; (l) 10 August 2007.

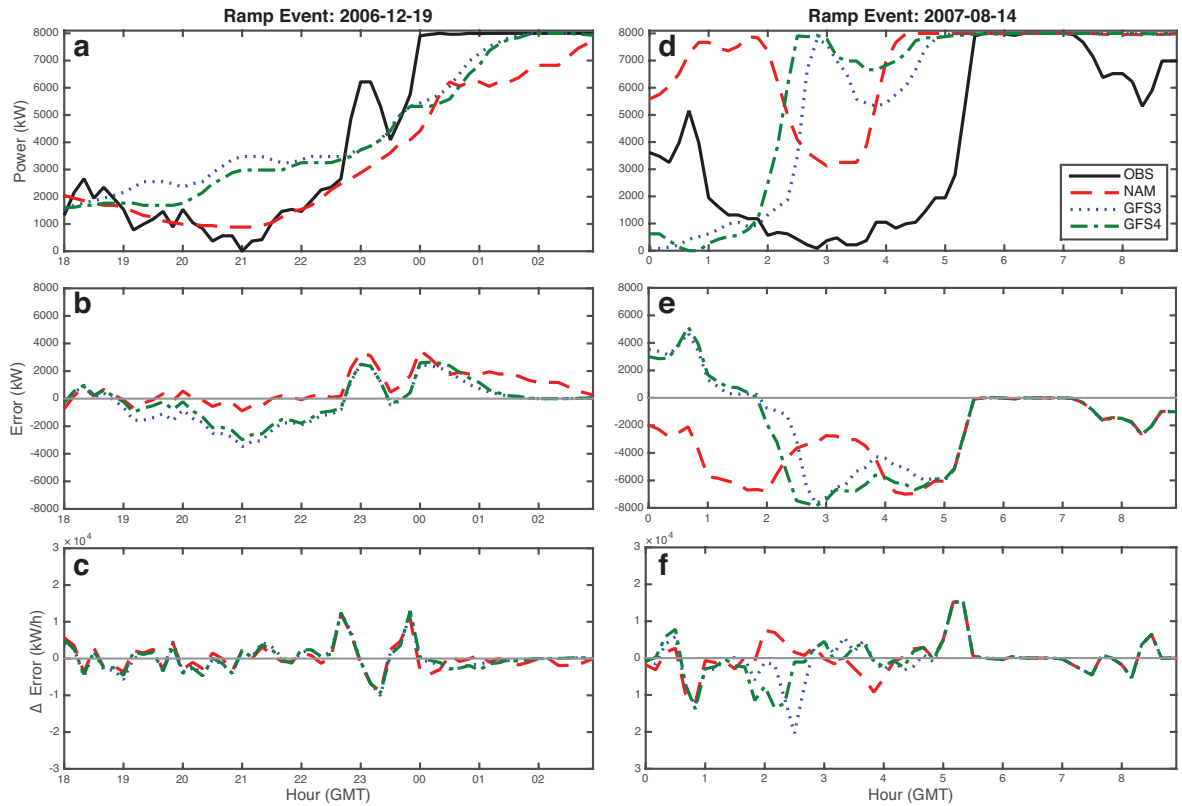


Figure 4.8: Two of the selected case studies showing the ramps as observed and modeled by WRF. (a–c) shows the ramp on 19 December 2006. (a) shows the power output based on observations and the model output, (b) shows the error defined as observations minus models, while (c) shows the rate of change of error. (d–f) shows the ramp on 14 August 2007, with axes as in (a–c).

the unexpected shortfall in wind-generated electricity (see Figure 4.8b/e). It is important to note the sign of this error, as each type of error would necessitate a different grid impact, and corresponding operator response. It is also counterintuitive to most meteorologists, who typically think in terms of observations subtracted from modeled results, indicating whether the model is either overpredicting (positive error) or underpredicting (negative error) the result. In this case, the amount of excess/needed power is inversely related to the model under/over prediction of the wind, necessitating the sign on the error opted for here.

The second metric of model forecasting error developed in this study is the first derivative of the previously calculated error, or the rate of change of error (see

Figure 4.8c/f). This metric aids in identifying when and where the prediction error changes rapidly and, in particular, indicates times when an overprediction may suddenly shift to an underprediction (such as a prediction of higher wind speeds before a ramp accompanied by the actual ramp taking place earlier than predicted). A very large rate of change of error may indicate rapid changes in the available wind, that may require a rapid adjustment from the grid.

Combined, these two metrics give an overall picture of how the model is performing, and how that performance may influence grid operations. An example is shown with two case studies in Figure 4.8. For the ramp event on 19 December 2006, the error between predicted and observed is less variable and extreme compared to more significant forecasting errors like 14 August 2007 (Figure 4.8b/d). Therefore, the model is seen as doing an adequate job of predicting the ramp overall, although the model predicts the ramp to take place more gradually than observed. However, the slight drop-off in winds (and therefore power) that takes place in the middle of the ramp-up between 2230Z and 0000Z, is highlighted in the rate of change in error shown in Figure 4.8c. During this time frame, the winds suddenly increase more than anticipated in the models, resulting in both a positive error (surplus wind power), and positive rate of change in error. Then, the winds drop off briefly, resulting in a near-zero error, but a sudden negative change in the error with time. Finally, the wind continues to ramp up, giving a positive error showing that the discrepancy between the model and observed winds is growing. This case illustrates a situation where a wind operator may be forced to curtail the wind production at 2230Z, only to have to stop curtailing the wind at 2330Z, and then resume curtailing production at 0000Z, if the operator had bid for the level of power predicted by WRF.

The importance of looking at the rate of change of error is clearly indicated in the case of 14 August 2007, shown in Figure 4.8d–f. In this case, the models predict the ramp to take place earlier than it actually occurs (Figure 4.8d), particularly the WRF runs forced using GFS data. In the WRF runs forced with the NAM product, WRF predicts a large and temporary drop in power on an otherwise windy day instead

of predicting a true ramp. Due to the fact that error magnitude leading up to the ramp is close to 8000 kW, the maximum error possible since it represents the difference between a turbine producing no power and full power, this results in a large amount of error prior to the actual occurrence of the ramp in observations at just after 0500Z, seen in Figure 4.8e. However, in between the GFS-forced model prediction of the ramp occurring at about 0230Z and the observed ramp at 0500Z, there is very little rate of change of error (see Figure 4.8f). This indicates that once a grid operator compensates for the lack of wind when expected at 0230Z, they need take no further action until the ramp actually takes place 2.5 hours later.

Ultimately, the challenge lies in being able to provide guidance to a grid operator regarding the reliability of a ramp forecast. Future work in this area could develop a reliability metric, based on the model's established performance under similar conditions, that could give the operator useful information that one predicted ramp event should occur with high confidence, while another has a more limited chance of occurring as predicted.

4.3.2 Grid Impacts and Assessing Forecast Probabilities

Ramp events like the ones modeled here can have a significant impact on grid operations. As one example, on 7 December 2006, an extreme event, the power output of the farm located at 44009 would have increased from near zero power to full power in just 6 minutes time. Given a proposed wind farm size of 100 8-MW turbines, this would be a rate of change of 800 MW over 6 minutes, or 8000 MW/h, the equivalent of spinning up a large thermal power plant in that same time frame. This particular event was verified using data from other nearby stations, in order to insure it wasn't merely an observational error.

As seen in Figure 4.2, the 357 ramps detected using the specified criteria during this time period are distributed throughout the day and the year. Ramps are more prevalent in the late evening/early morning hours; this is particularly true during December, February, April, May, and August. This time of day is typically characterized

by reduced electricity load demand, as seen in Figure 4.9a. Due to the reduced demand, a spike in wind power generation resulting from a mispredicted ramp event could have grid-related consequences, such as a necessary reduction in baseload power generation to accommodate the additional wind, exporting electricity to another grid system, or curtailing/storing the wind power. A similar situation is common in March and October, when ramp events typically take place in the evening, during periods of diminishing load, as seen in Figure 4.9b. A mispredicted ramp during this time exacerbates the grid impacts during a period of low load demand: an increase in wind power production resulting in surplus power to the grid which is already ramping down power production in order to meet decreased load demand.

In contrast, the months of January, June, September, and November often include ramps that occur in early to mid-day, which are times characterized by increasing load demand, and the peak demand for the day (Figure 4.9). Under these conditions, a wind ramp could allow other generation plans that normally spin up to meet peak load (i.e. natural gas generators) to reduce their power generation or their own ramp rate. However, this introduces an issue when a ramp is predicted and accounted for, but then does not occur; those reserve generators will need to be ramped up unexpectedly in order to meet the load demand. A method for assessing the potential impacts of a wind ramp on the electrical grid was developed by Y. Shirazi, and is discussed in detail in Veron et al. (2016).

Wilczak et al. (2015) noted that model forecast improvements could be made by forcing the model using GFS and observational data assimilation, particularly when this data assimilation can lead to small wind power underprediction being corrected. In the present ramp study, there was no clearly superior model forcing data for WRF. NAM forcing tended to produce better timed ramp events, but they were typically more gradual than the observed ramps. In addition to the improvement in timing with NAM, the post-ramp wind speeds were often better predicted by the GFS-forced runs. This was particularly true for synoptic types 1035, 2010, and 3031, all different types in different seasons. Interestingly, the GFS4 forced model runs resulted in a greater

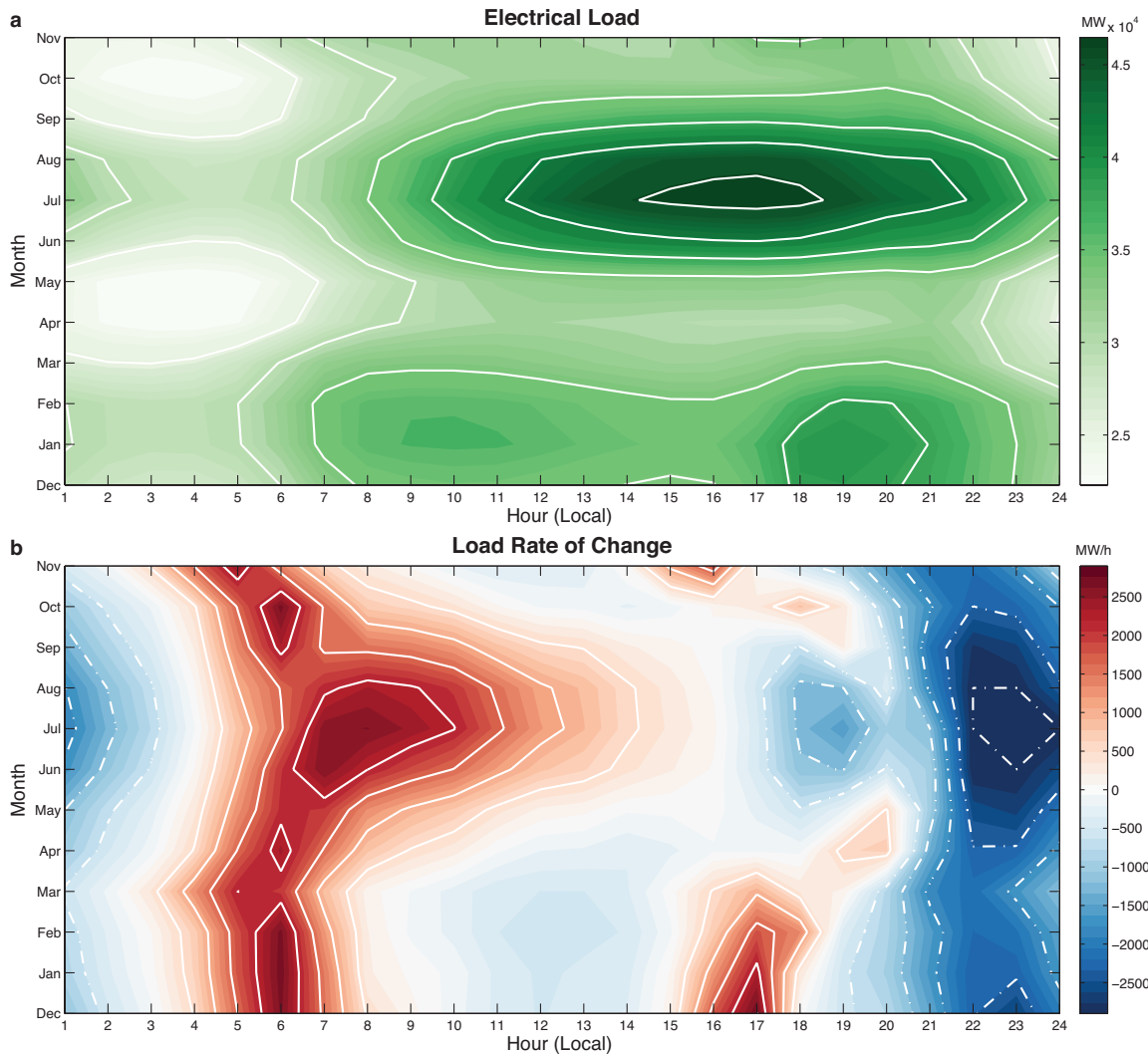


Figure 4.9: Illustration of the electricity demand (load) in PJM Interconnection from 2005-2011. (a) is the same as Figure 2.6 and shows the average electrical load as a function of hour of the day, plotted versus the month of the year. The darker colors indicate a greater electrical load. (b) shows the rate of change of this average load, with red colors (solid contours) indicating an increasing load demand, and blue colors (dashed contours) indicating decreasing load demand.

amount of prediction error during times of increased load demand or rapid load demand changes, suggesting that improved model forcing data resolution does not necessarily result in better model results.

The timing of a ramp event was seen to be the most significant factor in not causing potential issues with grid stability, particularly if the ramp event occurred during a period of increasing load demand. Ramp events were more likely to be predicted to occur earlier than observed, with half of the analog events and one quarter of the extreme events being predicted in this way. Conversely, only one fifth of both types were predicted to occur later than observed. In 9 of the extreme cases, and 5 of the analog cases, WRF predicted the wind speeds before the ramp event to be higher than observed, resulting in a lower overall ramp magnitude. WRF also entirely missed 2 extreme ramps and 1 analog event, while also showing an overall wind speed prior to the event to be higher than observed. It must be noted that in reality, the change in energy produced by a wind farm experiencing a ramp event will likely be smoother than that predicted in this study, as the spatial impacts of having wind turbines spread out over a large area of hundreds to thousands of km² will result in a more gradual overall power production change.

The diversity of model results illustrate the importance of continued work to improve the wind's predictability in mesoscale models. No clear model bias or trend emerges significantly enough to justify a specific adjustment to model results in order to make them more reliable for wind energy forecasting. [Marquis et al. \(2011\)](#) found that despite the challenges, making improvements in forecasting skill is a more economical solution than increasing the necessary backup power to compensate for forecasting error. In the interim, care must be taken when model guidance indicates a ramp event, or the potential for a ramp event, particularly if the situation falls during times of peak load demand or rapid load demand change. Until the forecasting skill improves, wind energy forecasters should be conservative with their predictions during ramp-inducing weather in order to maintain grid reliability.

4.4 Summary and Conclusions

Wind ramp events are a meteorological phenomenon which can result in electricity grid issues due to their inherent high levels of variability and unpredictability. However, the grid impacts are also variable, depending on the type of forecasting error, and the electrical demand at the time. This study used WRF to model 12 historic analog ramp events, and 12 extreme ramp events, as determined by the ramp magnitude and shape. This modeling illustrated the complexity involved in accurate predictions of ramps, demonstrating errors in ramp timing, magnitude, and overall shape. The use of different forcing datasets had a variable impact on WRF's forecasting skill, and no one dataset was clearly superior.

Errors in the timing of ramp events were shown to be more impactful than errors in magnitude or shape. Additionally, it was found that forecasting errors made during periods of increasing load demand are particularly challenging for grid stability. Because of this, improvements in wind forecasting skill would be most helpful if made in the morning hours throughout the year, and evening hours particularly in the winter, as these are daily periods of increasing load demand. As wind power penetration continues to expand, so too must wind forecasting skill and the grid's ability to handle the inherent variability in the wind. Forecasters in the wind energy industry must use caution when predicting power production during periods when ramp events are likely, and could cause grid instability if the forecast is wrong.

With the usefulness of using WRF to study wind energy in the Delaware Wind Energy Area established, Chapter 5 will take this to the next level by including various wind farm arrays in the model domain, and running an assortment of case studies to evaluate the farm performance in different meteorological conditions.

Chapter 5

REGIONAL MODELING OF A DELAWARE OFFSHORE WIND FARM

Previous results from this dissertation have shown that there is a benefit to placing the turbines in a wind farm in a layout other than a traditional rectangular grid. However, these results focused on an idealized wind simulation that did not explore the sensitivity of those results to wind variability. This next chapter explores the impact that wind farm layout has on the overall power production for a wind farm located in the Delaware wind energy area. This experiment combines the knowledge and experience gained in the earlier work for a modeling study of wind farm layout and performance for the Delaware Wind Energy Area. First, the process of selecting case studies is described, followed by the setup of the WRF model for this part of the study. Finally, the results of this study are discussed.

5.1 Case Study Selection

An assessment of the wind resource for a given region can be done using observational or modeling data or a combination of both. There is value in having a large volume of model data with which to evaluate and extend the observed wind conditions when constructing a wind farm. Ideally, a wind developer would have a large amount of data at hub height and sub-kilometer spacing at their disposal. However, practicality of the modeling effort needs to be considered, due to finite time and computational resources. Several studies have explored how to employ limited temporal and spatial data in order to perform a reasonable wind assessment without the ideal modeling described above (i.e. [Lackner et al., 2010](#)). One method of developing a statistically representative dataset is through careful selection of case studies which can provide a

reasonable assessment of a wind farm’s likely productivity without needing an excessive amount of computational resources.

Synoptic typing, as described in Section 2.3 (Siegert et al., 2016), provides a unique and useful way to evaluate the variety of weather conditions experienced in a region, and can provide guidance on suitable case studies for modeling (Hughes and Veron, 2015). Work discussed earlier (see Section 4.1) indicated that the winter and summer seasons are the most interesting with regards to wind energy, when there is a large change in both electricity demand and available wind. While there is a high demand for power in both seasons (see Figure 4.9), there is much less wind in the summer. The intermediate seasons of spring and autumn often are a combination of summer and winter wind speeds and directions. As such, it is of interest to evaluate both simulated and observed wind by the synoptic types which occur during winter and summer before selecting case studies. Tables 5.1 and 5.2 show the number of days which correspond to the different synoptic types which occur during the winter and summer, both for the full data record used in Siegert et al. (2016) (1946–2012) and for the study period of 2005–2011 (gray bars, Figure 4.4a and c). With a handful of exceptions, the synoptic types which occur during the 2005–2011 study period are similar in frequency to the complete Siegert et al. (2016) study.

The frequency distribution of synoptic types provides an ideal method with which to guide the selection of case study dates for modeling. This frequency distribution tells us the likelihood of a particular synoptic situation taking place, and therefore, guides how much emphasis should be placed on each synoptic type. Naturally, due to the constraints of limited time and computational resources, it is necessary to select a limited number of case study dates which capture the daily variability of weather. The use of these synoptic types allows for a climatological representation of this variability. A target of 30 case study dates for each of the two seasons was chosen, capturing the variability of wind conditions that occur during most synoptic types. The number of selected case studies and their frequencies are shown in Table 5.3. These selections will allow for the cases to be statistically representative of the various synoptic and

Table 5.1: Frequency of winter synoptic types, both from the entire period that [Siegert et al. \(2016\)](#) used to develop the synoptic types, and for the selected period for this research, 2005–2011.

Type	All Events		2005–2011	
	Number	Percent	Number	Percent
1003	463	7.7	47	7.5
1005	178	2.9	13	2.1
1010	413	6.8	35	5.6
1011	341	5.6	30	4.8
1013	535	8.9	74	11.7
1014	169	2.8	13	2.1
1016	274	4.5	20	3.2
1017	118	2.0	19	3.0
1031	1085	17.9	105	16.6
1032	919	15.2	101	16.0
1033	747	12.4	74	11.7
1034	386	6.4	59	9.4
1035	419	6.9	41	6.5
Total	5247	100.0	631	100.0

Table 5.2: Frequency of summer synoptic types, both from the entire period that [Siegert et al. \(2016\)](#) used to develop the synoptic types, and for the selected period for this research, 2005–2011.

Type	All Events		2005–2011	
	Number	Percent	Number	Percent
3002	219	3.6	25	3.9
3004	23	0.4	0	0.0
3007	163	2.6	6	0.9
3011	432	7.0	27	4.2
3031	1402	22.7	130	20.2
3032	1565	25.4	208	32.3
3033	895	14.5	110	17.1
3034	290	4.70	29	4.5
3035	1051	17.1	91	14.1
3036	124	2.0	18	2.8
Total	6164	100.0	644	100.0

Table 5.3: Number of case studies selected by synoptic type.

Winter Cases (DJF)			Summer Cases (JJA)		
Type	Number	Percent	Type	Number	Percent
1003	2	6.3	3002	1	3.2
1005	1	3.1	3004	0	0.0
1010	2	6.3	3007	1	3.2
1011	1	3.1	3011	1	3.2
1013	4	12.5	3031	6	19.4
1014	1	3.1	3032	10	32.3
1016	1	3.1	3033	5	16.1
1017	1	3.1	3034	2	6.5
1031	5	15.6	3035	4	12.9
1032	5	15.6	3036	1	3.2
1033	4	12.5			
1034	3	9.4			
1035	2	6.3			
Total	32	100.0	Total	31	100.0

climatic variability present in the Delaware offshore region.

The case studies were chosen randomly by synoptic type in the following manner. First, the synoptic type data from March 2005 through December 2011 were sorted into chronological order into an array for each synoptic type. A random number generator was seeded using the numerical value for each synoptic type, in order to enable an easily traceable method to add additional cases if it were needed later. The random number generator provided an index value, which was used to select the date from the array which contained the dates for each synoptic type. This method was used to select the number of cases indicated in Table 5.3, along with one alternate for each case to provide for a back-up in case there were any issues with one of the selected case study dates. The selected case studies are listed in Table 5.4, while the selected alternates are in Table 5.5. It should be noted that there were no cases modeled of synoptic type 3004, this synoptic type did not occur during the study period. This type occurred only 0.37% of the time over 60 years.

Table 5.4: Selected case study dates for modeling of the Delaware Wind Energy Area.

Winter Cases (DJF)		Summer Cases (JJA)	
Date	Type	Date	Type
2008-12-27	1003	2006-06-07	3002
2009-02-26	1003	2010-07-02	3007
2009-01-24	1005	2006-07-01	3011
2006-12-22	1010	2005-06-01	3031
2007-12-10	1010	2005-06-07	3031
2009-01-10	1011	2005-07-29	3031
2005-12-17	1013	2010-07-16	3031
2007-12-08	1013	2010-08-09	3031
2009-02-14	1013	2011-06-08	3031
2011-01-14	1013	2005-06-11	3032
2007-12-06	1014	2005-06-28	3032
2010-01-14	1016	2007-06-29	3032
2007-02-14	1017	2007-06-30	3032
2005-12-06	1031	2007-08-25	3032
2007-02-10	1031	2008-06-14	3032
2007-12-17	1031	2008-06-27	3032
2008-02-14	1031	2008-07-13	3032
2010-02-12	1031	2010-06-01	3032
2007-01-04	1032	2011-07-24	3032
2007-01-05	1032	2006-06-20	3033
2007-12-23	1032	2006-08-08	3033
2008-12-10	1032	2008-08-03	3033
2009-01-04	1032	2009-08-06	3033
2008-02-16	1033	2010-08-17	3033
2008-12-05	1033	2007-07-01	3034
2009-02-19	1033	2007-07-02	3034
2009-02-19 ¹	1033	2006-08-17	3035
2008-02-19	1034	2007-06-13	3035
2010-02-26	1034	2007-07-26	3035
2011-01-02	1034	2008-07-15	3035
2005-12-01	1035	2006-06-11	3036
2009-12-09 ²	1035		

Table 5.5: Alternate case study dates for the regional modeling of the Delaware Wind Energy Area.

Winter Cases (DJF)		Summer Cases (JJA)	
Date	Type	Date	Type
2005-12-08	1003	2009-06-13	3002
2006-12-30	1005	2009-08-14	3011
2006-01-22	1010	2006-06-08	3031
2008-01-17	1011	2010-08-16	3032
2008-02-23	1013	2005-07-06	3033
2011-02-15	1014	2008-08-31	3034
2009-12-14	1016	2005-07-16	3035
2011-01-08	1017	2005-06-17	3036
2011-01-23	1031		
2011-01-01	1032		
2006-01-01	1033		
2006-12-23	1034		
2008-01-29	1035		

5.2 Model Setup

As previously mentioned in Section 2.6, some of WRF’s power lies in its design as a flexible mesoscale model, intended for regional meteorological studies, with a large suite of dynamical and physical parameterizations that allow for model configurations to be customized for a range of studies. While the work conducted in Chapter 3 demonstrates the efficiency and ability of WRF to simulate the impact of a variety of offshore wind farm designs on the wind field using an idealized domain, this experiment tests the model in regional forecasting configuration setup with real-world meteorological conditions. Ultimately, the results from this study will provide guidance towards improving wind resource assessments by combining mesoscale modeling with wind farm layout development.

For this study, WRF version 3.6.1 is used, with some significant changes were made to the input parameters for the [Fitch et al. \(2012\)](#) wind farm module since its

¹ Since this date was selected twice by the algorithm, the alternate was used (2006-01-01).

² This case experienced technical difficulties, and so the alternate case was used (2008-01-29).

original implementation, allowing for the user to easily specify the power and thrust characteristics for the wind turbines. Details on the model setup described in this section include specifics on the wind farms for insertion into WRF; the design of the model domains and the selection of vertical, horizontal, and temporal resolution; and finally details on the model physics, forcing data, and other namelist options.

5.2.1 The Wind Farms and Model Domain

The wind farm characteristics used in the model runs described in this chapter are similar to the those employed in the idealized Bluewater Wind study described in Section 3.3. Each wind farm consists of 90 REpower 5M 5 MW wind turbines, for a total wind farm capacity of 450 MW. It is important to note that for this study, rather than using the idealized 5 MW machines used in Chapter 3, the specifications of the actual REpower 5M are used (REpower Systems AG, 2011, 2010), which allows for inclusion of more wind turbine specifications.

In order for the wind farm parameterization to properly model the impact of the wind turbines on the atmospheric flow, WRF requires a variety of input data, included in two separate plain-text input files. The first is `windturbines.txt`, which includes the latitude and longitude of each wind turbine, along with an integer value that indicates what type of wind turbine is located at each latitude/longitude pair, thereby allowing multiple turbine designs to be included. The second data file is the input file `wind-turbine-*.tbl`, which contains the technical parameters for each of the wind turbine types specified in the first file (in this case, only one type, $* = 1$). This file contains the data necessary for the wind farm parameterization to calculate the impacts of the wind turbines, and includes the height of the hub (90 m), the power capacity of the turbine (5 MW), the rotor diameter (126 m), and the standing thrust coefficient. This file also contains a breakdown of both the wind turbine power curve and the thrust coefficient curve at various wind speeds, as detailed in REpower Systems AG (2010); the power curve is shown graphically in Figure 3.4.

Since this study aims to expand the results found in Chapter 3 through exploration of more realistic meteorological conditions, it will include modified versions of the 10×9 rectangle (RECT) and the custom shape (CUST) 90 turbine wind farms discussed in Section 3.3. As described in further detail below, a select number of case studies were also modeled with four other wind farm configurations: a rectangle rotated to align with the southeast edge of the custom shape (RADJ); along with the regular rectangle with staggering spacing every other east-west row in order to improve conditions for north-south wind flow (STNS) and every other north-south column for west-east wind flow (STWE). This rotated rectangle shape acts as a control to investigate the impact of changing the orientation of the wind farm, and the staggered rectangles act as a sensitivity test of the number of turbines in the “front” row. Finally, these select case studies were also modeled using the custom shape, but with the “courtyard” replaced with 15 additional wind turbines (FILL, 105 total turbines) in order to evaluate the impact of the presence of the gap in the custom shape on the wake. The layouts of all six wind farms can be seen in Figure 5.1.

Within each farm, the turbine rows and columns are spaced 10 rotor diameters apart in the x and y direction, or 1260 m, slightly further apart than the turbines in Section 3.3. As shown in Figure 5.2, these six farms are all positioned within the lease area for the Delaware Wind Energy Area, as specified by the Bureau of Ocean Energy Management (BOEM) of the United States Department of the Interior (Bureau of Ocean Energy Management, 2013, 2015). The location of the turbines in all of the farms are in the `windturbines.txt` files found in Appendix A.

The domain for these model runs included 4 nested domains centered over the Delaware Wind Energy Area (as shown in Figure 5.3). The innermost nest, d04, is 234 grid cells east-west and 210 grid cells north-south and has a horizontal resolution of 630 m, which is half of the distance between wind turbines, as described in Section 3.3. The horizontal resolution increases by a factor of 3 for each domain to the outermost parent, yielding horizontal resolutions of 1890 m for d03, 5670 m for d02, and 17.01 km for d01. These nested domains will allow for simulation of some of the wake details

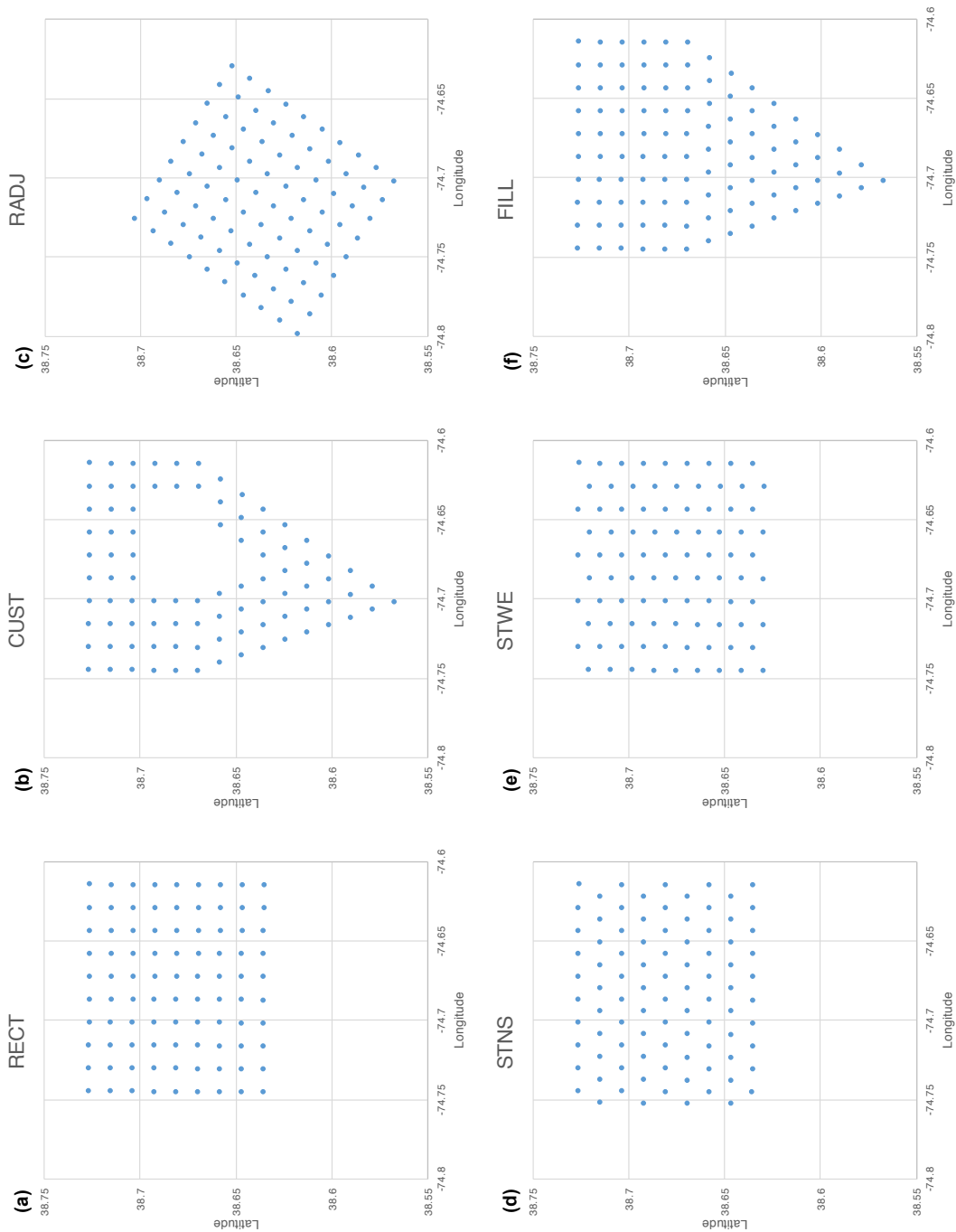


Figure 5.1: The layouts of the 6 modeled wind farms. (a) RECT; (b) CUST; (c) RADJ; (d) STNS; (e) STWE; (f) FILL.

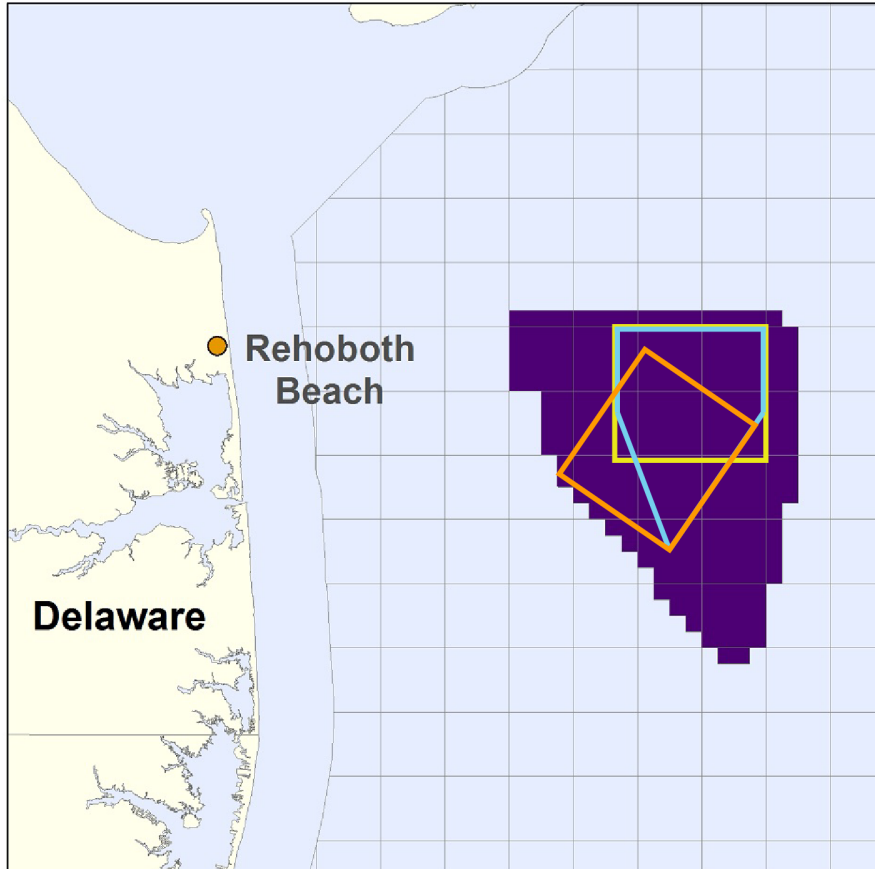


Figure 5.2: Map showing the area of the five modeled wind farms in this study, superposed on the Delaware Wind Energy Area lease area (purple). The yellow line shows the rectangular array (RECT), the blue the custom shape (CUST), and the orange the rotated rectangle (RADJ). The staggered rectangles are located in the same area as the regular rectangle shown here, albeit with the western border being located 630 m more to the west for STNS and the southern border being located 630 m to the south for STWE. Image adapted from [Bureau of Ocean Energy Management \(2015\)](#) image of lease area.

introduced by the wind farms, without exceeding the acceptable limits of fine-scale modeling and near-wake effects using WRF (Carvalho et al., 2012). The nesting was set to be one-way, after sensitivity runs with one- and two-way nesting found that the results from each type of nesting were comparable, but one-way nesting provided a significant boost in computational efficiency.

To characterize the impacts of the wind turbines on the wind as accurately as possible, the model vertical resolution was designed to capture as much variability within the rotor area as possible, without making the model numerically unstable. The vertical model structure of 48 levels, very close together near the surface, was calculated using a tanh algorithm developed by Vanderwende et al. (2015) and Vanderwende and Lundquist (2015). This resulted in a set of very closely spaced levels near the surface with a layer thickness of 13 m, gradually increasing to 37 m in layer thickness above the wind turbine’s rotors, before reaching a uniformly thick set of layers of about 500 m for the top half of the model atmosphere. The vertical structure is detailed in Table 5.6, and shown in Figure 5.4. As can be seen, the vertical layers include 2 below the rotor, and 7 within the rotor disk area, allowing for sufficient modeling of the dynamics occurring within the turbine’s area of immediate influence. The model’s vertical structure is the same in all domains.

5.2.2 Forcing Data and Model Physics

The forcing dataset selected for this suite of model runs was the North American Regional Reanalysis (NARR, Mesinger et al., 2006). The NARR dataset combines a vast array of observational data with model results, going back as far as 1979, and is easily accessible through NCEI’s NOMADS data server (Rutledge et al., 2006)³. The NARR dataset was selected due to the established reliability of the dataset by combining observations and modeling at a high enough resolution to allow for a smaller, more finely resolved WRF outer domain. NARR data are easily processed by the WPS as initial and boundary conditions for WRF.

³ <http://nomads.ncdc.noaa.gov/data.php>

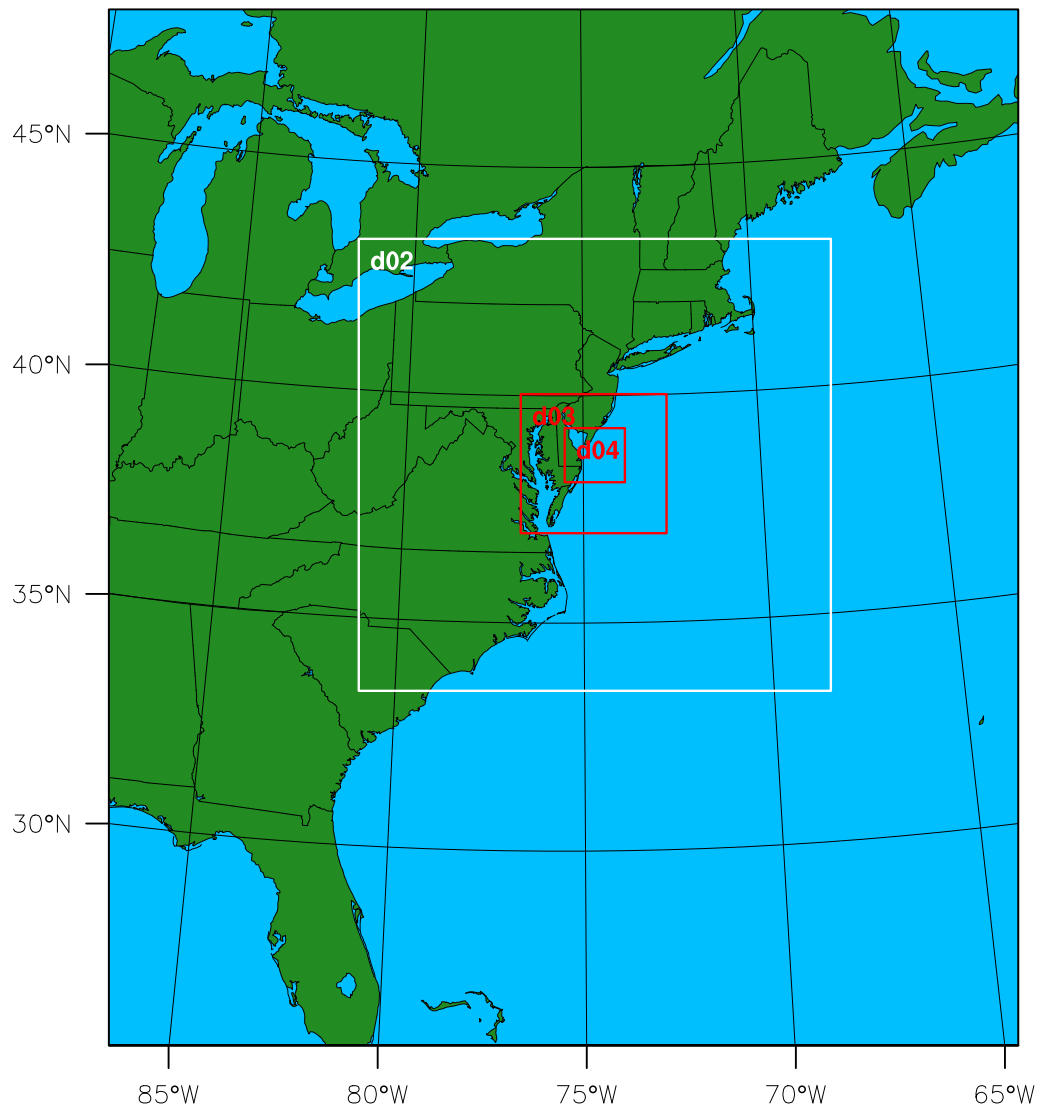


Figure 5.3: The WRF modeling domains for the regional modeling study.

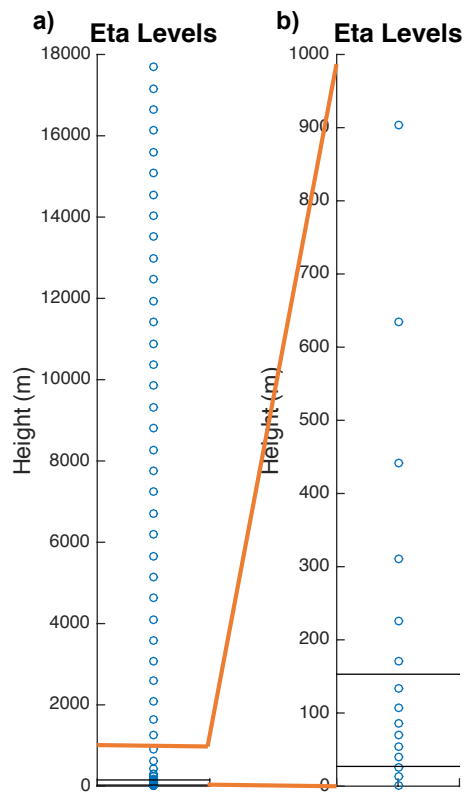


Figure 5.4: The vertical structure of the WRF model for all domains, with blue circles showing each model level, assuming a surface at 0 m AMSL and at 1013.25 hPa, and a model top at 100 hPa. (a) shows the entire atmosphere, while (b) only shows the lowest kilometer. The black lines show the turbine rotor disk area.

Table 5.6: The vertical structure of the WRF domains, assuming the surface is at 0 m AMSL and with a surface pressure at 1013.25 hPa, with a model top of 100 hPa.

η Level	Pressure (hPa)	Height (m AGL)	Thickness (m)
1.000 000	1013.25	0.0	N/A
0.998 100	1011.51	13.1	13.1
0.996 179	1009.76	26.4	13.3
0.994 215	1007.97	39.9	13.6
0.992 173	1006.10	54.1	14.1
0.989 987	1004.11	69.3	15.2
0.987 536	1001.87	86.3	17.0
0.984 608	999.19	106.7	20.4
0.980 826	995.74	133.2	26.5
0.975 548	990.92	170.3	37.1
0.967 721	983.77	225.6	55.3
0.955 770	972.86	310.8	85.2
0.937 666	956.32	441.8	131.0
0.911 461	932.39	635.4	193.6
0.876 280	900.26	903.3	267.9
0.833 099	860.83	1245.5	342.2
0.784 447	816.40	1650.4	404.9
0.733 249	769.64	2101.0	450.6
0.681 876	722.72	2581.5	480.5
0.631 864	677.05	3080.2	498.8
0.584 047	633.38	3589.6	509.4
0.538 803	592.06	4105.0	515.4
0.496 242	553.19	4623.8	518.8
0.456 337	516.75	5144.5	520.7
0.418 990	482.64	5666.1	521.7
0.384 071	450.75	6188.4	522.3
0.351 440	420.95	6711.0	522.6
0.320 957	393.11	7233.7	522.7
0.292 485	367.11	7756.5	522.8
0.265 894	342.83	8279.4	522.9
0.241 060	320.15	8802.3	522.9
0.217 868	298.97	9325.2	522.9
0.196 211	279.19	9848.2	522.9

(continued on next page)

Table 5.6: continued

η Level	Pressure (hPa)	Height (m AGL)	Thickness (m)
0.175 986	260.72	10 371.1	522.9
0.157 099	243.47	10 894.1	522.9
0.139 461	227.36	11 417.0	522.9
0.122 990	212.32	11 939.9	522.9
0.107 609	198.27	12 462.9	522.9
0.093 246	185.16	12 985.8	522.9
0.079 833	172.91	13 508.8	522.9
0.067 307	161.47	14 031.7	522.9
0.055 610	150.79	14 554.7	522.9
0.044 686	140.81	15 077.6	522.9
0.034 486	131.49	15 600.5	522.9
0.024 960	122.79	16 123.5	522.9
0.016 065	114.67	16 646.4	522.9
0.007 758	107.08	17 169.4	522.9
0.000 000	100.00	17 692.3	522.9

The WRF model runs are set up to provide a 24-hour simulation for the entire calendar date of the particular case study (00Z on the day of the event to 00Z the following day). The model runs also include 6 hours of spin-up time, so each model run starts at 18Z the day before the case study date and runs for a total of 30 hours. The model output for the spin-up period is not included in the analysis, but are necessary to ensure the model is producing stable and accurate results for the time period of interest. The model is therefore initialized using the NARR data for 18Z on the day before the case study date, and is forced every 3 hours with NARR boundary conditions for d01 until 00Z the day following the case study date. The NARR data is only used for initial conditions in the inner domains: each inner domain receives its boundary conditions from its parent nest.

The physics parameterizations selected for these WRF runs are similar to, but not identical to, the options used in the ramp forecasting study in Chapter 4. The Mellor-Yamada-Nakanishi-Niino Level 2.5 (MYNN2, [Nakanishi and Niino, 2006](#)) planetary boundary layer scheme and MYNN surface layer scheme are selected to handle the

boundary layer physics, as the [Fitch et al. \(2012\)](#) wind turbine parameterization only works when using the MYNN2 PBL scheme. The Thompson microphysics ([Thompson et al., 2008](#)) was used since recent research has indicated that the Thompson scheme performs well for forecasting in the wind energy industry ([Davis et al., 2013](#)), with some seasonal and regional dependencies ([Cheng et al., 2013](#)). Cumulus convection was parameterized for the 17.01 km (d01) nest using the Betts-Miller-Janjić Eta operational scheme([Janjić, 1994](#)), with the parameterization turned off for the remaining nests, due to WRF’s ability to explicitly model convection at finer grid scales ([Wang and Seaman, 1997](#); [Gilliland and Rowe, 2007](#)). Finally, the wind turbine parameterization was enabled within the innermost nest (d04) to ensure the wind farm impacts would only be measured at the finest available grid scale, and not influence the predictions in the parent nests which might propagate into the innermost nest. Preliminary test runs performed while setting up the domains indicated that very little information will be lost without the innermost nest feeding back to its parent, as the innermost domain was large enough to contain the farms’ wake effects. A detailed list of the selected physics parameterizations is available in [Table 5.7](#).

5.3 Model Results

Analysis of the model output is done in several stages. First, the power production of each farm for each case study is evaluated, based on the energy produced by the turbines within the parameterized wind farm. The atmospheric conditions experienced by the farm, and influenced by the turbines, are also evaluated. Finally, the power production from the case studies are used to estimate an expected annual average power production based on the distribution of synoptic types, and the average power calculated in the model during those synoptic conditions.

5.3.1 Wind Energy Production of the Primary Farms

A typical resource assessment calculates wind energy production using the wind speed at the hub height of the turbines. As discussed in [Section 2.6](#), the [Fitch et al.](#)

Table 5.7: Parameterizations selected for the model runs conducted using WRF for the regional study.

Option	Setting	Reference
Planetary boundary layer (PBL) scheme	Mellor-Yamada-Nakanishi-Niino Level 2.5 (MYNN2)	Nakanishi and Niino (2006)
Surface layer scheme	MYNN	Nakanishi and Niino (2006)
Land surface scheme	Noah land surface model	Mlawer et al. (1997)
Microphysics scheme	Thompson double-moment 5-class graupel	Thompson et al. (2008)
Cumulus parameterization	Betts-Miller-Janjić Eta operational for 17.01 km parent nest, none for child nests	Janjić (1994)
Longwave radiation scheme	Rapid Radiative Transfer Model (RRTM)	Chen and Dudhia (2001)
Shortwave radiation scheme	Dudhia	Dudhia (1989)

(2012) parameterization calculates the power produced by the turbine in each grid box using Equation 2.22. WRF outputs the value of the power produced in each horizontal grid cell in the main output file when the Fitch parameterization is active. Since these numbers are calculated within every vertical layer that the rotor passes through, these numbers are a more accurate representation of the actual power produced by the wind turbine than just estimating power using hub height winds, since it accounts for variable wind speeds within the vertical profile of the turbine rotor.

There are several methods to evaluate the power output of the wind farms modeled, each providing a different information. Since the Fitch parameterization calculates power production in each grid box, and the model domains set up for this project contain no more than 1 turbine per grid cell, the output data therefore is indicating the power output by each individual turbine at each output timestep (instantaneous power output, in kW). If the model domain contained more than one wind turbine in a grid cell, the information on individual turbine power output would be lost, since the calculations are done on a per grid cell basis. This allows for observing how the wind farm responds to meteorological changes throughout the model forecast period, at 10 minute intervals (the chosen output timestep). Next, the total energy produced by each turbine for the entire 24 hour case study is calculated by adding all of these 10 minute values of power production, and dividing by the number of observations per hour (6), in order to give total daily energy production for each turbine (in kWh). From this, the average power output for that day can also be calculated. Additionally, these numbers can be summed in order to give total power production for the entire farm.

It is also important to consider the capacity factor of each turbine and of the farm as a whole. The capacity factor CF is the ratio between the power/energy produced and the power/energy the turbine or farm would have produced if it were producing full rated power at the given time or interval, $CF = P/P_R$, where P is the produced power and P_R is the rated power (Manwell et al., 2010). Capacity factor is typically expressed as a value between 0 and 1, or occasionally as a percent. The capacity factor

is an easy way to determine how productive the turbines or the farm is for any given time or interval, and makes for easy comparisons between different farms, particularly if they have a different number of turbines. Much of the following discussion will focus on capacity factor, although actual power/energy production will be used for certain improvement comparisons and cost considerations.

An overall view of the predicted wind productivity for all of the case studies is shown in Figure 5.5. These figures depict the overall daily capacity factor for each of the case study events for both the RECT and CUST shapes. On average, the winter is a more productive season than the summer, as indicated by the fact that there are more points with higher capacity factors. The winter also had 4 case studies where the farm was producing full power; 2007-02-14, 2007-12-17, 2008-12-10, and 2010-02-26. The daily power production is also much more variable in the wintertime, as indicated by the tremendous range of capacity factors seen in Figure 5.5a. During the summer, the wind farms do not produce full power at any time; however, there are only two cases (2008-07-15 and 2007-06-30) where the power output is near zero. Overall, daily wind productivity is less variable in the summer months, and almost all of the case studies are concentrated below on daily capacity factors of $CF < 0.5$.

The actual power produced during each case study, along with their corresponding capacity factors, are used to analyze the results of these model runs. The results indicate that CUST outperforms RECT in every case study except one (2005-06-07), sometimes only slightly, occasionally more noticeably, such as on 2007-12-23. This improvement indicates that thoughtful consideration of the geometry of the wind farm can lead to improved performance. The factors that lead to improved performance will be examined and evaluated in Section 5.3.2.

These overall case study power production and capacity factors allow for analysis of how the farm as a whole performs on a daily basis. However, there is a large amount of variability within the farm, and on an intradaily timeframe. These metrics are important for evaluating the wind farm's ability to help meet electricity load, and provide power when it's needed. To begin this discussion, Figure 5.6 shows the

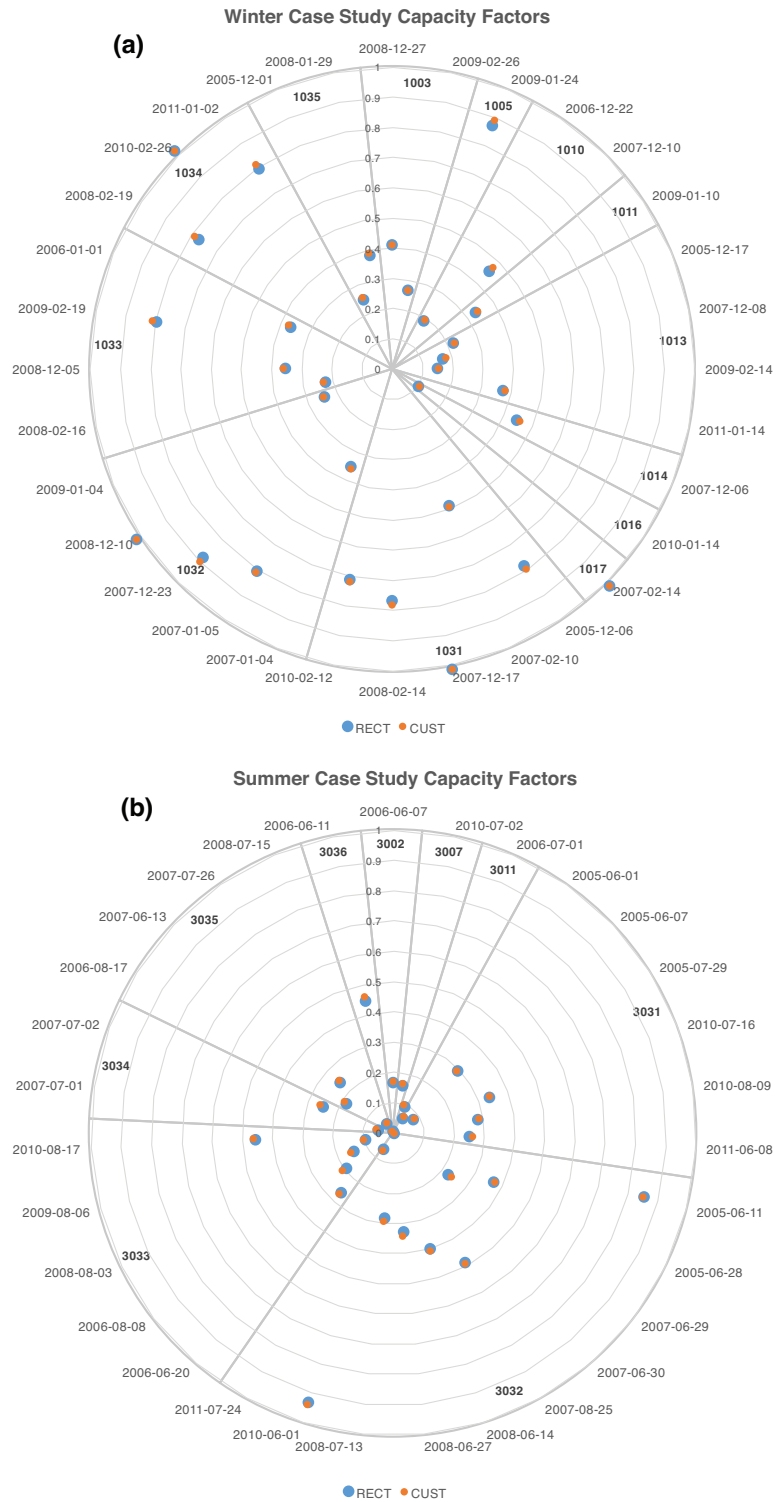


Figure 5.5: The daily capacity factor predicted by WRF for all case studies, for RECT and CUST farm layout for (a) the winter, and (b) the summer.

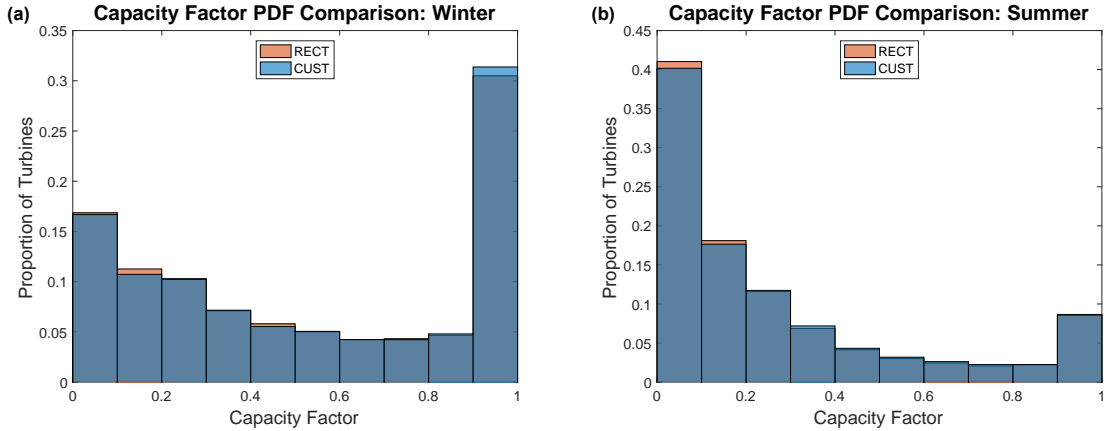


Figure 5.6: Probability distribution of capacity factors for each individual turbine at all model timesteps for all of the case studies for (a) winter synoptic types, and (b) summer synoptic types. Note the gray-blue colored areas are where the blue and red bars overlap.

probability distribution of each wind turbine in the RECT and CUST scenarios at every model output time (10 minutes) for all case studies in each season. The most significant note here is that during the winter, $CF > 0.9$ occurs more than 30% of the time, while during the summer, it occurs less than 10% of the time. Conversely, during the summer, $CF < 0.1$ takes place about 40% of the time, and less than 20% of the time during the winter. This bimodal distribution suggests that in both seasons, many turbines are either producing no or little power, or full or nearly full power for about half of the time. This is an indicator that the wind regime has a significant amount of time where the wind is either calm or weak, or at wind speeds at or exceeding the design speed of the turbine – when the wind is blowing, particularly in the winter, it can provide significant power. This figure also shows that CUST has a higher proportion of wind turbines producing at higher levels ($0.8 < CF < 1.0$), resulting in its improved overall performance.

The overall farm performance can also be compared by evaluating the total farm capacity factor at every model output time (every 10 minutes). Figure 5.7 compares the capacity factor of each farm, where each dot represents one particular time during a case study. The black line is the 1:1 ratio, where the two farms' capacity factors are

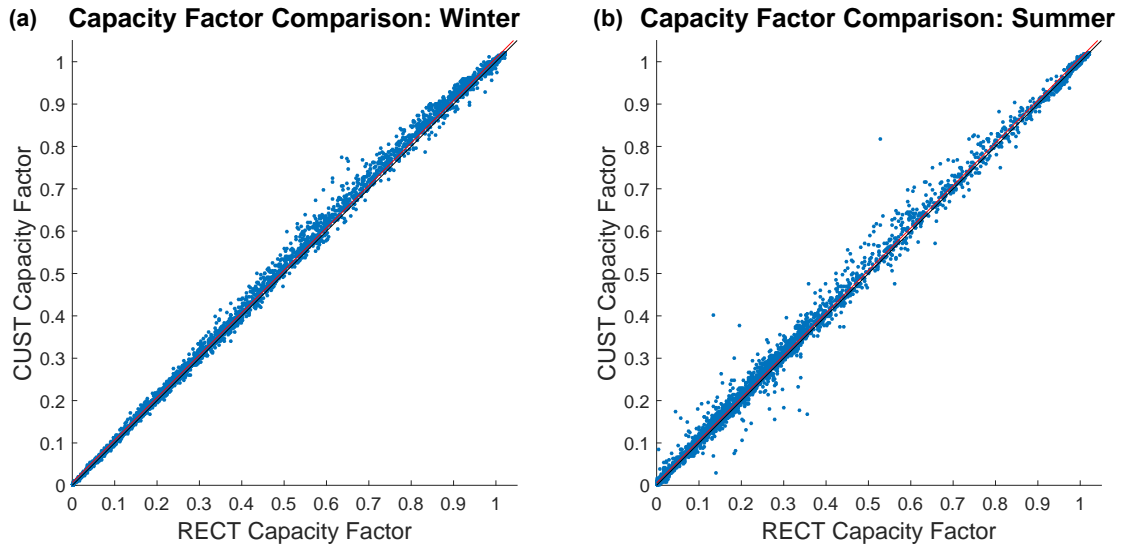


Figure 5.7: Comparison between total farm capacity factor for RECT and CUST at every time interval for all case studies run. The black line depicts the 1:1 ratio line, where the CF of the two farms is equal; the red line is the least-squares regression line of the data points. (a) shows winter synoptic types, and (b) shows summer synoptic types.

equal. Points above this line are times where CUST is performing better than RECT; points below this line indicate the opposite. Notice that in both seasons, the majority of points fall above the 1:1 line, indicative of the CUST farm's improved performance. During the winter (Figure 5.7a), the concentration of high capacity factors can clearly be seen; the rest of the dots are relatively uniformly distributed along the line. Also notice that there is more variability in the middle ($0.5 < CF < 0.7$), particularly for RECT, and the productivity tends to be close to equal at extreme CF . This indicates that during the winter, CUST seems to be particularly beneficial with higher capacity factors ($0.5 < CF < 0.9$), corresponding to wind speeds between about 9 m s^{-1} to 13 m s^{-1} .

During the summer (Figure 5.7b), there is much more variability in wind farm performance than there is in the winter, including a couple outliers. The high concentration of capacity factors at lower levels is clear, and indicative of the weaker average winds in the summer. Similarly to the winter, CUST gives the greatest benefit over

RECT for $0.4 < CF < 0.8$, indicating that the best improvement in power occurs in the middle range of power production.

5.3.2 Wind Energy Production of the Supplemental Farms

The two primary farms discussed in Section 5.3.1, RECT and CUST, are useful to examine two possible scenarios of wind farm geometry for the Delaware WEA. However, the custom shape has several factors to improve its performance, including knowledge gained from the basic geometric shape study discussed in Chapter 3. Therefore, as described in Section 5.2.1, the performance of four supplemental farms is also examined for a subset of the case study dates, based on the results of the RECT and CUST runs. This allows for an examination of the factors that are most relevant to the success of the CUST farm, and of what meteorological conditions are more influential in the performance of these arrays.

In terms of overall performance, no one farm consistently outperforms any others; each of the supplemental farms has an advantage under certain circumstances, and outperforms CUST in certain cases. An overview of the general trends can be seen in Figure 5.8, comparing the average wind farm capacity factors at each time step during all of the selected model runs. The RADJ farm has the greatest amount of variability, as indicated by the fact that the points are less focused on the 1:1 ratio line, where RADJ and RECT performance would be equal. Additionally, while there are a lot of points above the line, some rather significantly, there are roughly a similar number of points below the line. This indicates that the rotation angle of a rectangular array can have a significant impact on power production, and the correct orientation must be carefully considered in the wind farm design phase.

STWE shows the least amount of variability, with performance close to the 1:1 ratio line. There is a slight benefit to the STWE shape at lower capacity factors, indicating that some of the lighter winds may correspond to a west-east wind direction. Conversely, STNS shows a reasonable performance improvement over RECT throughout the capacity factor range, with few points below the 1:1 ratio line. This result

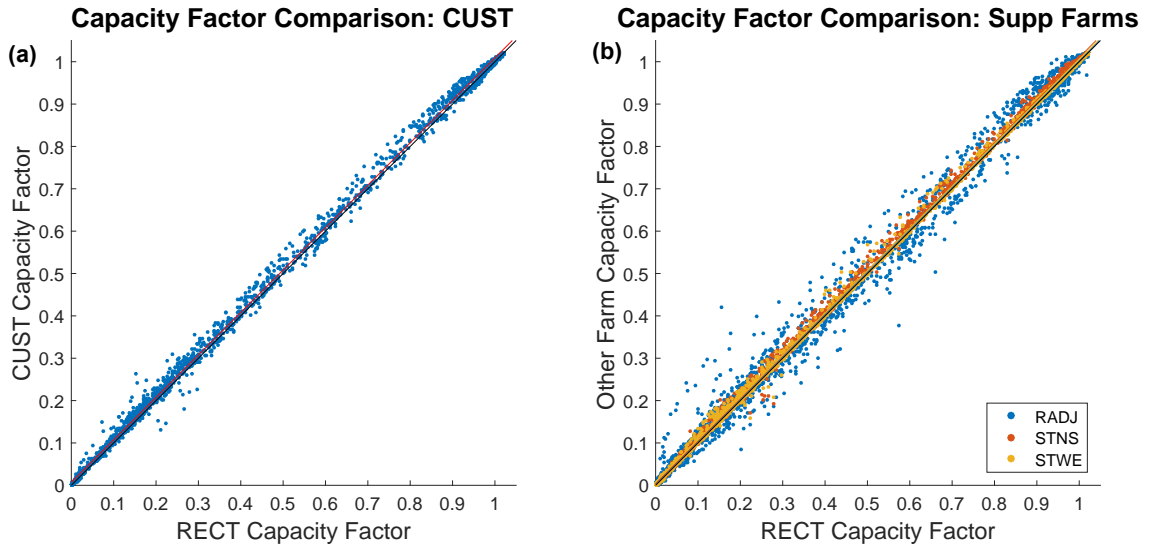


Figure 5.8: Comparison between total farm capacity factor for RECT, CUST, and the 3 supplemental farm shapes at every time step for the selected cased studies explored using all of the supplemental shapes. The black line depicts the 1:1 ratio line, where the CF of the two farms is equal; the red line is the least-squares regression line of the data points. (a) shows RECT v. CUST for only the selected case studies, and (b) shows the three supplemental farm shapes compared to RECT.

indicates that either the farm performance is less sensitive to the layout than might be expected.

The FILL supplemental farm shape was modeled in order to evaluate the influence of the open space, or courtyard, within the CUST shape, with focus on how the presence of the courtyard may improve wind farm performance by giving the winds a chance to recover some of their speed and allow some of the turbulent wakes to dissipate somewhat. It is important to note that directly comparing the power production of FILL to the other farms can be misleading; FILL contains an additional 15 wind turbines, and therefore has an overall increase in power capacity of 16.7% or 75 MW_c , for a total farm capacity of 525 MW_c . As a result, the FILL scenario always produces the most daily power. However, the daily average capacity factor for each case modeled is always lower than the capacity factor in the CUST scenario, due to the decreased efficiency of the increased number of turbines, and the loss of the spacing gap within the farm.

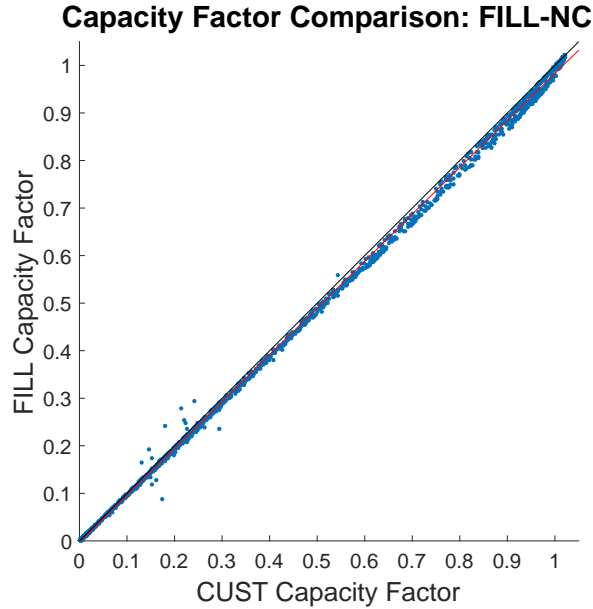


Figure 5.9: Comparison between total farm capacity factor for CUST and FILL-NC at every time step for the selected case studies explored using all of the supplemental shapes. The black line depicts the 1:1 ratio line, where the CF of the two farms is equal; the red line is the least-squares regression line of the data points.

In addition to examining FILL as-is, analysis was also performed on FILL after removing the power results for the 15 extra turbines from the data (FILL-NC); in other words, FILL-NC only evaluates the turbines in FILL which also exist in CUST. This was done in order to see the impact those central turbines have on the overall wake effects within the farm. Figure 5.9 compares the overall capacity factors of the FILL-NC data with the original CUST layout, and shows that almost all data points fall below the 1:1 ratio line, indicating that, unsurprisingly, the additional wake effects of those central turbines result in a decrease in performance. The outliers are due to the impact of sea breezes on some of the case studies, which cause a highly variable wind field, and will be discussed in Section 5.3.3.

All of the results from the FILL runs are shown in Table 5.8. As mentioned previously, the FILL layout outperformed both RECT and CUST due to the increased number of turbines improving the overall power production: from about 9% to 20%

compared to RECT, and 6.5% to 15% compared to CUST. In no case does FILL outperform CUST by more than the 16.7% increase in power capacity resulting from the additional turbines, demonstrating the necessary trade-off between adding additional turbines in order to increase overall power output, and seeing a reduction in performance efficiency due to increased wake effects. When including only the FILL-NC turbines, the RECT layout is outperformed in 9 out of the 14 cases, but in no case is the CUST farm outperformed, indicating the impact of the reduced wakes in the CUST layout, with a power output reduction ranging between 0.7% and 6.4%.

5.3.3 Meteorological Factors

Since the power production of wind farms are dictated by the meteorological conditions, there are a variety of different meteorological scenarios that influence farm output. Therefore, several of the case studies are examined in additional detail, to further assess the influence of the variability in meteorological conditions on the wind farm.

The first case for evaluation is 2007-08-25, which is of synoptic type 3032, a summertime synoptic type characterized by southerly flow. As shown in Table 5.2, this is the most common summer synoptic type, accounting for roughly 1/3 of the summer days from 2005–2011. This case was one of those selected for modeling with all of the supplemental farms, and the results of those model runs can be seen in Table 5.9. Overall, CUST slightly outperforms RECT in power production in this scenario. The influence of the various grid layout changes utilized in CUST on its improved power production can be seen by looking at the influence of RADJ and STNS on the farm performance. Staggering the turbines in a north-south (STNS) direction has a significant influence on the farm’s performance (2.41%), while rotation of the farm (RADJ) decreased wind farm performance (–1.16%). This indicates that the staggering effect was the most significant factor on the CUST scenario’s improved performance. To assess the influence of the wakes, the wind conditions at 18Z in the

Table 5.8: Comparison of different custom-shaped farms. Note that FILL-NC is the FILL layout with the 15 extra turbines from the center removed for the data analysis, thereby only showing the wake impacts those turbines would cause to the rest of the 90 turbines. RECT Chg shows the change from the RECT layout, while CUST Chg shows the change from the CUST layout.

Date	RECT		CUST		FILL		FILL-NC		
	Ttl Energy (MWh)	Ttl Energy (MWh)	Ttl Energy (MWh)	Ttl Energy (MWh)	RECT Chg %	CUST Chg %	Ttl Energy (MWh)	RECT Chg %	CUST Chg %
2009-02-26	2862.9	2865.2	3141.0	3141.0	9.7	9.6	9525.6	-3.4	-3.5
2009-01-24	9401.4	9615.7	11042.8	11042.8	17.5	14.8	9525.6	1.3	-0.9
2007-12-10	4897.3	5109.6	5701.3	5701.3	16.4	11.6	4960.2	1.3	-2.9
2007-12-08	1864.0	1969.2	2241.1	2241.1	20.2	13.8	1937.6	4.0	-1.6
2008-02-14	8318.7	8459.7	9754.3	9754.3	17.3	15.3	8399.5	1.0	-0.7
2007-01-05	8697.2	8743.0	10004.0	10004.0	15.0	14.4	8640.7	-0.7	-1.2
2008-02-16	2440.0	2515.9	2850.1	2850.1	16.8	13.3	2465.3	1.0	-2.0
2005-06-01	599.8	672.6	723.7	723.7	20.7	7.6	629.7	5.0	-6.4
2005-06-07	3165.1	3158.1	3436.7	3436.7	8.6	8.8	3041.2	-3.9	-3.7
2005-06-11	9235.8	9237.5	10247.3	10247.3	11.0	10.9	8922.6	-3.4	-3.4
2007-06-30	54.2	59.5	63.4	63.4	16.9	6.5	56.5	4.2	-5.0
2007-08-25	5325.0	5361.6	5921.4	5921.4	11.2	10.4	5193.0	-2.5	-3.2
2008-06-27	3559.9	3720.5	4119.7	4119.7	15.7	10.7	3608.2	1.4	-3.0
2006-08-08	2102.9	2246.6	2496.0	2496.0	18.7	11.1	2190.2	4.2	-2.5

Table 5.9: Performance of the modeled farms for the 2007-08-25 case study. Ttl Energy is the total energy produced by the entire farm for the 24-hr period. Avg Turb Energy is the average total energy produced by each turbine during the 24-hr period. The Farm CF is the overall capacity factor of the farm for the same period. The two Impr. columns indicate the improvement of each farm shape over RECT, where a negative number indicates that RECT outperformed that model farm.

Farm	Ttl Energy (MWh)	Avg Turb Energy (MWh)	Farm CF	Impr. (MWh)	Impr. %
RECT	5324.95	59.17	0.493		
CUST	5361.61	59.57	0.496	36.66	0.69
RADJ	5263.30	58.48	0.487	-61.65	-1.16
STNS	5453.03	60.59	0.505	128.08	2.41
STWE	5323.42	59.15	0.493	-1.53	-0.03

control case (CTRL), along with the difference in wind speed seen in 5 of the farm shapes, is shown in Figure 5.10.

A second example of a meteorological condition that impacts the farm performance is on 2008-02-14, which is of synoptic type 1031, characterized by strong northwestern flow. It is the most common winter synoptic type, occurring 16.6% of the time between 2005 and 2011, and 17.9% over the entire record. As can be seen in Figure 5.11a, this northwest flow results in winds that are channeled down the Delaware Bay. This leads to the strongest winds being located directly downwind of the mouth of the bay. The wakes produced during this case study are rather weak, as seen in the remaining images in Figure 5.11, due to the fact that prior to 18Z (the time of this figure), the winds were considerably stronger, resulting in full power throughout the farm, which reduces the wake effects due to the excessive wind. The winds began to weaken at around 16Z, but the wakes remain rather weak. However, what can be seen in this figure is the impact of the farm location in being directly downwind of the bay. In particular, the RADJ shape is located almost entirely downwind of the bay's mouth, as opposed to RECT. To examine this effect, an additional rotated farm was modeled (ROTD, Figure 5.11e), which is just the RECT shape rotated but left in the same position as RECT, instead of moved in order to parallel the southeast edge of

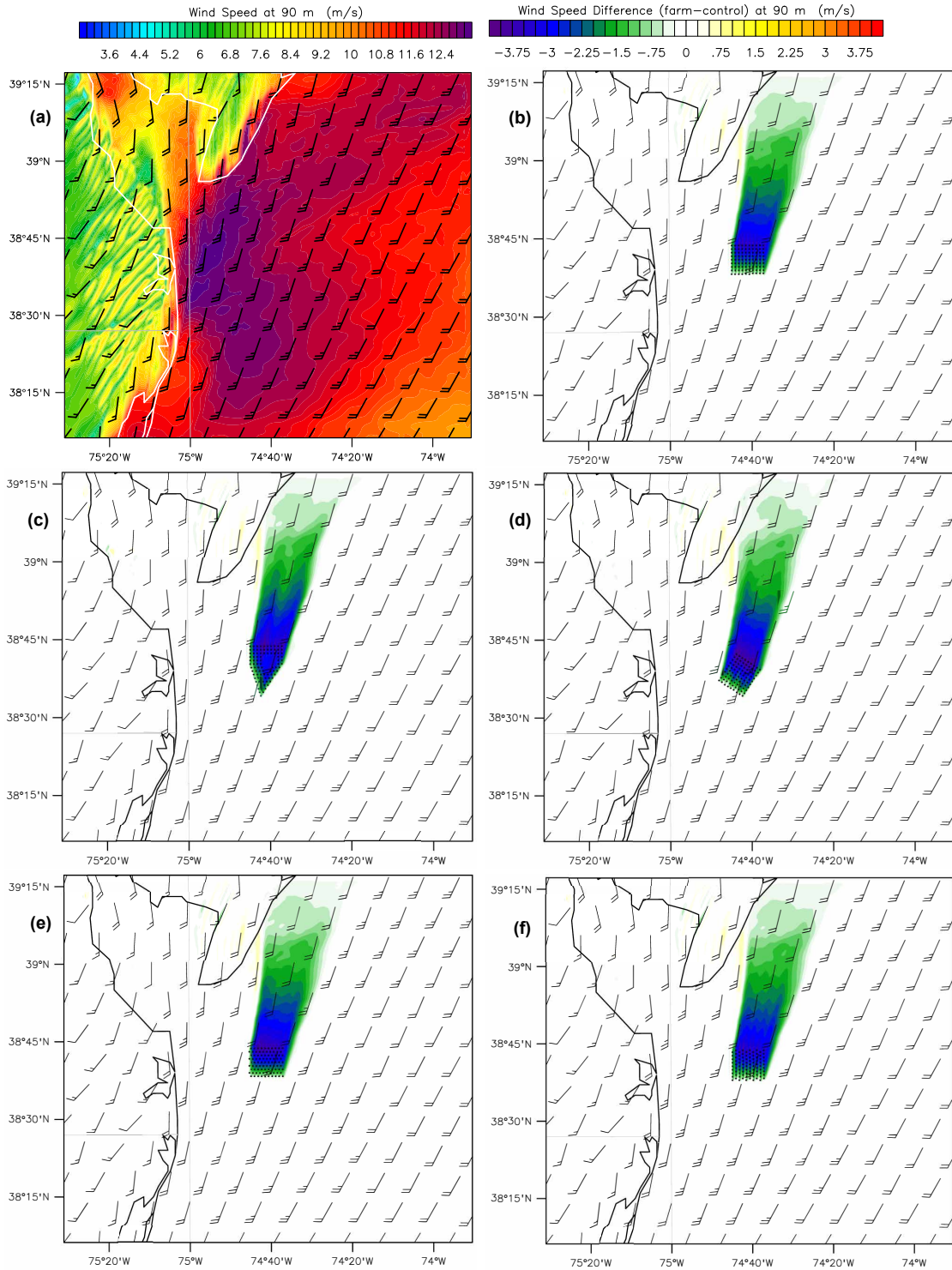


Figure 5.10: Winds as modeled in the innermost domain for the 2007-08-25 case study date at 18Z. (a) shows the control case (CTRL) with no wind farm, while (b) through (f) depict the difference in wind speeds between a farm scenario, and the control (FARM-CTRL). (b) RECT; (c) CUST; (d) RADJ; (e) STNS; (f) STWE.

Table 5.10: Performance of the modeled farms for the 2008-02-14 case study. Ttl Energy is the total energy produced by the entire farm for the 24-hr period. Avg Turb Energy is the average total energy produced by each turbine during the 24-hr period. The Farm CF is the overall capacity factor of the farm for the same period. The two Impr. columns indicate the improvement of each farm shape over RECT, where a negative number indicates that RECT outperformed that model farm.

Farm	Ttl Energy (MWh)	Avg Turb Energy (MWh)	Farm CF	Impr. (MWh)	Impr. %
RECT	8318.65	92.43	0.770		
CUST	8459.71	94.00	0.783	141.06	1.70
RADJ	8617.29	95.75	0.798	298.64	3.59
STNS	8386.11	93.18	0.776	67.46	0.81
STWE	8344.84	92.72	0.773	26.19	0.31
ROTD	8448.04	93.87	0.782	129.39	1.56

CUST.

The overall performance of these farms for the entire case study date is shown in Table 5.10. As can be seen, the RADJ shape outperformed all of the other farms by a considerable margin: it exceeded RECT by nearly 3.6%. However, the rotation appears to be less significant than the position of the farm overall. The ROTD shape outperforms RECT by 1.56%, compared to the CUST shape outperforming RECT by 1.7%. This effect can be clearly seen in Figure 5.12, which shows the turbine performance throughout the farms at 18Z. The RADJ farm has more turbines in the 3000 kW to 4000 kW range, compared to the other farms which have a significant number of turbines performing below 3000 kW.

5.3.4 Front Row Equivalent Turbine Count

In a wind farm with a simple layout, such as RECT, during certain conditions it is easy to determine which turbines are located in the “front row” and are receiving the most possible power without being influenced by wake effects. However, with wind farms that are arranged with factors intended to maximize wind extraction and minimize wake effects, this can be more difficult to determine. For example, the STNS layout is designed such that the rows of wind turbines are staggered for winds in the

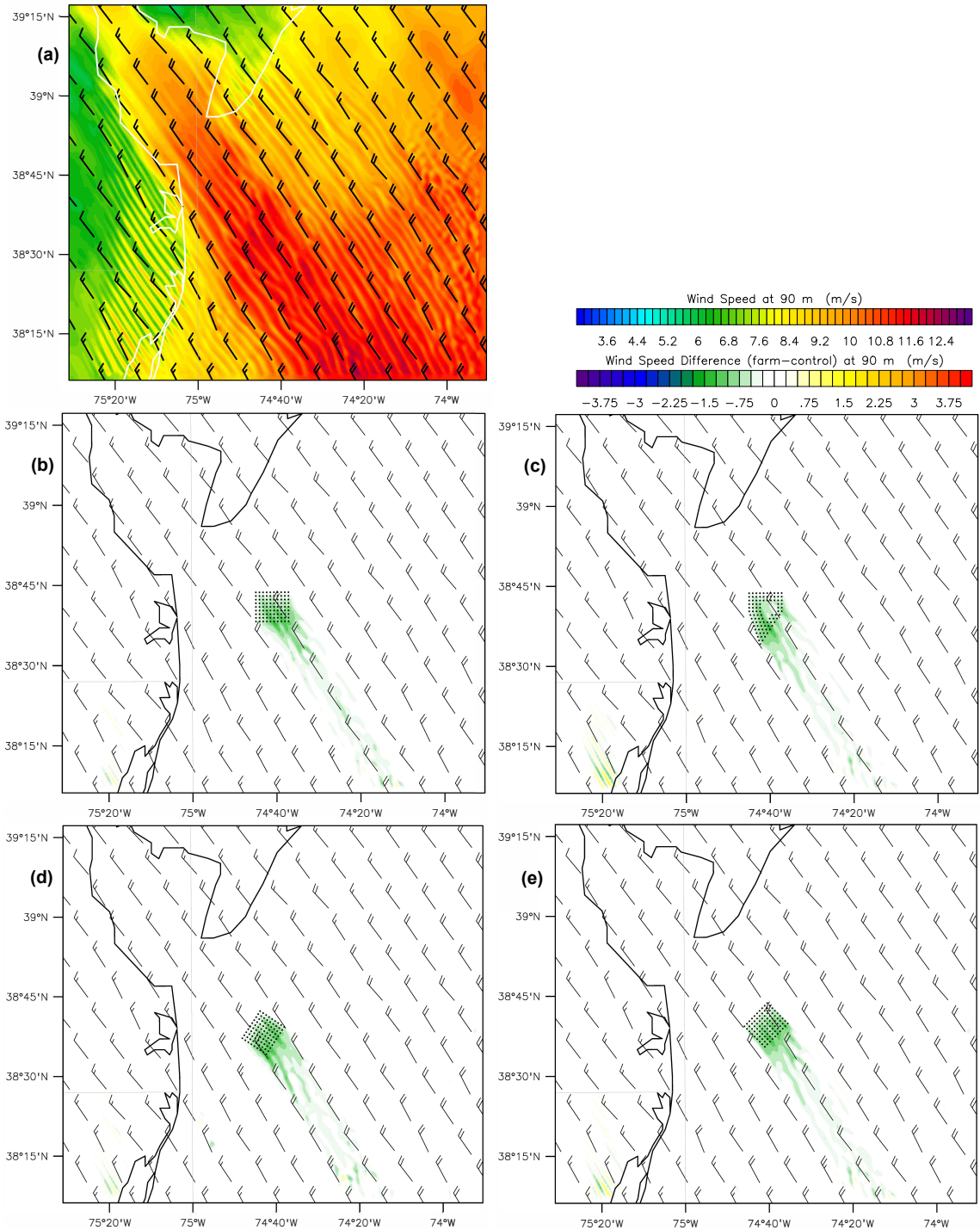


Figure 5.11: Winds as modeled in the innermost domain for the 2008-02-14 case study date at 18Z. (a) shows the control case (CTRL) with no wind farm, while (b) through (d) depict the difference in wind speeds between a farm scenario, and the control (FARM-CTRL). (b) RECT; (c) CUST; (d) RADJ; (e) ROTD.

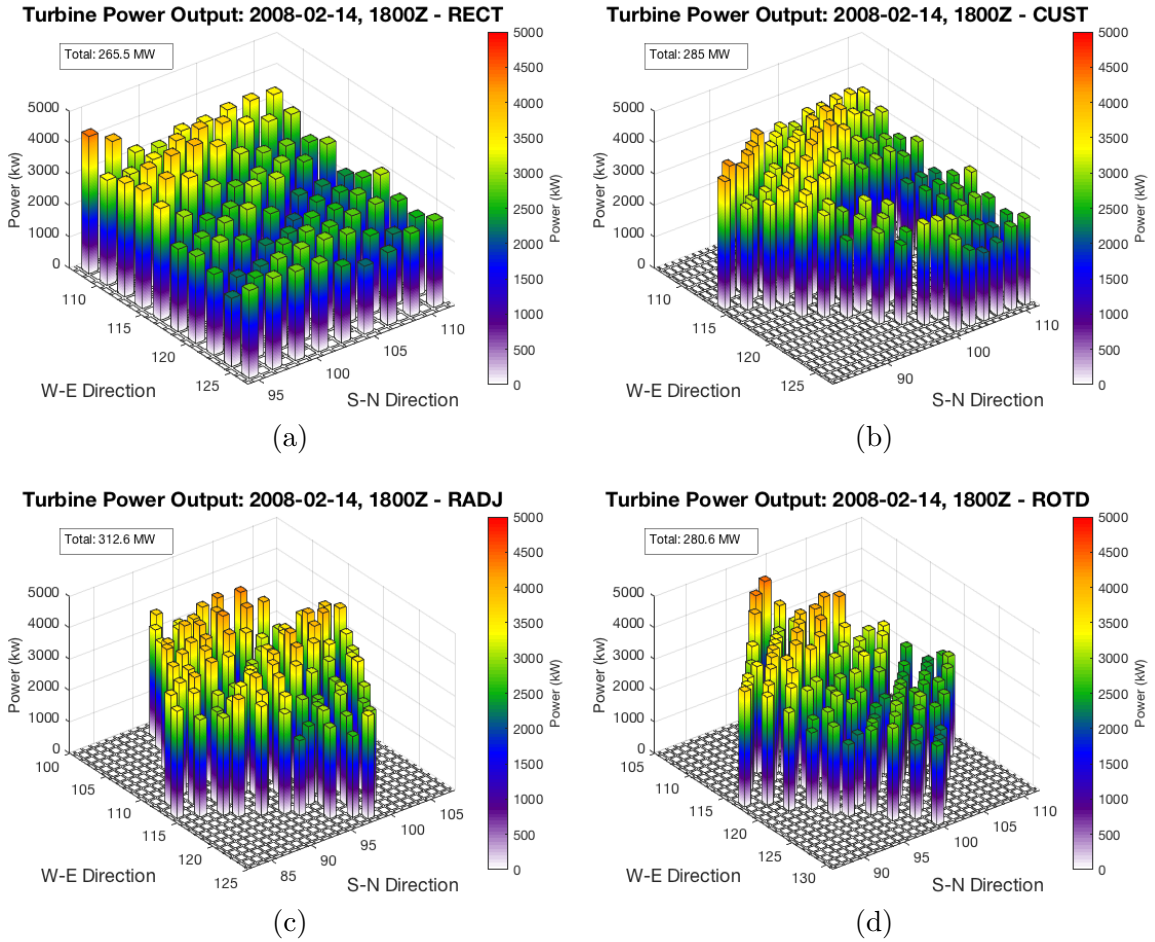


Figure 5.12: The wind turbine productivity for several of the farms at 1800Z on 2008-02-14. The power production of each turbine is represented by a single bar, as arranged in the layout. (a) RECT; (b) CUST; (c) RADJ; (d) ROTD.

north-south direction, resulting in the second row of turbines being less impacted by wakes, and closer to receiving front row winds. But, how can this be evaluated with more complex wind farm shapes, or under less than ideal wind conditions?

One possible method of evaluation is by ordering the turbines from most to least productive at a given time, and examining how the power is reduced by wake effects. The case study date of 2007-08-25 (see Table 5.9 for the summary numbers) is a good case for a first look at this concept, since the winds were out of the south-southwest. The consistent wind conditions throughout the day with little variability make this case very conducive to examining the wake effects for various wind farm layouts under a constant and simple to evaluate wind condition.

The wind farm production at 1800Z for RECT and CUST can be seen in Figure 5.13. In the RECT shape, it can be seen in Figure 5.13a that the wind is clearly coming out of the south, by the clear superior level of power achieved in the first row; the slightly westward component is also seen in the higher power levels on the west side of the farm. In Figure 5.13b, the drop-off in power behind the front row of 10 turbines is evident in the shape of the histogram. The slightly westward component of the southerly wind is also evident in the CUST layout, as seen by the fact that the turbines on the southwest edge perform better than those on the southeast edge in Figure 5.13c. Those few turbines on the southwest edge also slightly outperform those in front row of RECT, seen in Figure 5.13d, leading to a total power production of 286.9 MW. Overall, this farm only performs slightly better for the full day.

The power production characteristics within the supplemental farms at this time can be seen in Figure 5.14. The positive impact of staggering the wind turbines can be seen quite clearly in the STNS layout (Figure 5.14a–b). In addition to the front row achieving a high level of wind power extraction, the second row also remains at a rather high level, easily in excess of 4 MW each, compared to the RECT layout that is well below 4 MW each in the second row. This is particularly clear in the histogram, where there is no rapid drop-off in power after the first 10 turbines, but a more gradual reduction until after turbine 24, due to both the staggering, and the

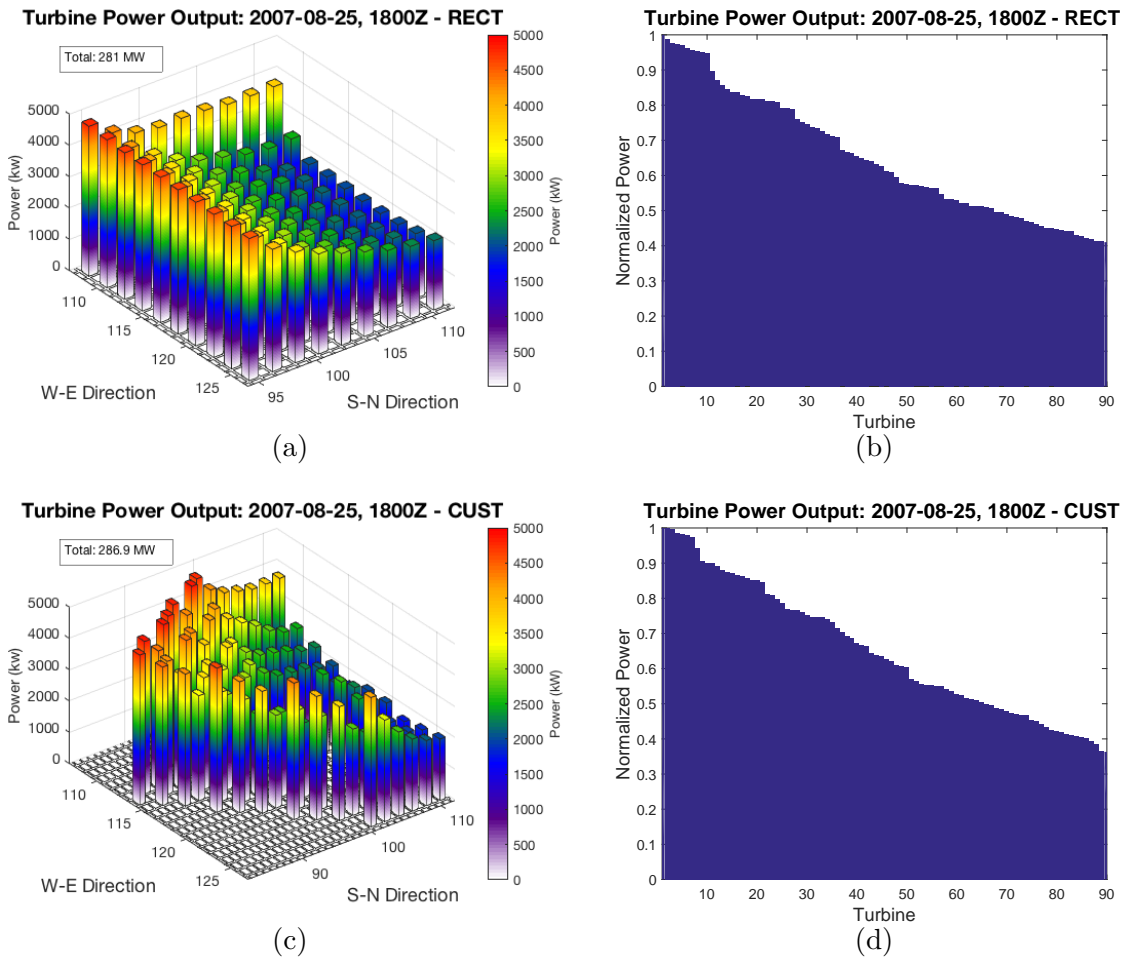


Figure 5.13: The wind farm productivity for the primary farms at 1800Z on 2007-08-25. (a–b) shows the RECT layout, with (a) depicting the power production of each turbine as a single bar, as arranged in the layout, while (b) shows the power production of each turbine in descending order of productivity, normalized by the power output of the most productive turbine. (c–d) is as (a–b), but for the CUST layout.

improved wind productivity of the 4 wind turbines on the westernmost edge that stick out from the rest of the farm. The total power produced at this time by STNS is 301.6 MW, contributing to its overall daily performance improvement over RECT (and, indeed, any other shape).

The power production of STWE (Figure 5.14c–d) looks very similar to RECT, since the staggering for the west-east wind direction does little for a predominantly southerly wind; the power production of STNS is the same as RECT at this time, and roughly the same for the entire day. The RADJ farm (Figure 5.14e–f) also sees a performance boost, outperforming any other farm at this time interval with 304.5 MW of power production, likely due to both the southwesterly orientation of the side of the wind farm with 10 turbines, the improved leading edge on the southeast side, and the staggering effect seen due to the rotation. However, for the entire day, RADJ actually performed slightly worse than RECT.

The concept of “front-row equivalency” is a possible way to quantify what turbines are considered to be in the leading edge of the farm, when combining both the wind direction and how it relates to the orientation of the farm and the actual leading edge, and the level of staggering in that wind direction which causes a second row to also experience near-front row winds. This concept is worthy of further consideration in order to evaluate if there might be a clear productivity level that indicates which turbines are experiencing the front-row effect.

5.3.5 Annual Results

One of the aforementioned benefits of using case studies selected by synoptic type is that these case studies can be used to assess what the overall power production of the farms might be for an entire season or year. This allows for a more thorough assessment of how much wind farm geometry matters, and when it appears to matter most. For this analysis, the chosen case studies were considered representative of their corresponding synoptic types, which then allows for an estimate on the expected power based on the prevalence of the various synoptic types.

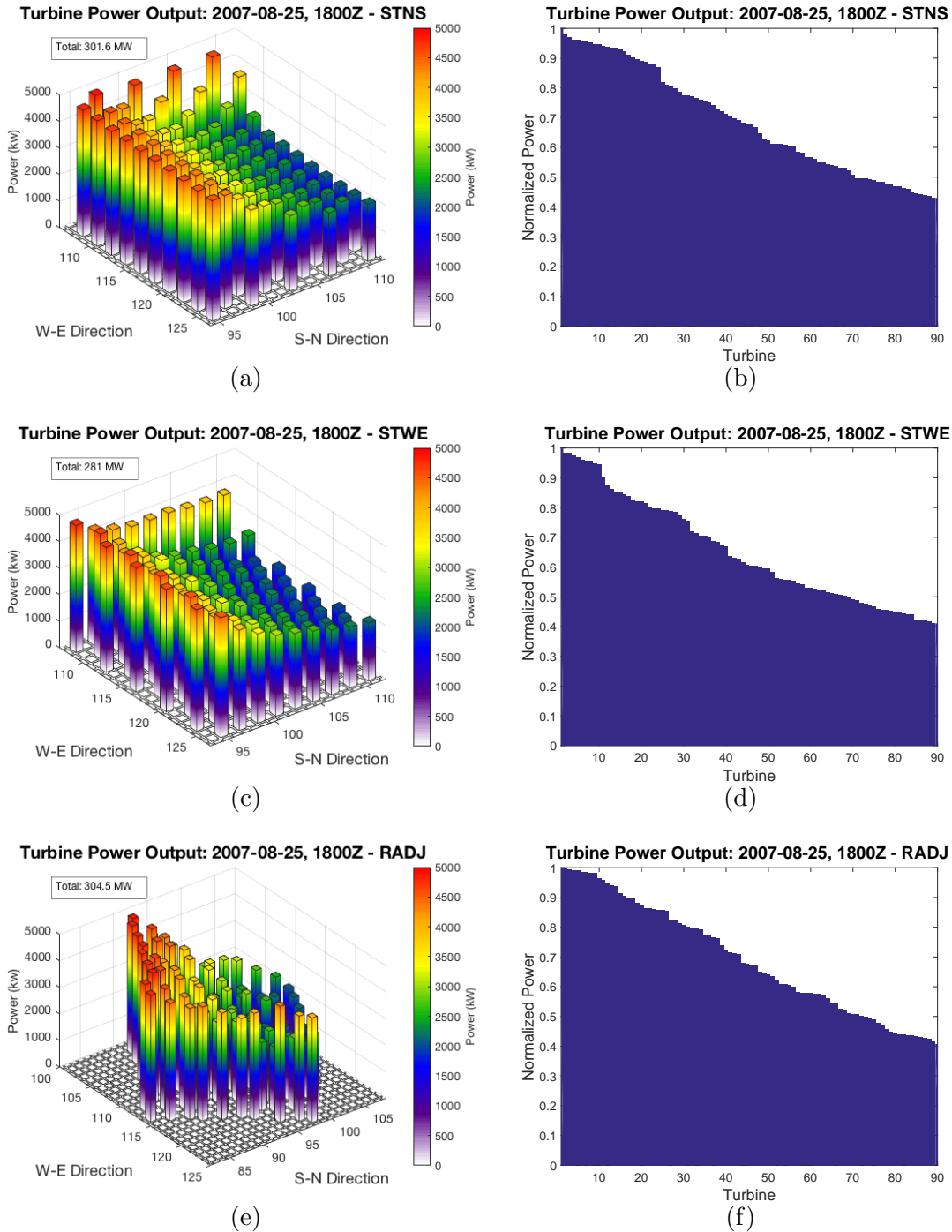


Figure 5.14: Wind farm productivity for the supplemental farms at 1800Z on 2007-08-25. (a–b) shows the STNS layout, with (a) depicting the power production of each turbine as a single bar, as arranged in the layout, while (b) shows the power production of each turbine in descending order of productivity, normalized by the power output of the most productive turbine. (c–d) is as (a–b), but for the STWE layout; (e–f) is as (a–b), but for the RADJ layout.

In order to estimate annual production, the daily energy production results for each case study day were averaged together by synoptic type, in order to calculate the average expected energy production under each synoptic condition. Since the number of case studies for each synoptic type was determined based on the prevalence of that synoptic type, the more common synoptic types have more case study data to average together in order to have a more varied assessment of the energy production that might be expected under that synoptic type, and to not have the entire season's productivity results overly influenced by one case study which may be an outlier. This average was then used to calculate a weighted sum of expected production for the entire season based on the probability distribution of the synoptic types during that season.

The results of this analysis are shown in Table 5.11 for the winter synoptic types, and Table 5.12 for the summer synoptic types. Overall, the use of the custom shape resulted in a greater percentage improvement in power production during the summer season, with a 2.4% improvement on a seasonal basis, while the winter improvement was 1.4%. However, in terms of actual power produced, the custom shape during wintertime produced an extra 7.1 GWh of electricity, as opposed to 6.2 GWh during the summer season, due to the fact that overall, the winter season is windier. For both seasons combined, the use of the custom shape would result in an additional 13.4 GWh of electricity. Based on the U.S. Energy Information Administration's 2014 average household electricity use of 10.9 MWh each year (U.S. Energy Information Administration, 2016a), this is enough electricity to power more than 1200 additional homes.

In order to explore individual turbine performance, a histogram of each turbine's performance at every time interval for all of the case studies throughout the year is shown in Figure 5.15. As in the seasonal plots, there is a large proportion of turbines producing at both very low and very high capacity factors. Overall, CUST has a slight edge over RECT at the higher capacity factors, while RECT has more turbines producing at $CF < 0.2$. This is reflective of the seasonal results shown in Figure 5.6.

To further assess overall farm performance, and the benefits gained from the

Table 5.11: Summary of the calculated energy production for the entire winter season based on the synoptic type distribution.

Type	Cases	Days	RECT				CUST			
			Avg Prod (MWh)	Avg CF	Ttl Energy (MWh)	Avg Prod (MWh)	Avg CF	Ttl Energy (MWh)	Increase %	
1003	2	6.70	3641.7	0.3372	24 412.5	3651.1	0.3381	24 475.6	0.3	
1005	1	1.85	9401.4	0.8705	17 432.1	9615.7	0.8903	17 829.4	2.3	
1010	2	4.99	3472.1	0.3215	17 332.9	3602.7	0.3336	17 985.1	3.8	
1011	1	4.28	3604.3	0.3337	15 422.7	3657.6	0.3387	15 650.6	1.5	
1013	4	10.55	2463.4	0.2281	26 000.8	2536.6	0.2349	26 772.7	3.0	
1014	1	1.85	4846.6	0.4488	8986.6	4930.5	0.4565	9142.1	1.7	
1016	1	2.85	1134.0	0.1050	3234.8	1172.4	0.1086	3344.3	3.4	
1017	1	2.71	10 989.9	1.0176	29 782.5	10 992.0	1.0178	29 788.1	0.0	
1031	5	14.98	8150.5	0.7547	122 063.8	8236.7	0.7627	123 354.8	1.1	
1032	5	14.41	7134.1	0.6606	102 772.0	7202.7	0.6669	103 760.3	1.0	
1033	4	10.55	4686.5	0.4339	49 464.1	4782.9	0.4429	50 481.9	2.1	
1034	3	8.42	9304.2	0.8615	78 296.8	9425.0	0.8727	79 313.6	1.3	
1035	2	5.85	3400.2	0.3148	19 883.7	3474.5	0.3217	20 318.3	2.2	
Season	32	90.00	5748.1	0.5322	515 085.3	5830.5	0.5399	522 216.9		
Increase						82.4	0.0076	7131.7	1.4	

Table 5.12: Summary of the calculated energy production for the entire summer season based on the synoptic type distribution.

Type	Cases	Days	RECT				CUST				Increase %
			Avg Prod (MWh)	Avg CF	Ttl Energy (MWh)	Avg Prod (MWh)	Avg CF	Ttl Energy (MWh)	Avg Prod (MWh)	Avg CF	
3002	1	3.57	1781.8	0.1650	6363.5	1805.6	0.1672	6448.5	1.3		
3004	0	0.00	0.0	0.0000	0.0	0.0	0.0000	0.0	0.0		
3007	1	0.86	1706.8	0.1580	1463.0	1750.7	0.1621	1500.6	2.6		
3011	1	3.86	1007.2	0.0933	3884.7	1048.7	0.0971	4045.1	4.1		
3031	6	18.57	2342.3	0.2169	43500.5	2400.8	0.2223	44587.1	2.5		
3032	10	29.71	4281.2	0.3964	127212.7	4363.5	0.4040	129657.7	1.9		
3033	5	15.71	2491.7	0.2307	39155.0	2573.1	0.2383	40435.2	3.3		
3034	2	4.14	1599.3	0.1481	6625.7	1667.2	0.1544	6907.0	4.2		
3035	4	13.00	1233.7	0.1142	16038.6	1276.0	0.1181	16588.1	3.4		
3036	1	2.57	4786.8	0.4432	12308.8	4902.8	0.4540	12607.1	2.4		
Season	31	92.00	2798.1	0.2591	256552.4	2866.2	0.2654	262776.4			
Increase						68.1	0.0063	6224.0	2.4		

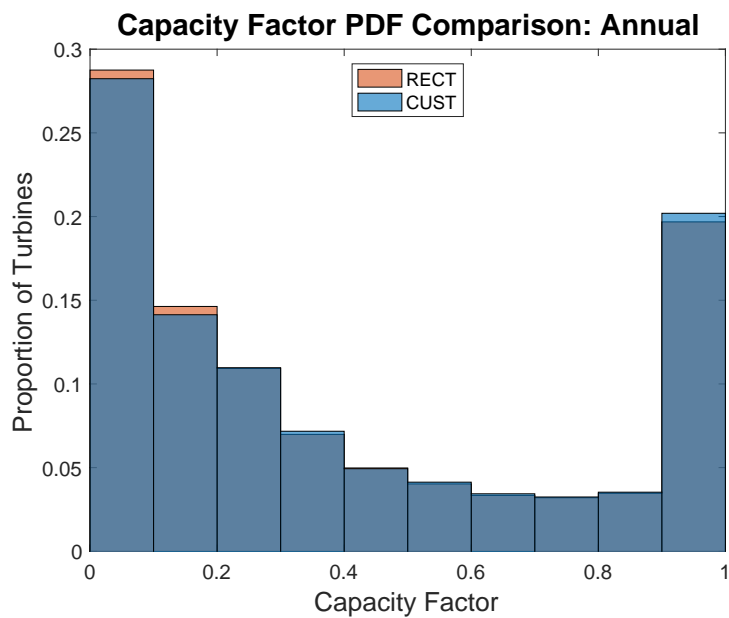


Figure 5.15: Probability distribution of capacity factors for each individual turbine at all model timesteps for all of the case studies modeled. Note the gray-blue colored areas are where the blue and red bars overlap.

CUST layout, the scatterplot in Figure 5.16 compares the performance of the entire wind farm at all times within all of the runs between RECT and CUST. There is a larger number of points located above the 1:1 ratio line, indicating the improved performance achieved by the CUST farm.

5.4 Summary and Conclusions

This regional modeling study went beyond the initial wind farm modeling conducted in Chapter 3 by using WRF to model wind farms under actual meteorological conditions. These conditions were case studies selected to capture the variability of synoptic conditions seen in the Delaware region. The results of those model runs were used to estimate seasonal and annual power production from the two primary wind farm layouts by weighting the results according to the prevalence of each synoptic type. These results showed that the custom wind farm layout outperformed the rectangular farm in every synoptic condition, and all but one of the case studies. Overall, the custom wind farm produced an additional 1.4% of energy in the winter season, and

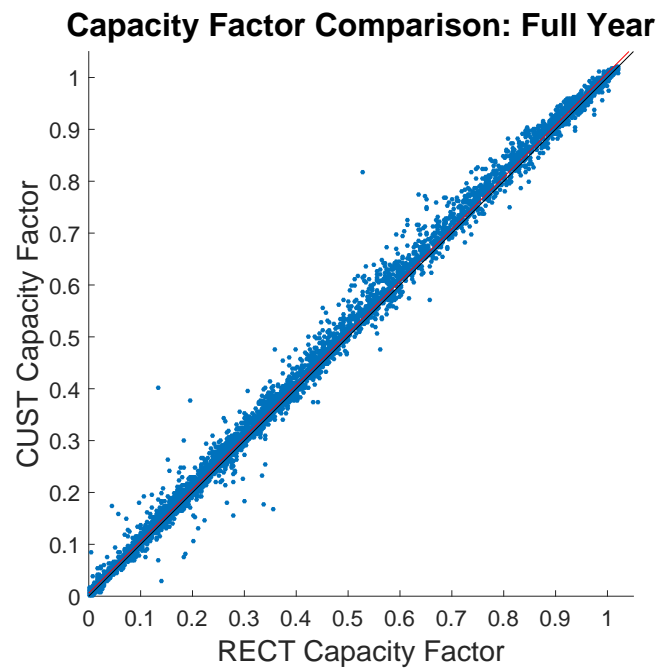


Figure 5.16: Comparison between total farm capacity factor for RECT and CUST at every time interval for all case studies run. The black line depicts the 1:1 ratio line, where the CF of the two farms is equal; the red line is the least-squares regression line of the data points.

2.4% in the summer months. This indicates that careful consideration of wind farm layout based on the local climatology can be beneficial to the overall energy production, particularly in the demanding summer months. Large-eddy simulations (LES) of these wind farms would provide more accurate wake effects, but at a high computational cost. Using limited LES runs to evaluate the optimal wind farm for specific conditions could be combined with the WRF mesoscale modeling to provide a broader, more thorough assessment than either technique alone.

The technique outlined in this chapter for evaluating wind farm performance is a powerful tool. The described method allows for evaluating the possible energy production of the proposed wind farm under realistic meteorological conditions, using a well-established and trusted mesoscale model. The technique is scalable: a large number of case studies can be used if more rigor and variability were desired, or fewer in a region with less synoptic variability than coastal Delaware. The methods are also easily accessible, using all public data and tools if necessary, although proprietary information can be used if desired. With refinement to suit the situation, and a knowledgeable scientist controlling the experiments, these methods are beneficial to the wind industry.

Chapter 6

DISCUSSION AND CONCLUSIONS

Offshore wind is beginning to make significant inroads in the United States, with the completion of the Block Island Wind Farm in Rhode Island expected to be operational by the end of 2016. The ongoing development of other offshore wind leasing areas makes now a very important time to conduct research that will benefit an industry just getting started in the United States. This dissertation seeks to advance knowledge surrounding both the development and operation of offshore wind, most specifically in the Delaware Wind Energy Area (WEA), although the methods described are applicable anywhere. The research questions addressed in the preceding pages fit into two broad areas explored using the Weather Research and Forecasting (WRF) mesoscale model: improved modeling of offshore wind farm geometries in order to improve resource assessment; and managing wind ramp forecasting error and improving wind energy reliability to maintain grid stability. The discussion on these areas is followed by a brief description of future work and focus areas of study.

6.1 Resource Assessment Improvements

Accurate and thorough wind resource assessments are vital in the successful deployment of offshore wind. They rely on not only as many high quality observations as are available, but also efficient and trustworthy modeling in order to have a complete picture of the levels of power a potential wind farm site is expected to produce. Resource assessments for the offshore region are particularly challenging, as observations can be sparse and expensive to obtain, which makes good modeling using the available observations essential. It is important for these models to take into consideration the variety of meteorological conditions present at the site, which includes a thorough

understanding of the wind climatology, and the possible ways the farm itself might influence the wind dynamics through their turbulent wakes.

The study discussed in Chapter 3 focused on utilizing an idealized WRF model and domain in order to evaluate the impact wind farm array geometry has on the wake effects produced, and thereby, the power extracted by the farm. Not surprisingly, given other research using large-eddy simulations (Archer et al., 2013), one layout factor which showed promise is the concept of staggering; wind turbines in subsequent rows should not be placed directly behind each other in the predominant wind directions. A second factor is the overall shape: having a triangular point in the predominant wind direction also improved overall performance, due to the increased number of turbines in the “front row” relative to the wind.

The challenge to implementing these ideas is that the Delaware WEA is in a complicated wind regime, and has three predominant wind directions. Optimizing power production in one direction could lead to reduced power in another important direction. This dissertation sought to create a customized wind farm array, intended to capitalize on the unique wind climatology of the Delaware WEA. This custom shape was initially modeled and compared to a conventional rectangular array in the idealized WRF domain, with model runs conducted for 324 different wind velocity bins of speed and direction. These results were then used to assess climatologically expected annual power, based on the probability distribution of the winds. Overall, the custom-shaped array delivered an additional 36 000 MWh over the rectangular array in a climatologically average year, an improvement of 2.2%.

The idealized study was limited to a stable atmosphere, and employed a simplified WRF domain. The regional study described in Chapter 5 went beyond, and selected 63 case study dates to model using a regional, real-world WRF domain. The selection of case studies made careful consideration of the variety of synoptic conditions found in the Delaware coastal region (Hughes and Veron, 2015; Siegert et al., 2016). In addition to the rectangular and custom-shaped arrays, several additional wind farm layouts were modeled, in order to assess some of the factors that cause the

custom shape to outperform the rectangle in all but one of the case study dates. Both staggering of wind turbines and the rotation of the farm played a role on the power production of the wind farms. Overall, the custom shaped layout outperformed the rectangle by 1.4% for the winter case studies, and 2.4% for the summer case studies, which is very similar to the results in Chapter 3.

The reduction in wind turbine performance which results from wakes propagating through the farm is more linear than that typically observed in studies such as Barthelmie et al. (2010). WRF has some limitations in its ability to model wind turbine wakes, due to the scales at which wakes occur. The Fitch et al. (2012) wind farm parameterization within WRF simulates each turbine as a drag sink within the grid cells, and does not explicitly model the turbine or its blade rotation, which underestimates the near-downwind wake impacts. Additionally, WRF is a mesoscale model, and therefore does not operate at the fine resolution of a large-eddy simulation, and is unable to accurately replicate the dynamics in the near wake. However, the results are sufficient enough to indicate that there is value to customizing a wind farm layout to best suit the climatology of a site location. Combining the two methods could provide great benefit to wind resource assessments.

6.2 Forecasting Improvements

Wind ramp events are a meteorological phenomenon characterized by a large and rapid change in wind speed, and present unique forecasting challenges, particularly in the wind energy industry. Chapter 4 focused on understanding how ramp events at the Delaware WEA would potentially impact a wind farm at the site, taking into consideration the effects the variable power might have on electrical grid operations. WRF was used to model 24 case study dates which featured prominent ramp events using three different commonly available forcing datasets, mirroring how an operational forecaster may predict power production at an operating wind farm. While no one forcing dataset outperformed the others, the comparison served to illustrate the challenges of ramp forecasting, as the model error in predicting the events varied tremendously.

The model's error in predicting the timing was found to be more impactful on grid operations than errors in ramp magnitude or shape. Most significantly, the potential grid impacts resulting from a ramp misprediction was a function of not just the error itself, but the overall electrical load demand, and how that demand was changing at the time of the event. Predicting the ramp event to occur at a different time when load demand is rapidly increasing could result in more negative consequences in the grid than if it were to occur at a time when load was stable or decreasing. While improving the grid's ability to respond better to the variability inherent in wind power through increased backup power generation is one way to reduce the grid impacts, making improvements in the wind predictions themselves is likely to be less costly (Marquis et al., 2011). To that end, these results show that forecasting improvements would be most beneficial in the morning hours throughout the year, and the early evening during the winter months.

6.3 Future Work

The research conducted within this dissertation leaves several exciting avenues for future work. While the case studies modeled in the regional study in Chapter 5 included cases that featured ramp events, these were not explicitly examined for their possible grid implications. Performing additional model runs of ramp events for evaluation using the methods outlined in Chapter 4, but including a wind farm within the domain, could bring some interesting results that further evaluate the potential grid implications for poor ramp predictions. It would also be important to take consideration of the short-term power bidding requirements, which allow electricity operators to slightly adjust their bids closer to real-time, as opposed to relying on the day before modeling used in this study.

All three of the studies discussed focused on a hypothetical wind farm constructed within the Delaware WEA. However, due to the fact that a farm is not yet located here, it is difficult to evaluate the accuracy of these results by comparing them to observations. A study applying the regional modeling techniques developed

in Chapter 5 for an already existing wind farm would provide an exciting opportunity to evaluate how well the model performs when compared to the observations at the existing farm. Additionally, it could allow for an assessment of how the farm might have seen better results with a different wind farm layout while using the efficient mesoscale WRF model. This idea could be further explored by comparing the results with those from a large-eddy simulation in order to evaluate the results obtained using a high-resolution model compared to a coarser resolution, but more computationally efficient, model.

6.4 Final Remarks

In summary, this dissertation sought to answer several main research questions, outlined in Chapter 1. The first goal was to address whether wind farm array layouts influence wind farm productivity, and which of those design considerations lead to the most significant improvement in productivity. It was found that unsurprisingly, the array configuration does influence the farm's productivity, even when using a mesoscale model such as WRF. Specifically, the staggering of wind turbines in the predominant wind directions, and including more front row turbines through the correct orientation emerged as significant design considerations. This knowledge was used to address the next goal, which was an improved examination of the wind energy resource in the Delaware Wind Energy Area, taking these design considerations into account. Finally, meteorological forecasting uncertainty and its impacts on grid operations were examined, specifically for wind ramp events. It was found that improvements in forecasting accuracy in the morning and evening hours would prove most beneficial to the wind energy industry. Combined, these results can help guide the future of wind energy in society's ongoing quest to combat climate change through renewable energy generation, and moves the wind energy industry closer to the goal of seeing offshore wind throughout the United States.

REFERENCES

- Ainslie, J. F., 1988: Calculating the flowfield in the wake of wind turbines. *Journal of Wind Engineering and Industrial Aerodynamics*, **27** (1–3), 213–224, doi:10.1016/0167-6105(88)90037-2.
- Archer, C. L., and M. Z. Jacobson, 2003: Spatial and temporal distributions of US winds and wind power at 80 m derived from measurements. *Journal of Geophysical Research*, **108** (D9), doi:10.1029/2002JD002076.
- Archer, C. L., and M. Z. Jacobson, 2005: Evaluation of global wind power. *Journal of Geophysical Research*, **110** (D12), doi:10.1029/2004JD005462.
- Archer, C. L., and M. Z. Jacobson, 2013: Geographical and seasonal variability of the global “practical” wind resources. *Applied Geography*, **45** (0), 119–130, doi:10.1016/j.apgeog.2013.07.006.
- Archer, C. L., S. Mirzaeisefat, and S. Lee, 2013: Quantifying the sensitivity of wind farm performance to array layout options using large-eddy simulation. *Geophysical Research Letters*, **40** (18), 4963–4970, doi:10.1002/grl.50911.
- Archer, C. L., B. A. Colle, L. D. Monache, M. J. Dvorak, J. Lundquist, B. H. Bailey, P. Beaucage, M. J. Churchfield, A. C. Fitch, B. Kosovic, S. Lee, P. J. Moriarty, H. Simao, R. J. A. M. Stevens, D. Veron, and J. Zack, 2014: Meteorology for coastal/offshore wind energy in the United States: Recommendations and research needs for the next 10 years. *Bulletin of the American Meteorological Society*, **95** (4), 515 – 519, doi:10.1175/BAMS-D-13-00108.1.
- Barthelmie, R., G. Larsen, S. Pryor, H. Jørgensen, H. Bergström, W. Schlez, K. Rados, B. Lange, P. Vølund, S. Neckelmann, S. Mogensen, G. Schepers, T. Hegberg, L. Folkerts, and M. Magnusson, 2004: ENDOW (Efficient Development of Offshore Wind Farms): Modelling wake and boundary layer interactions. *Wind Energy*, **7** (3), 225–245, doi:10.1002/we.121.
- Barthelmie, R. J., L. Folkerts, G. C. Larsen, K. Rados, S. C. Pryor, S. T. Frandsen, B. Lange, and G. Schepers, 2006: Comparison of wake model simulations with offshore wind turbine wake profiles measured by sodar. *Journal of Atmospheric and Oceanic Technology*, **23** (7), 888–901, doi:10.1175/JTECH1886.1.

- Barthelmie, R. J., K. Hansen, S. T. Frandsen, O. Rathmann, J. G. Schepers, W. Schlez, J. Phillips, K. Rados, A. Zervos, E. S. Politis, and P. K. Chaviaropoulos, 2009: Modelling and measuring flow and wind turbine wakes in large wind farms offshore. *Wind Energy*, **12** (5), 431–444, doi:10.1002/we.348.
- Barthelmie, R. J., S. C. Pryor, S. T. Frandsen, K. S. Hansen, J. G. Schepers, K. Rados, W. Schlez, A. Neubert, L. E. Jensen, and S. Neckelmann, 2010: Quantifying the impact of wind turbine wakes on power output at offshore wind farms. *Journal of Atmospheric and Oceanic Technology*, **27** (8), 1302–1317, doi:10.1175/2010JTECHA1398.1.
- Black, T. L., 1994: The new NMC mesoscale Eta model: Description and forecast examples. *Weather and Forecasting*, **9** (2), 265–278, doi:10.1175/1520-0434(1994)009<0265:TNNMEM>2.0.CO;2.
- Breton, S.-P., and G. Moe, 2009: Status, plans and technologies for offshore wind turbines in Europe and North America. *Renewable Energy*, **34** (3), 646–654, doi:10.1016/j.renene.2008.05.040.
- Bureau of Ocean Energy Management, 2013: Commercial wind lease issuance on the Atlantic outer continental shelf offshore Delaware. *Federal Register*, **78** (13), 4167.
- Bureau of Ocean Energy Management, 2015: Delaware activities. URL <http://www.boem.gov/Delaware/>, accessed 12/2/2015.
- Carvalho, D., A. Rocha, M. Gomez-Gesteira, and C. Santos, 2012: A sensitivity study of the WRF model in wind simulation for an area of high wind energy. *Environmental Modelling & Software*, **33**, 23–34, doi:10.1016/j.envsoft.2012.01.019.
- Chen, F., and J. Dudhia, 2001: Coupling an advanced land surface–hydrology model with the Penn State–NCAR MM5 modeling system. Part I: Model implementation and sensitivity. *Monthly Weather Review*, **129** (4), 569–585, doi:10.1175/1520-0493(2001)129<0569:CAALSH>2.0.CO;2.
- Cheng, W. Y., Y. Liu, Y. Liu, Y. Zhang, W. P. Mahoney, and T. T. Warner, 2013: The impact of model physics on numerical wind forecasts. *Renewable Energy*, **55**, 347 – 356, doi:10.1016/j.renene.2012.12.041.
- Cochran, J., M. Miller, O. Zinaman, M. Milligan, D. Arent, B. Palmintier, M. O’Malley, S. Mueller, E. Lannoye, A. Tuohy, B. Kujala, M. Sommer, H. Holttinen, J. Kiviluoma, and S. K. Soonee, 2014: Flexibility in 21st Century Power Systems. Technical Paper NREL/TP-6A20-61721, National Renewable Energy Laboratory, Golden, CO.
- Davis, N., A. N. Hahmann, N.-E. Clausen, and M. Žagar, 2013: Forecast of icing events at a wind farm in Sweden. *Journal of Applied Meteorology and Climatology*, **53** (2), 262–281, doi:10.1175/JAMC-D-13-09.1.

- Deepwater Wind, 2016: Block Island Wind Farm. URL <http://dwwind.com/project/block-island-wind-farm/>.
- Dhanju, A., P. Whitaker, and W. Kempton, 2008: Assessing offshore wind resources: An accessible methodology. *Renewable Energy*, **33** (1), 55–64, doi:10.1016/j.renene.2007.03.006.
- Dowtin, A. L., 2012: Developing a drought climatology for Delaware (1948–2005). M.S. thesis, Department of Geography, University of Delaware, Newark, DE.
- Dudhia, J., 1989: Numerical study of convection observed during the winter monsoon experiment using a mesoscale two-dimensional model. *Journal of the Atmospheric Sciences*, **46** (20), 3077–3107, doi:10.1175/1520-0469(1989)046<3077:NSOCOD>2.0.CO;2.
- Dvorak, M. J., B. A. Corcoran, J. E. Ten Hoeve, N. G. McIntyre, and M. Z. Jacobson, 2012: US East Coast offshore wind energy resources and their relationship to peak-time electricity demand. *Wind Energy*, **16** (7), 977–997, doi:10.1002/we.1524.
- Firestone, J., 2008: Summary of Bluewater Wind Power Purchase Agreement, <http://www.ceoe.udel.edu/windpower/deproject.html>, accessed 5/2/2012.
- Firestone, J., C. L. Archer, M. P. Gardner, J. A. Madsen, A. K. Prasad, and D. E. Veron, 2015: Opinion: The time has come for offshore wind power in the United States. *Proceedings of the National Academy of Sciences*, **112** (39), 11 985–11 988, doi:10.1073/pnas.1515376112.
- Firestone, J., and W. Kempton, 2007: Public opinion about large offshore wind power: Underlying factors. *Energy Policy*, **35** (3), 1584–1598, doi:http://dx.doi.org/10.1016/j.enpol.2006.04.010.
- Fitch, A. C., 2015: Notes on using the mesoscale wind farm parameterization of Fitch et al. (2012) in WRF. *Wind Energy*, doi:10.1002/we.1945.
- Fitch, A. C., J. B. Olson, and J. K. Lundquist, 2013a: Parameterization of wind farms in climate models. *Journal of Climate*, **26** (17), 6439–6458, doi:10.1175/JCLI-D-12-00376.1.
- Fitch, A. C., J. B. Olson, J. K. Lundquist, J. Dudhia, A. K. Gupta, J. Michalakes, and I. Barstad, 2012: Local and mesoscale impacts of wind farms as parameterized in a mesoscale NWP model. *Monthly Weather Review*, **140** (9), 3017–3038, doi:10.1175/MWR-D-11-00352.1.
- Fitch, A. C., J. B. Olson, J. K. Lundquist, J. Dudhia, A. K. Gupta, J. Michalakes, I. Barstad, and C. L. Archer, 2013b: Corrigendum. *Monthly Weather Review*, **141** (4), 1395–1395, doi:10.1175/MWR-D-12-00341.1.

- Garvine, R. W., and W. Kempton, 2008: Assessing the wind field over the continental shelf as a resource for electric power. *Journal of Marine Research*, **66** (6), 751–773.
- Gilliland, E. K., and C. M. Rowe, 2007: A comparison of cumulus parameterization schemes in the WRF model. *Proceedings of the 87th AMS Annual Meeting & 21st Conference on Hydrology*, 2–16.
- Greaves, B., J. Collins, J. Parkes, and A. Tindal, 2009: Temporal forecast uncertainty for ramp events. *Proceedings of the European Wind Energy Conference and Exhibition (EWEC)*, Marseille, France.
- Hughes, C. P., and D. E. Veron, 2015: Characterization of low-level winds of southern and coastal Delaware. *Journal of Applied Meteorology and Climatology*, **54** (1), 77–93, doi:10.1175/JAMC-D-14-0011.1.
- Janjić, Z. I., 1994: The step-mountain Eta coordinate model: Further developments of the convection, viscous sublayer, and turbulence closure schemes. *Monthly Weather Review*, **122** (5), 927–945, doi:10.1175/1520-0493(1994)122<0927:TSMECM>2.0.CO;2.
- Kalkstein, L. S., and P. Corrigan, 1986: A synoptic climatological approach for geographical analysis: Assessment of sulfur dioxide concentrations. *Annals of the Association of American Geographers*, **76** (3), 381–395.
- Kamath, C., 2010: Understanding wind ramp events through analysis of historical data. *Transmission and Distribution Conference and Exposition*, IEEE Power & Energy Society, 1–6.
- Kanamitsu, M., 1989: Description of the NMC global data assimilation and forecast system. *Weather and Forecasting*, **4** (3), 335–342, doi:10.1175/1520-0434(1989)004<0335:DOTNGD>2.0.CO;2.
- Kanamitsu, M., J. C. Alpert, K. A. Campana, P. M. Caplan, D. G. Deaven, M. Iredell, B. Katz, H. L. Pan, J. Sela, and G. H. White, 1991: Recent changes implemented into the Global Forecast System at NMC. *Weather and Forecasting*, **6** (3), 425–435, doi:10.1175/1520-0434(1991)006<0425:RCITG>2.0.CO;2.
- Katic, I., J. Højstrup, and N. O. Jensen, 1986: A simple model for cluster efficiency. *Proceedings of the European Wind Energy Conference and Exhibition (EWEC)*, Rome, Italy, European Wind Energy Association, Vol. 1, 407–410.
- Kempton, W., C. L. Archer, A. Dhanju, R. W. Garvine, and M. Z. Jacobson, 2007: Large CO₂ reductions via offshore wind power matched to inherent storage in energy end-uses. *Geophysical Research Letters*, **34** (2), doi:10.1029/2006GL028016.

- Kempton, W., F. M. Pimenta, D. E. Veron, and B. A. Colle, 2010: Electric power from offshore wind via synoptic-scale interconnection. *Proceedings of the National Academy of Sciences*, **107** (16), 7240–7245, doi:10.1073/pnas.0909075107.
- Lackner, M. A., A. L. Rogers, J. F. Manwell, and J. G. McGowan, 2010: A new method for improved hub height mean wind speed estimates using short-term hub height data. *Renewable Energy*, **35** (10), 2340–2347, doi:10.1016/j.renene.2010.03.031.
- Lamb, H. H., 1972: British Isles weather types and a register of daily sequence of circulation patterns, 1861–1971. *Geophysical Memoir 116*, HMSO, London, 85pp.
- Lund, I. A., 1963: Map-pattern classification by statistical methods. *Journal of Applied Meteorology*, **2** (1), 56–65, doi:10.1175/1520-0450(1963)002<0056:MPCBSM>2.0.CO;2.
- Madariaga, A., I. M. de Alegria, J. Martn, P. Egua, and S. Ceballos, 2012: Current facts about offshore wind farms. *Renewable and Sustainable Energy Reviews*, **16** (5), 3105 – 3116, doi:10.1016/j.rser.2012.02.022.
- Manwell, J. F., C. N. Elkinton, A. L. Rogers, and J. G. McGowan, 2007: Review of design conditions applicable to offshore wind energy systems in the United States. *Renewable Sustainable Energy Reviews*, **11** (2), 210–234, doi:10.1016/j.rser.2005.01.002.
- Manwell, J. F., J. G. McGowan, and A. L. Rogers, 2010: *Wind Power Explained: Theory, Design, and Application*. 2nd ed., Wiley, West Sussex, UK.
- Marquis, M., J. Wilczak, M. Ahlstrom, J. Sharp, A. Stern, J. C. Smith, and S. Calvert, 2011: Forecasting the wind to reach significant penetration levels of wind energy. *Bulletin of the American Meteorological Society*, **92** (9), 1159–1171, doi:10.1175/2011BAMS3033.1.
- McClatchey, R. A., R. W. Fenn, J. E. A. Selby, F. E. Volz, and J. S. Garing, 1972: *Optical Properties of the Atmosphere*. 3rd ed., No. 411, Environmental Research Papers, United States Air Force, Air Force Systems Command, Air Force Cambridge Research Laboratories, Optical Physics Laboratory, Bedford, Massachusetts.
- Mesinger, F., G. DiMego, E. Kalnay, K. Mitchell, P. C. Shafran, W. Ebisuzaki, D. Jović, J. Woollen, E. Rogers, E. H. Berbery, M. B. Ek, Y. Fan, R. Grumbine, W. Higgins, H. Li, Y. Lin, G. Manikin, D. Parrish, and W. Shi, 2006: North American Regional Reanalysis. *Bulletin of the American Meteorological Society*, **87** (3), 343–360, doi:10.1175/BAMS-87-3-343.
- Mlawer, E. J., S. J. Taubman, P. D. Brown, M. J. Iacono, and S. A. Clough, 1997: Radiative transfer for inhomogeneous atmospheres: Rrtm, a validated correlated-k model for the longwave. *Journal of Geophysical Research*, **102** (D14), 16 663–16 682, doi:10.1029/97JD00237.

- Monitoring Analytics, 2015: 2014 State of the Market Report for PJM. Annual report, Monitoring Analytics, LLC. URL http://www.monitoringanalytics.com/reports/PJM_State_of_the_Market/2014.shtml, retrieved 6/2/2016.
- Monitoring Analytics, 2016: 2015 State of the Market Report for PJM. Annual report, Monitoring Analytics, LLC. URL http://www.monitoringanalytics.com/reports/PJM_State_of_the_Market/2015.shtml, retrieved 6/2/2016.
- Musial, W., and S. Butterfield, 2004: Future for offshore wind energy in the United States. *EnergyOcean 2004*, Palm Beach, FL, NREL/CP-500-36313.
- Musial, W., and B. Ram, 2010: Large-scale offshore wind power in the United States: Assessment of opportunities and barriers. Technical Report NREL/TP-500-40745, National Renewable Energy Laboratory, Golden, CO.
- Nakanishi, M., and H. Niino, 2006: An improved Mellor–Yamada level-3 model: Its numerical stability and application to a regional prediction of advection fog. *Boundary-Layer Meteorology*, **119** (2), 397–407, doi:10.1007/s10546-005-9030-8.
- National Centers for Environmental Information, 2016a: Global Forecast System (GFS). URL <https://www.ncdc.noaa.gov/data-access/model-data/model-datasets/global-forecast-system-gfs>.
- National Centers for Environmental Information, 2016b: North American Mesoscale Forecast System (NAM). URL <https://www.ncdc.noaa.gov/data-access/model-data/model-datasets/north-american-mesoscale-forecast-system-nam>.
- National Oceanic and Atmospheric Administration, 2016: National Data Buoy Center. URL <http://www.ndbc.noaa.gov/>.
- NCAR, 2012: *ARW Version 3 Modeling System User’s Guide*. Boulder, Colorado, USA, Mesoscale and Microscale Meteorology Division, National Center for Atmospheric Research.
- Noel, L., J. F. Brodie, W. Kempton, C. L. Archer, and C. Budischak, 2016: Cost minimization of generation, storage, and new loads, comparing costs with and without externalities. *Nature Energy*, submitted.
- NRG Bluewater Wind, 2012: NRG Bluewater Wind – Delaware. URL <http://www.bluewaterwind.com/delaware.htm>, accessed 5/2/2012.
- PJM, 2016a: About PJM. URL <http://www.pjm.com/about-pjm.aspx>, accessed 5/23/2016.
- PJM, 2016b: PJM 101: The Basics. URL <http://pjm.com/Globals/Training/Courses/ol-pjm-101.aspx>, accessed 6/2/2016.

- PJM, 2016c: *PJM Manual 11: Energy & Ancillary Services Market Operations*. PJM, URL <http://www.pjm.com/documents/~media/documents/manuals/m11.ashx>.
- Pryor, S. C., and R. J. Barthelmie, 2002: Statistical analysis of flow characteristics in the coastal zone. *Journal of Wind Engineering and Industrial Aerodynamics*, **90** (3), 201–221, doi:10.1016/S0167-6105(01)00195-7.
- Rathmann, O., R. J. Barthelmie, and S. T. Frandsen, 2006: Turbine wake model for wind resource software. *Proceedings of the European Wind Energy Conference and Exhibition (EWEC)*, Athens, Greece, European Wind Energy Association, BL3.313.
- REpower Systems AG, 2010: Power curve, power and thrust coefficients: REpower 5M with LM61.5P2 Evolution B. Document SD-5.1-WT.PC.02-B-C-EN, Hamburg, Germany.
- REpower Systems AG, 2011: REpower 5M. Product Brochure, Hamburg, Germany.
- Rutledge, G. K., J. Alpert, and W. Ebisuzaki, 2006: NOMADS: A climate and weather model archive at the National Oceanic and Atmospheric Administration. *Bulletin of the American Meteorological Society*, **87** (3), 327–341, doi:10.1175/BAMS-87-3-327.
- Schlez, W., and A. Neubert, 2009: New developments in large wind farm modelling. *Proceedings of the European Wind Energy Conference and Exhibition (EWEC)*, Marseille, France, European Wind Energy Association, PO.167.
- Schwartz, M., D. Heimiller, S. Haymes, and W. Musial, 2010: Assessment of offshore wind energy resources for the United States. Technical Report NREL/TP-500-45889, National Renewable Energy Laboratory, Golden, CO.
- Sevlian, R., and R. Rajagopal, 2013: Detection and statistics of wind power ramps. *IEEE Transactions on Power Systems*, **4**, 3610–3620.
- Siegert, C. M., D. J. Leathers, and D. F. Levia, 2016: Synoptic typing: interdisciplinary application methods with three practical hydroclimatological examples. *Theoretical and Applied Climatology*, 1–19, doi:10.1007/s00704-015-1700-y.
- Skamarock, W. C., J. B. Klemp, J. Dudhia, D. O. Gill, D. M. Barker, M. G. Duda, X.-Y. Huang, W. Wang, and J. G. Powers, 2008: A description of the Advanced Research WRF version 3. NCAR Technical Report NCAR/TN-475+STR, Mesoscale and Microscale Meteorology Division, National Center for Atmospheric Research, Boulder, Colorado, USA.
- Steel, W., 2015: Siemens looks toward next-generation 10–20 MW wind turbines. URL <http://cleantechnica.com/2015/09/15/siemens-looks-toward-next-generation-10-20-mw-wind-turbines/>.

- Stull, R. B., 1988: *An Introduction to Boundary Layer Meteorology*. Kluwer Academic Publishers, Dordrecht, The Netherlands.
- Thompson, G., P. R. Field, R. M. Rasmussen, and W. D. Hall, 2008: Explicit forecasts of winter precipitation using an improved bulk microphysics scheme. Part II: Implementation of a new snow parameterization. *Monthly Weather Review*, **136** (12), 5095–5115, doi:10.1175/2008MWR2387.1.
- University of Delaware, 2012: *UD Community Cluster Program Mills User Guide*. Newark, Delaware, University of Delaware Information Technologies.
- U.S. Energy Information Administration, 2016a: Frequently asked questions. URL <https://www.eia.gov/tools/faqs/>, accessed 6/19/2016.
- U.S. Energy Information Administration, 2016b: International Energy Outlook 2016. Report DOE/EIA-0484(2016), U.S. Department of Energy, Washington, DC.
- van Wijk, A. J. M., A. C. M. Beljaars, A. A. M. Holtslag, and W. C. Turkenburg, 1990: Evaluation of stability corrections in wind speed profiles over the North Sea. *Journal of Wind Engineering and Industrial Aerodynamics*, **33** (3), 551–566, doi:10.1016/0167-6105(90)90007-Y.
- Vanderwende, B., and J. K. Lundquist, 2015: Could crop height affect the wind resource at agriculturally productive wind farm sites? *Boundary-Layer Meteorology*, 1–20, doi:10.1007/s10546-015-0102-0.
- Vanderwende, B. J., J. K. Lundquist, M. E. Rhodes, E. S. Takle, and S. L. Irvin, 2015: Observing and simulating the summertime low-level jet in central Iowa. *Monthly Weather Review*, **143** (6), 2319–2336, doi:10.1175/MWR-D-14-00325.1.
- Veron, D. E., J. F. Brodie, Y. A. Shirazi, and J. R. Gilchrist, 2016: Characterizing the impact of wind ramp forecasting error in the offshore Mid-Atlantic region. *Journal of Renewable and Sustainable Energy*, in final preparation.
- Vestas Wind Systems A/S, 2011: V164 8.0 MW. Product Brochure, Aarhus, Denmark.
- Wang, W., and N. L. Seaman, 1997: A comparison study of convective parameterization schemes in a mesoscale model. *Monthly Weather Review*, **125** (2), 252–278, doi:10.1175/1520-0493(1997)125<0252:ACSOCP>2.0.CO;2.
- Wilczak, J., C. Finley, J. Freedman, J. Cline, L. Bianco, J. Olson, I. Djalalova, L. Sheridan, M. Ahlstrom, J. Manobianco, J. Zack, J. R. Carley, S. Benjamin, R. Coulter, L. K. Berg, J. Mirocha, K. Clawson, and M. Marquis, 2015: The Wind Forecast Improvement Project (WFIP): A public-private partnership addressing wind energy forecast needs. *Bulletin of the American Meteorological Society*, **96** (10), 1699–1718, doi:10.1175/BAMS-D-14-00107.1.

Wu, Y.-T., and F. Porté-Agel, 2011: Large-eddy simulation of wind-turbine wakes: Evaluation of turbine parametrisations. *Boundary-Layer Meteorology*, **138** (3), 345–366, doi:10.1007/s10546-010-9569-x.

Yarnal, B., 1993: *Synoptic Climatology in Environmental Analysis: A Primer*. Belhaven Press, London.

Appendix A

WIND TURBINE LOCATION FILES

This appendix includes the location files (`windturbines.txt`) of each of the wind farms used in the regional study described in Chapter 5. The first column shows latitude; the second column is longitude; the third column is the wind turbine type, which tells WRF which `wind-turbine-*.tbl` file to find the input parameters for the turbine design used (in this case, `* = 1`).

A.1 Rectangle (RECT)

```
38.725620 -74.613462 1
38.725667 -74.627957 1
38.725712 -74.642452 1
38.725756 -74.656947 1
38.725797 -74.671442 1
38.725837 -74.685937 1
38.725875 -74.700432 1
38.725911 -74.714927 1
38.725946 -74.729422 1
38.725978 -74.743917 1
38.714265 -74.613523 1
38.714312 -74.628016 1
38.714357 -74.642508 1
38.714401 -74.657001 1
38.714442 -74.671494 1
38.714482 -74.685986 1
38.714520 -74.700479 1
38.714557 -74.714972 1
38.714591 -74.729465 1
38.714624 -74.743958 1
38.702911 -74.613584 1
38.702958 -74.628074 1
38.703003 -74.642565 1
38.703046 -74.657055 1
```

38.703088 -74.671546 1
38.703128 -74.686036 1
38.703166 -74.700527 1
38.703202 -74.715017 1
38.703236 -74.729508 1
38.703269 -74.743998 1
38.691556 -74.613645 1
38.691603 -74.628133 1
38.691648 -74.642621 1
38.691692 -74.657109 1
38.691733 -74.671598 1
38.691773 -74.686086 1
38.691811 -74.700574 1
38.691847 -74.715062 1
38.691881 -74.729550 1
38.691914 -74.744039 1
38.680201 -74.613706 1
38.680248 -74.628192 1
38.680293 -74.642678 1
38.680337 -74.657164 1
38.680378 -74.671649 1
38.680418 -74.686135 1
38.680456 -74.700621 1
38.680492 -74.715107 1
38.680527 -74.729593 1
38.680559 -74.744079 1
38.668847 -74.613767 1
38.668894 -74.628251 1
38.668939 -74.642734 1
38.668982 -74.657218 1
38.669024 -74.671701 1
38.669063 -74.686185 1
38.669101 -74.700669 1
38.669137 -74.715152 1
38.669172 -74.729636 1
38.669204 -74.744120 1
38.657492 -74.613828 1
38.657539 -74.628309 1
38.657584 -74.642791 1
38.657627 -74.657272 1
38.657669 -74.671753 1
38.657709 -74.686234 1
38.657747 -74.700716 1

38.657783 -74.715197 1
38.657817 -74.729679 1
38.657850 -74.744160 1
38.646137 -74.613889 1
38.646184 -74.628368 1
38.646229 -74.642847 1
38.646272 -74.657326 1
38.646314 -74.671805 1
38.646354 -74.686284 1
38.646392 -74.700763 1
38.646428 -74.715242 1
38.646462 -74.729721 1
38.646495 -74.744200 1
38.634782 -74.613950 1
38.634829 -74.628427 1
38.634874 -74.642903 1
38.634918 -74.657380 1
38.634959 -74.671857 1
38.634999 -74.686333 1
38.635037 -74.700810 1
38.635073 -74.715287 1
38.635107 -74.729764 1
38.635140 -74.744241 1

A.2 Custom Shape (CUST)

38.725620 -74.613462 1
38.725667 -74.627957 1
38.725712 -74.642452 1
38.725756 -74.656947 1
38.725797 -74.671442 1
38.725837 -74.685937 1
38.725875 -74.700432 1
38.725911 -74.714927 1
38.725946 -74.729422 1
38.725978 -74.743917 1
38.714265 -74.613523 1
38.714312 -74.628016 1
38.714357 -74.642508 1
38.714401 -74.657001 1
38.714442 -74.671494 1
38.714482 -74.685986 1
38.714520 -74.700479 1

38.714557 -74.714972 1
38.714591 -74.729465 1
38.714624 -74.743958 1
38.702911 -74.613584 1
38.702958 -74.628074 1
38.703003 -74.642565 1
38.703046 -74.657055 1
38.703088 -74.671546 1
38.703128 -74.686036 1
38.703166 -74.700527 1
38.703202 -74.715017 1
38.703236 -74.729508 1
38.703269 -74.743998 1
38.691556 -74.613645 1
38.691603 -74.628133 1
38.691811 -74.700574 1
38.691847 -74.715062 1
38.691881 -74.729550 1
38.691914 -74.744039 1
38.680201 -74.613706 1
38.680248 -74.628192 1
38.680456 -74.700621 1
38.680492 -74.715107 1
38.680527 -74.729593 1
38.680559 -74.744079 1
38.668847 -74.613767 1
38.668894 -74.628251 1
38.669101 -74.700669 1
38.669137 -74.715152 1
38.669172 -74.729636 1
38.669204 -74.744120 1
38.657523 -74.623482 1
38.657569 -74.637964 1
38.657613 -74.652445 1
38.657734 -74.695889 1
38.657771 -74.710370 1
38.657806 -74.724851 1
38.657839 -74.739333 1
38.646199 -74.633194 1
38.646244 -74.647673 1
38.646287 -74.662152 1
38.646367 -74.691110 1
38.646404 -74.705589 1

38.646439 -74.720068 1
38.646473 -74.734548 1
38.634874 -74.642903 1
38.634918 -74.657380 1
38.634959 -74.671857 1
38.634999 -74.686333 1
38.635037 -74.700810 1
38.635073 -74.715287 1
38.635107 -74.729764 1
38.623549 -74.652609 1
38.623591 -74.667084 1
38.623631 -74.681558 1
38.623669 -74.696033 1
38.623706 -74.710507 1
38.623741 -74.724982 1
38.612222 -74.662312 1
38.612263 -74.676784 1
38.612302 -74.691256 1
38.612339 -74.705729 1
38.612375 -74.720201 1
38.600895 -74.672012 1
38.600934 -74.686482 1
38.600972 -74.700952 1
38.601008 -74.715422 1
38.589566 -74.681709 1
38.589605 -74.696176 1
38.589641 -74.710644 1
38.578237 -74.691402 1
38.578274 -74.705868 1
38.566907 -74.701093 1

A.2.1 Filled Custom Shape (FILL)

The custom shape farm with the “courtyard” replaced with 15 wind turbines include the same turbines as the CUST farm, but also include the below turbines.

38.691648 -74.642621 1
38.691692 -74.657109 1
38.691733 -74.671598 1
38.691773 -74.686086 1
38.680293 -74.642678 1
38.680337 -74.657164 1
38.680378 -74.671649 1

38.680418 -74.686135 1
38.668939 -74.642734 1
38.668982 -74.657218 1
38.669024 -74.671701 1
38.669063 -74.686185 1
38.657655 -74.666926 1
38.657696 -74.681407 1
38.646327 -74.676631 1

A.3 Rotated (ROTD)

38.725787 -74.667848 1
38.717728 -74.657637 1
38.709669 -74.647428 1
38.701609 -74.637222 1
38.693548 -74.627017 1
38.685485 -74.616815 1
38.677423 -74.606615 1
38.669359 -74.596418 1
38.661294 -74.586223 1
38.717787 -74.678134 1
38.709729 -74.667923 1
38.701670 -74.657714 1
38.693611 -74.647507 1
38.685551 -74.637303 1
38.677490 -74.627101 1
38.669427 -74.616901 1
38.661365 -74.606703 1
38.653301 -74.596508 1
38.709785 -74.688417 1
38.701729 -74.678206 1
38.693671 -74.667997 1
38.685613 -74.657790 1
38.677553 -74.647586 1
38.669493 -74.637384 1
38.661432 -74.627184 1
38.653369 -74.616986 1
38.645307 -74.606791 1
38.701783 -74.698698 1
38.693727 -74.688487 1
38.685671 -74.678278 1
38.677613 -74.668071 1
38.669554 -74.657867 1

38.661495 -74.647664 1
38.653435 -74.637465 1
38.645374 -74.627267 1
38.637312 -74.617072 1
38.693780 -74.708977 1
38.685725 -74.698765 1
38.677669 -74.688556 1
38.669613 -74.678350 1
38.661555 -74.668145 1
38.653496 -74.657943 1
38.645437 -74.647743 1
38.637377 -74.637546 1
38.629315 -74.627350 1
38.685776 -74.719253 1
38.677722 -74.709042 1
38.669667 -74.698833 1
38.661611 -74.688626 1
38.653554 -74.678421 1
38.645497 -74.668219 1
38.637438 -74.658019 1
38.629379 -74.647822 1
38.621319 -74.637626 1
38.677771 -74.729527 1
38.669718 -74.719316 1
38.661664 -74.709107 1
38.653609 -74.698900 1
38.645553 -74.688695 1
38.637496 -74.678493 1
38.629439 -74.668293 1
38.621380 -74.658096 1
38.613321 -74.647900 1
38.669765 -74.739799 1
38.661713 -74.729588 1
38.653660 -74.719378 1
38.645606 -74.709172 1
38.637551 -74.698967 1
38.629495 -74.688765 1
38.621438 -74.678565 1
38.613381 -74.668367 1
38.605322 -74.658172 1
38.661759 -74.750068 1
38.653707 -74.739857 1
38.645655 -74.729648 1

38.637602 -74.719441 1
38.629548 -74.709237 1
38.621493 -74.699034 1
38.613437 -74.688834 1
38.605380 -74.678637 1
38.597322 -74.668441 1
38.653751 -74.760336 1
38.645700 -74.750124 1
38.637649 -74.739915 1
38.629597 -74.729708 1
38.621544 -74.719504 1
38.613489 -74.709301 1
38.605434 -74.699101 1
38.597378 -74.688904 1
38.589322 -74.678708 1

A.4 Rotated - Adjusted (RADJ)

38.566907 -74.701093 1
38.576334 -74.693030 1
38.585761 -74.684965 1
38.595187 -74.676898 1
38.604612 -74.668829 1
38.614037 -74.660757 1
38.623461 -74.652684 1
38.632885 -74.644608 1
38.642308 -74.636531 1
38.651731 -74.628451 1
38.573236 -74.713102 1
38.582664 -74.705040 1
38.592091 -74.696976 1
38.601518 -74.688910 1
38.610944 -74.680841 1
38.620370 -74.672771 1
38.629795 -74.664698 1
38.639220 -74.656623 1
38.648643 -74.648547 1
38.658067 -74.640468 1
38.579563 -74.725113 1
38.588992 -74.717052 1
38.598420 -74.708989 1
38.607848 -74.700923 1
38.617275 -74.692856 1

38.626702 -74.684786 1
38.636127 -74.676714 1
38.645553 -74.668640 1
38.654978 -74.660564 1
38.664402 -74.652486 1
38.585890 -74.737126 1
38.595319 -74.729066 1
38.604748 -74.721003 1
38.614177 -74.712939 1
38.623605 -74.704872 1
38.633032 -74.696804 1
38.642459 -74.688733 1
38.651885 -74.680660 1
38.661310 -74.672584 1
38.670735 -74.664507 1
38.592215 -74.749142 1
38.601645 -74.741082 1
38.611075 -74.733021 1
38.620504 -74.724957 1
38.629933 -74.716891 1
38.639361 -74.708823 1
38.648789 -74.700753 1
38.658216 -74.692681 1
38.667642 -74.684607 1
38.677068 -74.676530 1
38.598539 -74.761159 1
38.607970 -74.753100 1
38.617400 -74.745040 1
38.626831 -74.736977 1
38.636260 -74.728912 1
38.645689 -74.720845 1
38.655117 -74.712776 1
38.664545 -74.704704 1
38.673972 -74.696631 1
38.683399 -74.688555 1
38.604861 -74.773179 1
38.614293 -74.765121 1
38.623725 -74.757061 1
38.633156 -74.748999 1
38.642586 -74.740935 1
38.652016 -74.732869 1
38.661445 -74.724800 1
38.670873 -74.716730 1

38.680302 -74.708657 1
38.689729 -74.700583 1
38.611182 -74.785200 1
38.620615 -74.777143 1
38.630048 -74.769084 1
38.639479 -74.761023 1
38.648911 -74.752960 1
38.658341 -74.744895 1
38.667771 -74.736827 1
38.677201 -74.728758 1
38.686629 -74.720686 1
38.696058 -74.712612 1
38.617502 -74.797224 1
38.626936 -74.789168 1
38.636369 -74.781110 1
38.645802 -74.773049 1
38.655234 -74.764987 1
38.664665 -74.756923 1
38.674096 -74.748856 1
38.683526 -74.740787 1
38.692956 -74.732716 1
38.702385 -74.724643 1

A.5 Staggered - North/South Winds (STNS)

38.725620 -74.613462 1
38.725667 -74.627957 1
38.725712 -74.642452 1
38.725756 -74.656947 1
38.725797 -74.671442 1
38.725837 -74.685937 1
38.725875 -74.700432 1
38.725911 -74.714927 1
38.725946 -74.729422 1
38.725978 -74.743917 1
38.714289 -74.620769 1
38.714335 -74.635262 1
38.714379 -74.649755 1
38.714422 -74.664247 1
38.714463 -74.678740 1
38.714502 -74.693233 1
38.714539 -74.707726 1
38.714574 -74.722218 1

38.714608 -74.736711 1
38.714639 -74.751204 1
38.702911 -74.613584 1
38.702958 -74.628074 1
38.703003 -74.642565 1
38.703046 -74.657055 1
38.703088 -74.671546 1
38.703128 -74.686036 1
38.703166 -74.700527 1
38.703202 -74.715017 1
38.703236 -74.729508 1
38.703269 -74.743998 1
38.691580 -74.620889 1
38.691626 -74.635377 1
38.691670 -74.649865 1
38.691713 -74.664353 1
38.691753 -74.678842 1
38.691792 -74.693330 1
38.691829 -74.707818 1
38.691864 -74.722306 1
38.691898 -74.736794 1
38.691930 -74.751283 1
38.680201 -74.613706 1
38.680248 -74.628192 1
38.680293 -74.642678 1
38.680337 -74.657164 1
38.680378 -74.671649 1
38.680418 -74.686135 1
38.680456 -74.700621 1
38.680492 -74.715107 1
38.680527 -74.729593 1
38.680559 -74.744079 1
38.668870 -74.621009 1
38.668916 -74.635493 1
38.668961 -74.649976 1
38.669003 -74.664460 1
38.669044 -74.678943 1
38.669083 -74.693427 1
38.669120 -74.707910 1
38.669155 -74.722394 1
38.669188 -74.736878 1
38.669220 -74.751361 1
38.657492 -74.613828 1

38.657539 -74.628309 1
38.657584 -74.642791 1
38.657627 -74.657272 1
38.657669 -74.671753 1
38.657709 -74.686234 1
38.657747 -74.700716 1
38.657783 -74.715197 1
38.657817 -74.729679 1
38.657850 -74.744160 1
38.646161 -74.621129 1
38.646207 -74.635608 1
38.646251 -74.650087 1
38.646293 -74.664565 1
38.646334 -74.679044 1
38.646373 -74.693524 1
38.646410 -74.708003 1
38.646445 -74.722482 1
38.646479 -74.736961 1
38.646510 -74.751440 1
38.634782 -74.613950 1
38.634829 -74.628427 1
38.634874 -74.642903 1
38.634918 -74.657380 1
38.634959 -74.671857 1
38.634999 -74.686333 1
38.635037 -74.700810 1
38.635073 -74.715287 1
38.635107 -74.729764 1
38.635140 -74.744241 1

A.6 Staggered - West/East Winds (STWE)

38.725620 -74.613462 1
38.719990 -74.627986 1
38.725712 -74.642452 1
38.720078 -74.656974 1
38.725797 -74.671442 1
38.720160 -74.685962 1
38.725875 -74.700432 1
38.720234 -74.714949 1
38.725946 -74.729422 1
38.720301 -74.743937 1
38.714265 -74.613523 1

38.708635 -74.628045 1
38.714357 -74.642508 1
38.708724 -74.657028 1
38.714442 -74.671494 1
38.708805 -74.686011 1
38.714520 -74.700479 1
38.708879 -74.714995 1
38.714591 -74.729465 1
38.708946 -74.743978 1
38.702911 -74.613584 1
38.697280 -74.628104 1
38.703003 -74.642565 1
38.697369 -74.657082 1
38.703088 -74.671546 1
38.697450 -74.686061 1
38.703166 -74.700527 1
38.697524 -74.715040 1
38.703236 -74.729508 1
38.697591 -74.744018 1
38.691556 -74.613645 1
38.685926 -74.628163 1
38.691648 -74.642621 1
38.686014 -74.657137 1
38.691733 -74.671598 1
38.686096 -74.686111 1
38.691811 -74.700574 1
38.686170 -74.715085 1
38.691881 -74.729550 1
38.686237 -74.744059 1
38.680201 -74.613706 1
38.674571 -74.628221 1
38.680293 -74.642678 1
38.674659 -74.657191 1
38.680378 -74.671649 1
38.674741 -74.686160 1
38.680456 -74.700621 1
38.674815 -74.715130 1
38.680527 -74.729593 1
38.674882 -74.744099 1
38.668847 -74.613767 1
38.663216 -74.628280 1
38.668939 -74.642734 1
38.663305 -74.657245 1

38.669024 -74.671701 1
38.663386 -74.686210 1
38.669101 -74.700669 1
38.663460 -74.715175 1
38.669172 -74.729636 1
38.663527 -74.744140 1
38.657492 -74.613828 1
38.651861 -74.628339 1
38.657584 -74.642791 1
38.651950 -74.657299 1
38.657669 -74.671753 1
38.652031 -74.686259 1
38.657747 -74.700716 1
38.652105 -74.715220 1
38.657817 -74.729679 1
38.652172 -74.744180 1
38.646137 -74.613889 1
38.640507 -74.628397 1
38.646229 -74.642847 1
38.640595 -74.657353 1
38.646314 -74.671805 1
38.640676 -74.686309 1
38.646392 -74.700763 1
38.640750 -74.715265 1
38.646462 -74.729721 1
38.640817 -74.744220 1
38.634782 -74.613950 1
38.629152 -74.628456 1
38.634874 -74.642903 1
38.629240 -74.657407 1
38.634959 -74.671857 1
38.629321 -74.686358 1
38.635037 -74.700810 1
38.629395 -74.715309 1
38.635107 -74.729764 1
38.629462 -74.744261 1